

Nanoparticle Systems that Exploit Host Biology for Diagnosis and Treatment of Disease

by

KEVIN LIN

B.S.E. Chemical Engineering, University of Michigan, Ann Arbor (2008)

Submitted to the Department of Chemical Engineering
in partial fulfillment of the requirements for the degree of

Doctor of Philosophy in Chemical Engineering

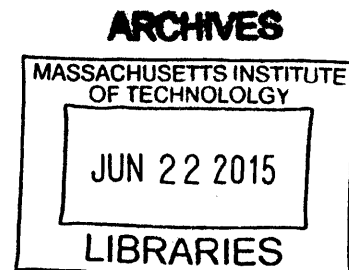
at the

MASSACHUSETTS INSTITUTE OF TECHNOLOGY

June 2014

© Massachusetts Institute of Technology 2014. All right reserved.

Signature redacted

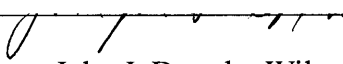


Author _____

Department of Chemical Engineering
May 5, 2014

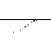
Signature redacted

Certified by _____


Sangeeta N. Bhatia
John J. Dorothy Wilson Professor of Health Sciences and Technology
& Electrical Engineering and Computer Science
Thesis Supervisor

Signature redacted

Certified by _____


Robert S. Langer
David H. Koch Institute Professor of Chemical Engineering
Thesis Supervisor

Signature redacted

Accepted by _____


Patrick S. Doyle
Chairmen, Department Committee on Graduate Students

Nanoparticle Systems that Exploit Host Biology for Diagnosis and Treatment of Disease

by Kevin Y. Lin

Submitted to the Department of Chemical Engineering on May 5, 2014 in partial fulfillment of
the requirements for the degree of Doctor of Philosophy in Chemical Engineering

Abstract

Over the past 30 years, advances in nanotechnology have generated a multitude of nanostructures exhibiting a breadth of physical, chemical, and biological properties that have tremendous potential to improve the detection and treatment of disease. Despite this progress, biomedical nanotechnologies have yet to approach the same level of complexity as biological systems, which produce higher-order functions through coordinated interactions between multiple nanoscale components. This thesis aims to explore the potential of nanoparticles to interface with the host biology to perform systems-level applications that benefit disease sensing and treatment.

First, we engineered nanoparticles to *sense* dysregulated protease activity associated with thrombosis and generate reporters that can be noninvasively quantified in the urine. These nanoparticles exploit the vascular transport of the circulatory system and the size filtration function of the renal system to emit reporters into the urine following proteolytic cleavage events. The reporter levels in the urine differentiate between healthy and thrombotic states and correlate with clot burden in a mouse model of pulmonary embolism.

Next, we developed nanoparticles that homeostatically *regulate* the biological cascade responsible for haemostasis to prevent the aberrant formation of clots. These nanoparticles form a negative feedback loop with thrombin, a key enzyme in the coagulation cascade, to regulate their release of the anticoagulant heparin. In mice, they inhibited the formation of pulmonary embolisms without an associated increase in bleeding, the primary side-effect of antithrombotic therapy in the clinic.

Finally, we investigated a two-component system whereby the first therapeutic entity induces the upregulation a molecular signal within a malignant environment to *amplify* the local recruitment of a secondary population of targeted nanoparticles. Here, the interaction between the initial therapeutic and the targeted nanoparticles occurred indirectly through a biological stress pathway. This cooperative targeting system delivered up to five-fold higher nanoparticle doses to tumors than non-cooperative controls, leading to delayed tumor growth and improved survival in mice.

Together, these systems highlight the potential for interactive nanoparticle systems to perform highly complex functions *in vivo* by leveraging and modulating the host biology. In contrast to the current strategy of injecting large populations of nanoparticles that carry out identical, pre-defined tasks with little to no feedback from the *in vivo* environment, this work supports the construction of nanoparticle systems that leverage both synthetic *and* endogenous components to produce emergent behaviors for enhancing diagnostics and therapeutics.

Thesis Supervisor: Sangeeta N. Bhatia

Title: John J. and Dorothy Wilson Professor of Health Sciences and Technology & Electrical Engineering and Computer Science

Thesis Supervisor: Robert S. Langer

Title: David H. Koch Institute Professor of Chemical Engineering

Acknowledgements

First and foremost, I would like to thank my primary adviser, Dr. Sangeeta Bhatia, for being a brilliant, inspirational mentor. Without her support through the best and worst of times, none of this work would be possible. To my co-adviser, Prof. Robert Langer, for being so generous with his time and resources and inspiring me to tackle big problems. To my committee members, Prof. Paula Hammond and Dr. Elazer Edelman, for sharing their keen insights and helping me refine my research.

To all the members of LMRT, thank you for creating such a vibrant, social, and intellectual work environment. Thank you to Geoff for brilliant research ideas; Gabe for mentorship and guidance during my formative years; Justin for being a close friend, apartment mate, artist, and collaborator; Yin for being a machine in lab and a buddy outside of lab; Ester for being funny, an awesome lab citizen, and ultra reliable collaborator; Ani for snacks and wild adventures; Nate and David for being buddies; Tal for being so smooth; Andrew for being a collaborator and research boss; Mythili for never-ending positivity and food discussions; Vyas for being the smartest person I've ever met in person to date; Alex for carrying me on the basketball court; and everyone else for being friends in and out of lab. To my UROPs, Nikita for sticking with it for three years and doing so much heavy lifting and Victoria for her kind presence and food recommendations. Special thanks to Sue, Steve, Lia, Lian'ee, and Heather for lab operations and taking care of all the 'little things' to make our research possible.

To all wonderful, talented, interesting friends I've met throughout the years. My Course X class for being the least lame class of all – Vivian, Kittipong, Rachel, Simon, Andrew H., Eric, Jen, Bonnie, Tanya, Jeremy, Andrew S., Tom, Micah, and everyone else; JM for being so good at life; Harry for having no fear; Louisa for a new experience; Raj for lots of ball; Shirley for her patience and support during the final year. Special thanks to my ninja friend Cheri Li, for being a kickass demon hunter, my Costco Chobani-run chauffeur, and so so stealthy; Armon for endless energy, peer pressure, and fun; Kartik for endless enlightening philosophies and explorations; these three have been the pillars of my support network since day one.

To MIT for being the quirky, innovative environment I always imagined it would be – thank you for all the opportunities you've given me. To the city of Boston for being so lively, strong, yet cozy. Finally, to my family – Mom, Dad, Julia – for their continued and unconditional love and support. Thank you!

Table of Contents

Abstract	1
Acknowledgements	2
Table of Contents	3
List of Figures	5
Chapter 1: Introduction	11
1.1 Nanotechnology in Medicine	11
1.2 Thrombosis.....	12
1.2.1 Diagnosis and Monitoring	16
1.2.1.1 Deep Vein Thrombosis.....	16
1.2.1.2 Pulmonary Embolism	18
1.2.2 Nanomaterials for Imaging Thrombosis.....	19
1.2.3 Synthetic Biomarkers for Urinary Monitoring of Disease	21
1.2.4 Treatment and Prevention.....	22
1.2.4.1 Anticoagulants.....	22
1.2.4.2 Antiplatelets.....	28
1.2.4.3 Thrombolytics	30
1.2.5 Nanomaterials for Treating Thrombosis	30
1.3 Cancer.....	32
1.3.1 Transport in Solid Tumors.....	34
1.3.2 Nanoparticles for Cancer Therapy.....	37
1.3.3 Systems of Nanoparticles for Amplified Delivery	40
1.3.4 Vascular Disrupting Agents	42
1.4 Scope of the Dissertation.....	45
Chapter 2: Nanoparticles that Sense Thrombin Activity as Urinary Biomarkers of Thrombosis	46
2.1 Abstract	46
2.2 Introduction	46
2.3 Results and Discussion.....	49
2.4 Conclusion.....	64

2.5 Materials and Methods	67
2.6 Acknowledgements	70
Chapter 3: Self-Titrating Anticoagulant Nanocomplexes that Restore Homeostatic Regulation of the Coagulation Cascade	72
3.1 Abstract	72
3.2 Introduction	72
3.3 Results	74
3.4 Discussion	89
3.5 Conclusion.....	91
3.6 Materials and Methods	92
3.7 Acknowledgements	95
Chapter 4: Drug Induced Amplification of Nanoparticle Targeting to Tumors	97
4.1 Abstract	97
4.2 Introduction	97
4.3 Results	100
4.4 Discussion	115
4.5 Conclusion.....	117
4.6 Materials and Methods	118
4.7 Acknowledgements	123
Chapter 5: Perspectives and Future Directions	125
5.1 Nanoparticles that Sense Coagulation Activity <i>In Vivo</i>	125
5.2 Nanoparticles that Regulate Biological Processes <i>In Vivo</i>	126
5.3 Drug-Induced Amplification of Nanoparticle Targeting <i>In Vivo</i>	128
References.....	131

List of Figures

Figure 1.1. Molecular pathways of the coagulation cascade divided into (A) the initiation phase and (B) the amplification phase.	14
Table 1.1 Bleeding Rates for Selected Anticoagulants.	23
Figure 1.2. Nanoparticle communication for amplified tumor targeting.	41
Figure 2.1. (A) Schematic of approach. Synthetic biomarkers composed of NWs conjugated with a thrombin-sensitive substrate in tandem with a ligand-encoded reporter. These agents survey the vasculature for the sites of clot formation where thrombin activity cleaves and releases the reporters into urine for analysis by ELISA. (B) Schematic of fluorogenic NW assay for detecting protease activity. (C) Kinetics of fluorogenesis produced by the activity of thrombin (red) and other coagulation proteases (n = 3 per condition). Thr, thrombin; Bival, bivalirudin. (D) Kinetics of fluorogenesis in plasma after the addition of CaCl ₂ to activate coagulation (n = 3 per condition).	48
Figure 2.2. <i>In vitro</i> characterization of NWs. (A) Size distribution of iron oxide NWs as determined by dynamic light scattering. (B) Absorbance spectra of NWs conjugated with fluorescein-labeled peptides (~500 nm) and free NWs (white). (C) Fluorescence spectra of NWs conjugated with fluorescein-labeled peptides and NWs incubated with equivalent amount of free fluorescein-labeled peptides (Excitation: 470 nm; emission: 500-700 nm; cutoff: 495 nm; quenching efficiency = 92.4%). (D) Average size of NWs incubated in 10% serum at 37°C over time as determined by dynamic light scattering (n = 3 per condition, s.d.). (E) Average fluorescence of NWs incubated in 10% serum at 37°C over time (Excitation: 485 nm; emission 538 nm; cutoff: 530 nm). NWs do not appear to dequench under these conditions (n = 3 per condition, s.d.).	50
Figure 2.3. Structures of peptide-conjugated NWs. (A) (K-Flsc)GGfPRSGGGC conjugated to NWs for <i>in vitro</i> protease assays. (B) Biotin-eGvndneeGffsar(K-Flsc)GGfPRSGGGC conjugated to NWs for urinary monitoring of thrombosis (Biotin = red, Glu-Fib = black, Flsc = purple, thrombin substrate = blue, NW = brown).	51
Figure 2.4. Designing ligand-encoded reporters for detection by ELISA. (A) Schematic of ligand-encoded reporters R ₁ and R ₂ along with chemical structures of associated ligands. (B) Schematic of ELISA sandwich complex and photograph of developed 96-well plates showing specific detection of R ₁ and R ₂ spiked into control urine samples. (C) Absorbance values (λ = 450 nm) of wells coated with anti-Flsc antibodies used to detect serial dilutions of R ₁ , R ₁ + R ₂ , and R ₂ in urine (n = 3 per condition, s.d.). (D) Quantification of the level of cleaved reporters (R ₁) released from NWs after incubation with increasing concentrations of thrombin (n = 3 per dose, s.d.).	54

- Figure 2.5.** Photograph of developed 96-well plates showing serial dilutions of R₁, R₁ + R₂, and R₂ in urine detected using an (A) anti-Flsc or (B) anti-AF488 capture antibody. (C) Absorbance values ($\lambda = 450$ nm) of wells coated with anti-AF488 antibodies used to detect serial dilutions of R₁, R₁ + R₂, and R₂ in urine (n = 3 per condition, s.d.).54
- Figure 2.6.** Induction of thrombosis by thromboplastin. (A) Near-infrared fluorescent scans of excised organs to monitor the deposition of VT750-labeled fibrinogen following intravenous administration of thromboplastin (2 μ L/g body weight) or PBS. (B) Quantification of the level of VT750-fibrin(ogen) deposited in organs harvested from thrombosis and control mice (* $P < 0.05$, ** $P < 0.01$, *** $P < 0.005$, Student's t -test; n = 3 per group, s.d.). (C) Hematoxylin and eosin staining of lungs harvested from thrombosis and healthy mice (scale bar = 100 μ m). Blue arrow denotes fibrin clot. (D) Quantification of fibrin deposited in the lungs in response to escalating doses of thromboplastin. Bival, bivalirudin (* $P < 0.05$, ** $P < 0.01$, *** $P < 0.005$, one-way ANOVA with Tukey post test; n = 3–5 mice, s.e.).56
- Figure 2.7.** Hematoxylin and eosin staining of organ sections excised from mice following intravenous injection of thromboplastin (2 μ L/g b.w.) or PBS (scale bar = 100 μ m). No fibrin clots were observed in any of the organ sections.....57
- Figure 2.8.** Near-infrared fluorescent scans of the level of VT750-fibrin(ogen) deposited in the lungs in response to increasing doses of thromboplastin and its inhibition by bivalirudin (Bival).58
- Figure 2.9.** Noninvasive urinary detection of pulmonary embolism. (A) Quantification of the distribution of VT750-labeled NWs in organs excised from mice treated with thromboplastin or PBS (n = 3 mice, s.d.). (B) Quantification of the fluorescent signal of organs after mice were infused mixtures of NWs conjugated with quenched substrates (labeled with VT750) and thromboplastin or PBS (** $P < 0.01$, Student's t -test; n = 3 mice, s.d.). Inset shows representative fluorescent scans of the kidneys and the lungs. (C) *In vivo* fluorescent image after administration of NWs showing increased fluorescent signal localized to the bladders of mice challenged with thromboplastin. (D) Normalized urinary reporter levels (R₁/R₂) from healthy mice (Day 0) and in response to thromboplastin and bivalirudin (Day 5). Bival, bivalirudin (*** $P < 0.005$, two-way ANOVA with Bonferroni post test; n = 5 mice, s.e.). (E) Correlation plot of the clot burden in the lungs versus urinary biomarker levels (Pearson's $r = 0.999$; n = 5–10 mice, s.e.).....60
- Figure 2.10.** Near-infrared fluorescent scans of excised organs to assess VT750-NW distribution following intravenous injection of thromboplastin (2 μ L/g b.w.) or PBS.61
- Figure 2.11.** Near-infrared fluorescent scans of excised organs to monitor substrate-NW cleavage in response to thromboplastin (2 μ L/g b.w.) or PBS.61
- Figure 2.12.** Immunofluorescent staining of lung sections following intravenous injection of thromboplastin or PBS. Staining of fibrin clots (red), NWs (green), and nuclei (blue) in the lung (scale bar = 100 μ m).62

Figure 2.13. Monitoring urine concentration by administering R₂ intravenously in mice. (A) Urine volume collected from control mice *versus* mice hydrated with 10% body weight equivalent of PBS injected subcutaneously, two hours after administration (*****P** < 0.005, Student's *t*-test; n = 5 mice.). (B) Quantification of R₂ in urine collected from control *versus* hydrated mice *via* ELISA (*****P** < 0.005, Student's *t*-test; n = 5 mice.).....62

Figure 3.1. Schematic of self-titrating activatable therapeutic. (A) Self-assembly of cationic PEG-Peptide and anionic heparin to form nanoSTATs. (B) Negative feedback system for self-titrating release of heparin in response to thrombin activity.75

Figure 3.2. *In vitro* characterization of nanoSTATs. (A) Transmission electron microscopy image of nanoSTATs (scale bar = 100 nm). (B) Mean hydrodynamic diameter of nanoSTATs at varying PEG:LVPR.RK4:Heparin ratios in PBS and 10% serum (n = 3 per condition, s.d.). (C) Zeta potential of nanoSTATs at varying PEG:LVPR.RK4:Heparin ratios in PBS and 10% serum (n = 3 per condition, s.d.).....77

Figure 3.3. Cell viability assay. Percent viability of HUVECs incubated with varying concentrations of nanoSTATs (nS), PEG-LVPR.RK4, LVPR.RK4, and free heparin as determined by a MTS assay (n = 3 per condition).....79

Figure 3.4. FPLC analysis of nanoSTATs. FPLC chromatograms of intact nanoSTATs (nS), nanoSTATs incubated with thrombin, and free heparin as monitored by absorbance at 488 nm.79

Figure 3.5. Azure II assay for heparin quantification. (A) Standard curve of free heparin mixed with Azure II (slope = 0.037, y-intercept = 0.097, $r^2 = 0.98$; n = 3 per condition, s.d.). (B) Free heparin from nanoSTATs quantified before and after incubation with thrombin by Azure II assay. Absorbance was compared to the standard curve of free heparin from (A) to determine the amount of free heparin (n = 3 per condition, s.d.).....80

Figure 3.6. *In vitro* nanoSTAT drug release and function. (A) Heparin activity when complexed with peptides and incubated with thrombin, as determined by anti-FXa assay (n = 3 per condition, s.d.). Pep, peptide; D, D-isomer; Thr, thrombin. (B) Release profile of heparin from nanoSTATs as a function of thrombin concentration and incubation time. Amount of heparin released was determined by anti-FXa assay (n = 3 per condition, s.d.). (C) Activated partial thromboplastin time of normal human control plasma spiked with free heparin or nanoSTATs (nS) (**P** < 0.001 by Student's *t*-test; n = 3 per condition, s.d.).....82

Figure 3.7. *In vivo* bleeding time of nanoSTATs. (A) Circulation time of nanoSTATs (nS) and free heparin as determined by fluorescence using FITC-heparin (n = 3 mice, s.e.). (B) Circulation time of nanoSTATs (nS) and free heparin (Hep) as determined by anti-FXa assay on mouse plasma samples withdrawn over time (n = 3 mice, s.e.). (C) Tail bleeding time of mice administered 200 U/kg of free heparin or nanoSTATs (****P** < 0.01 by one-way ANOVA with Tukey post test; n = 5–7 mice, s.e.).....85

- Figure 3.8.** Deposition of VT750-fibrin in thromboplastin-induced model of thrombosis. Near-infrared fluorescent scans of excised organs to assess VT750-NW distribution following intravenous injection of thromboplastin (2 $\mu\text{L/g}$ b.w.) or PBS.87
- Figure 3.9.** *In vivo* therapeutic efficacy of nanoSTATs. (A) Quantification of fibrin deposited in the lungs of mice dosed with thromboplastin (T, 2 $\mu\text{L/g}$ body weight) and nanoSTATs (nS, 200 U/kg) or free heparin (Hep, 200 U/kg) (** $P < 0.01$ by one-way ANOVA with Tukey post test; $n = 5$ mice, s.e.). (B) Near-infrared fluorescent scans of excised lungs to assess VT750-labeled fibrinogen following intravenous injection of PBS, T only, T + nS, and T + Hep. (C) H&E staining of lungs in mice under the same conditions as in (B). Arrow denotes fibrin clots; arrowheads denote patent vessels (scale bar = 100 μm).87
- Figure 3.10.** Heparin dose response in thromboplastin-induced thrombosis model. Quantification of fibrin deposited in the lungs in response to escalating doses of heparin (Hep) ($n = 3-5$ mice, s.e.).88
- Figure 4.1.** Schematic of cooperative targeting approach. Inducing agent, ombrabulin, disrupts the tumor vasculature, which initiates a cascade of intratumoral effects that leads to upregulated presentation of the p32 protein. LyP-1 coated nanoparticles that target the p32 protein then home to the tumor.99
- Figure 4.2.** Characterization of ombrabulin effect on tumor microenvironment. (A) Schematic of ombrabulin-induced enhancement in p32 presentation. (B) Intraoperative images at 24 hr post injection (p.i.) revealing ombrabulin mediated hemorrhaging. (C) Hematoxylin and eosin staining of tumors harvested from mice injected with ombrabulin at different timepoints p.i. (Con., control (0 mg/kg); scale bar = 100 μm). (D) Immunofluorescent staining of tumors without (0 mg/kg) and with (60 mg/kg) ombrabulin (red = p32 staining, blue = nuclear stain; scale bar = 1 mm). (E) Quantification of percentage p32 positive area of immunofluorescent staining of tumors receiving different dosages of ombrabulin at different timepoints p.i. ($n = 3$ mice, s.e.). (F) Quantification of percentage p32 positive human cells from tumors receiving different dosages of ombrabulin at different timepoints as determined by flow cytometry (** $P < 0.005$, one-way ANOVA with Tukey post test; $n = 3$ mice, s.e.).101
- Figure 4.3.** Flow cytometry analysis of p32 expression on cells *ex vivo*. (A) Representative histograms of untreated MDA-MB-435 xenograft cells stained with AF488-conjugated mouse IgG control or AF488-conjugated mouse anti-HLA A/B/C, used to exclude non-xenograft cells from final analysis. (B) Representative histograms of *ex vivo* MDA-MB-435 cells 24-hours post treatment with ombrabulin (60 mg/kg), stained with either rabbit IgG control or rabbit anti-p32 antibody to establish the threshold for positive p32 staining. (C) Flow cytometry histogram of *ex vivo* MDA-MB-435 cells stained for p32 following treatment without (0 mg/kg) or with ombrabulin (60 mg/kg).....103
- Figure 4.4.** Ombrabulin mediated amplification of NW delivery. (A) Schematic of ombrabulin signaling to NWs. (B) Experimental timeline for testing the signaling system. (C) Quantification of NW homing to tumors as a function of ombrabulin dosage (** $P < 0.01$,

Student's *t*-test; *n* = 3–4 mice, s.e.). (D) Representative near-infrared fluorescent scans of NW homing to tumors in response to increasing doses of ombrabulin. Tumors were excised and imaged at 24 hrs post-NW injection. (E) Immunofluorescent staining of NWs in tumors without (0 mg/kg) and with (60 mg/kg) ombrabulin (green = NW, red = p32 staining, blue = nuclear stain; scale bar = 100 μm). 104

Figure 4.5. *In vitro* characterization of NWs. (A) Size distribution of iron oxide NWs as determined by dynamic light scattering. (B) Absorbance spectra of NWs conjugated with fluorescein-labeled peptides (~500 nm) and VT750 (~750 nm) and free NWs (grey). (C) Circulation time of NWs as determined by near-infrared fluorescence in the blood (*n* = 3 mice, s.d.). 105

Figure 4.6. *In vitro* binding of NWs and LPs to recombinant p32. (A) Quantification of NW binding to p32 (***P* < 0.005, Student's *t*-test; *n* = 3, s.d.). (B) Quantification of LP binding to p32 (***P* < 0.005, Student's *t*-test; *n* = 3, s.d.). 107

Figure 4.7. *In vivo* biodistribution of NWs. Near-infrared fluorescent scans of NW distribution in organs without (0 mg/kg) or with (60 mg/kg) ombrabulin (Omb.). Organs were excised and imaged at 24 hrs post-NW injection. 108

Figure 4.8. Effect of administration schedule on NW homing. Quantification of NW homing to tumors as a function of different times between ombrabulin (60 mg/kg) and NW administration (** *P* < 0.01, Student's *t*-test; *n* = 3–4 mice, s.e.). 108

Figure 4.9. Ombrabulin mediated amplification of LP delivery. (A) Schematic of ombrabulin signaling to LPs. (B) Quantification of doxorubicin-loaded LP homing to tumors as a function of ombrabulin dosage (***P* < 0.005, Student's *t*-test; *n* = 3 mice, s.e.). (C) Immunofluorescent staining of LPs in tumors without (0 mg/kg) and with (60 mg/kg) ombrabulin (green = LP, red = p32 staining, blue = nuclear stain; scale bar = 100 μm). (D) Quantification of doxorubicin-loaded LP biodistribution in organs without (0 mg/kg) and with (60 mg/kg) ombrabulin (No significance, one-way ANOVA with Tukey post test; *n* = 3–6 mice, s.d.). 110

Figure 4.10. *In vitro* characterization of LPs. (A) Size distribution of doxorubicin-loaded LPs as determined by dynamic light scattering. (B) Fluorescence spectra of LPs conjugated with fluorescein-labeled peptides (excitation: 444 nm, emission: 480–700 nm, cutoff: 475 nm) and untargeted LPs (grey). (C) Circulation time of LPs as determined by doxorubicin fluorescence in the blood (*n* = 3 mice, s.d.). 111

Figure 4.11. Therapeutic efficacy of cooperative targeting system. (A) Tumor volumes of different groups following three weeks of treatment. Black arrow head denotes time of ombrabulin (60 mg/kg) administration; orange arrow head denotes time of LP (1 mg/kg by dox) administration (* *P* < 0.05, ** *P* < 0.01, *** *P* < 0.005, two-way ANOVA with Bonferroni post test, *n* = 7 mice, s.e.). (B) Change in body weight of different groups

following three weeks of treatment (n = 7 mice, s.e.). (C) Survival rate of different groups in the therapeutic efficacy study (** $P < 0.01$, log rank test; n = 7 mice).113

Figure 4.12. Tumor doubling time during therapeutic efficacy study. Calculated time to the doubling of tumor volume during the course of the therapeutic study (* $P < 0.05$, ** $P < 0.01$, *** $P < 0.005$, one-way ANOVA with Tukey post test; n = 7 mice, s.e.). Doubling time calculated by fitting tumor volumes to exponential growth curves. Table 1 shows the average coefficient of determination (R^2) of the curve fittings for each treatment group.....114

Figure 5.1. Schematic of a screening approach for identifying drug-induced antigens and matching targeting ligands.....130

Chapter 1: Introduction

1.1 Nanotechnology in Medicine

Our bodies are driven by biological processes, including events that are essential for life and those that lead to disease, which occur at the nanoscale. We are composed of biological nanoscale components, and the ability to manipulate materials at this scale opens tremendous opportunities to impact biological discovery and medicine. In particular, nanoparticles possess unique combinations of physical, chemical, and biological properties that are highly tunable compared to their synthetic or natural protein and small molecule complements. These properties include superparamagnetism, surface plasmon resonance, quantum confinement, self-assembly, high surface areas for drug loading, catalytic activity, multivalent presentation of ligands, tunable surface chemistries, extended pharmacokinetic profiles, and many others.¹⁻⁵ The most advanced systems to date can even respond to external stimuli such as ultrasound, light, magnetism, electricity, and heat, or endogenous stimuli such as pH, chemical reduction, and enzymes.⁶⁻⁸

Indeed, engineering of these properties has already yielded a spectrum of applications for improving the diagnosis and treatment of diseases. Nevertheless, despite operating on the same length scales as biological components, these nanoparticle approaches still lack the system-scale complexity of biological systems. As our understanding of nanoengineering and biology continue to grow in parallel, new biomedical nanosystems will emerge that are capable of interacting and even integrating with the endogenous biological nanomachinery to perform highly complex tasks *in vivo*. The overall goal of this thesis is to engineer nanoparticle systems that interact with and exploit the host biology to produce higher-order emergent functions that enhance the diagnosis and treatment of thrombosis and cancer.

1.2 Thrombosis

Thrombosis, the formation of a blood clot within a vessel, is associated with numerous life threatening conditions, including myocardial infarction (heart attack) and strokes, which are collectively the most common cause of death not only in the developed world, but globally.⁹⁻¹¹ Furthermore, thrombosis is also the second leading cause of death in patients with cancer.¹⁰ Our growing understanding of the underlying mechanisms of thrombus formation has enabled novel technologies to impact the development of more effective methods to diagnose, prevent, and treat thrombosis.

Thrombosis is closely linked to haemostasis, the biological process that maintains the integrity of blood vessels after vascular damage, sharing the principal pathways of platelet activation and blood coagulation. Platelets are small ($\sim 1 \mu\text{m}$) anucleate cells produced by megakaryocytes in the bone marrow that circulate in the blood and serve as sentries of vascular integrity. When vascular damage occurs, platelets are rapidly recruited to the site of injury through the interaction of specific platelet cell-surface receptors with the exposed subendothelial matrix proteins, collagen and von Willebrand factor to provide provisional wound closure. The platelets adhere to the vessel wall and become activated, releasing the contents of their granules to promote further platelet activation and receptor-mediated binding of additional platelets (termed platelet aggregation). This continual process of platelet adhesion, activation, and aggregation promotes the rapid growth of the thrombus.^{9, 11}

In parallel with platelet recruitment, the coagulation cascade, which consists of a group of zymogens that latently circulates through the bloodstream, is triggered at the site of injury as well. Briefly, vascular damage exposes the protein tissue factor (TF) that is expressed on extravascular cells, which initiates the activation of Factor X in conjunction with Factor VIIa and

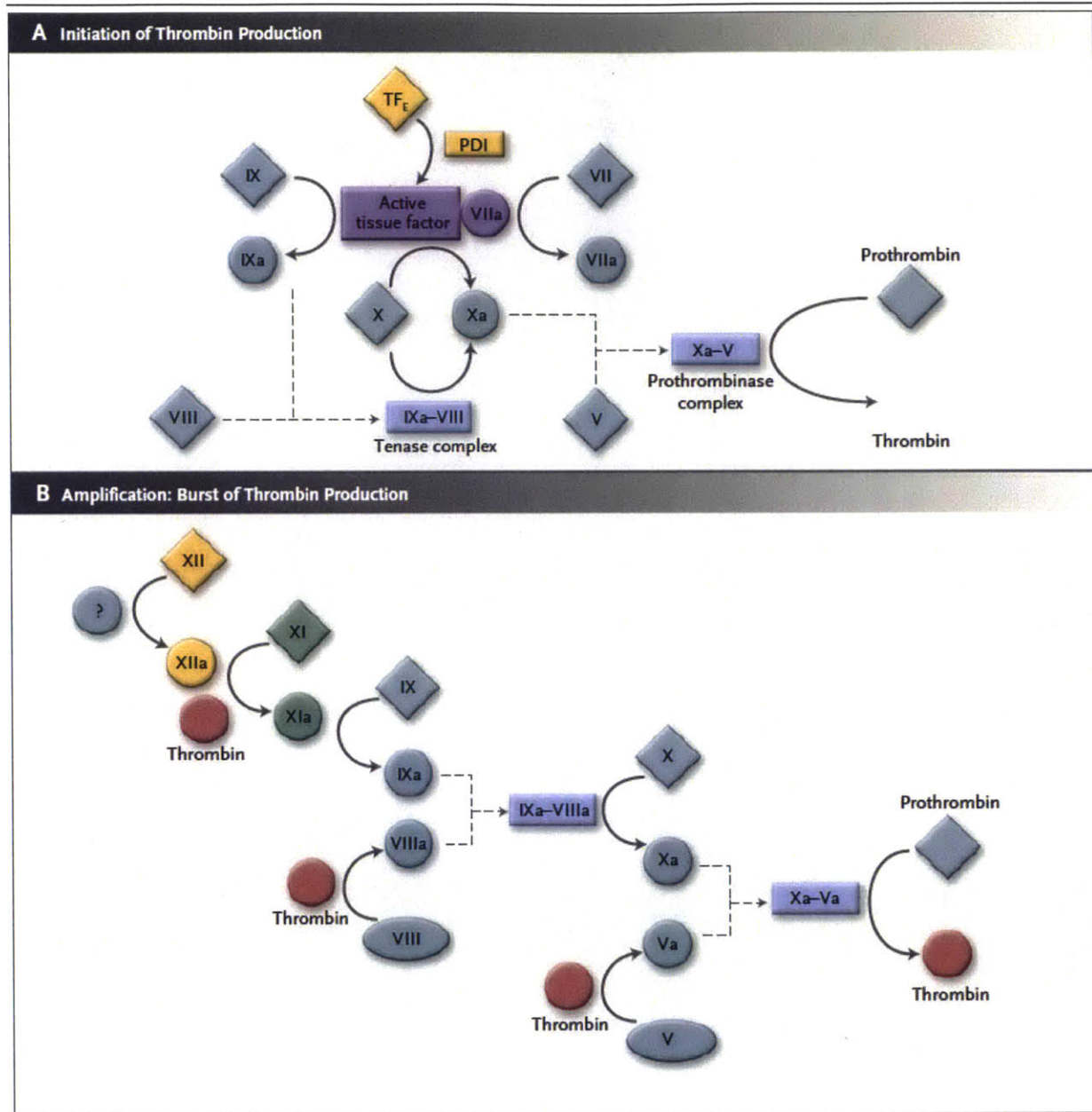


Figure 1.1. Molecular pathways of the coagulation cascade divided into (A) the initiation phase and (B) the amplification phase.¹⁰

features. Arterial thrombosis is triggered by the rupture of atherosclerotic plaque that develops through the deposition of lipid and foam cells in the artery wall over time. This event exposes the blood to collagen in the extracellular matrix and previously sequestered TF in the plaque, initiating the thrombotic event that is the major pathogenic process underlying myocardial infarction, stroke, and other conditions. Platelet recruitment preferentially occurs in regions of high shear and disturbed flow, such as at the site of plaque rupture in the artery, which leads to the formation of platelet-rich thrombi referred to as 'white clots'.^{9, 10, 14}

During the 19th century, the physician Virchow elucidated a triad of physiological alterations that contribute to venous thrombosis: circulatory stasis, hypercoagulable state, and activation of the endothelium. Reduced blood flow and stasis may explain the increased rate of venous thrombosis associated with surgery, hospitalization, paralysis, travel, obesity, age, and pregnancy. A hypercoagulable state refers to procoagulant changes in the blood constitution that may be associated with genetic disorder, age, major surgery, cancer, pregnancy, hormone contraceptives, and obesity. Finally, vessel wall injury caused by numerous potential sources, including trauma, surgery, venepuncture, or indwelling catheters, downregulates endogenous endothelial-associated anticoagulants and activates TF and various adhesion molecules that promote coagulation. In contrast to arterial thrombosis, venous thrombosis occurs under lower shear stress on the largely intact endothelium and is characterized by thrombi that are rich in fibrin and trapped red blood cells, typically referred to as 'red clots'. The most common clinical manifestations are deep vein thrombosis (DVT), which mostly occurs in the legs, and potentially fatal pulmonary embolism (PE), the migration of a dislodged blood clot to the lung.^{9, 15}

1.2.1 Diagnosis and Monitoring

While much progress has been made towards quickly and accurately diagnosing conditions associated with arterial thrombosis, such as myocardial infarction (e.g. electrocardiogram, cardiac biomarkers in blood) and stroke (e.g. computed tomography, magnetic resonance imaging), diagnosis of venous thrombosis remains a medical challenge because symptoms and signs of the condition are highly nonspecific and tools capable of differential diagnosis are not yet available. The specific steps to identifying the presence of venous thrombosis vary by subtype of disease, however the general approach is as follows: initial evaluation with a clinical prediction test in conjunction with laboratory assays, noninvasive imaging of suspected thrombus, and venography if imaging is equivocal. Unfortunately, the available laboratory assays suffer from low specificity for diagnosing thrombosis. Imaging techniques are more expensive, require established hardware infrastructure, and rely on substantial technical expertise to accurately acquire and interpret results, and may still deliver varying degrees of accuracy for diagnosis. Thus, there remains a strong need to develop rapid, definitive, and cost-effective methods for diagnosing venous thrombosis.

1.2.1.1 Deep Vein Thrombosis

Diagnosis of DVT begins with a physical exam of the involved extremity for associated symptoms – a palpable cord (reflecting a thrombosed vein), edema, warmth, and vein dilation – and an assessment of clinical risk factors that comprise the pretest probability of thrombosis known as the Wells score. The Wells score is most typically used in conjunction with a laboratory measurement of D-dimer, which is a degradation product of cross-linked fibrin in the blood. Analysis of D-dimer is most commonly carried out using enzyme-linked immunosorbent assays (ELISA), however rapid whole blood agglutination assays are also available. A major

limitation of the measurement is that the presence of elevated D-dimer concentrations is insufficient to diagnose venous thrombosis because elevated levels are non-specific and commonly present in hospitalized patients (particularly the elderly), cancer patients, recent surgery patients, and numerous other conditions including the second and third trimester of pregnancy. However, the negative predictive value of the D-dimer assay is high (94%), and a combination of a negative D-dimer assay and Wells score is used to rule out DVT in many patient populations.^{16, 17}

Noninvasive imaging of the lower extremity is recommended for patients with intermediate to high Wells score and/or positive D-dimer. The two most common methods for diagnosing DVT are compression ultrasonography and impedance plethysmography. While ultrasound is considered superior (positive predictive value of 94% versus 83%) and more widely available, it is unable to resolve thrombi in certain anatomical locations (e.g. iliac vein) and less useful for monitoring recurrent DVTs. Impedance plethysmography is less expensive and preferred for evaluation of suspected recurrent DVT, but is limited by its requirement that patients lie still for several minutes in correct positioning to avoid data artifacts and its susceptibility to false positives in patients with prior venous diseases. Magnetic resonance venography (MRI) and computed tomography (CT) are also emerging modalities for diagnosing DVT, however their higher costs may preclude them from becoming the noninvasive tests of choice. If noninvasive testing is clinically infeasible, or results are equivocal or in disagreement with strong clinical suspicion of DVT, contrast venography may be required. However, while contrast venography has long been considered the reference test for diagnosis of DVT, it is an invasive technique associated with higher costs, morbidity, patient discomfort, as well as other technical limitations.^{16, 17}

1.2.1.2 Pulmonary Embolism

Over 90% of cases of acute PE are due to emboli emanating from a DVT. Since the symptoms of PE are also highly variable and non-specific, the diagnostic approach is similar to that of DVTs is used to confirm or exclude the condition. Although the tests employed depend on availability at a particular medical institution, evaluation usually begins with a clinical pretest probability, called the modified Wells criteria for PE, in conjunction with the D-dimer assay; this combination has negative predictive value when used appropriately. For patients with moderate to high probability, imaging is performed to support the diagnosis of PE. While pulmonary angiography is considered the ‘gold standard’ for the diagnosis of PE, this technique has fallen out of favor because its increased risk of morbidity and mortality – usually related to catheter insertion, contrast reactions, cardiac arrhythmia, or respiratory insufficiency – as well as increased radiation exposure relative to noninvasive imaging techniques.^{18, 19}

CT pulmonary angiography (CT-PA) has emerged as the preferred noninvasive modality because of its ability to detect alternative pulmonary abnormalities that may explain a patient’s symptoms. The PIOPED II study, the largest of its kind to date, demonstrated that CT-PA has a sensitivity and specificity of 83% and 96% in diagnosing PE, though other studies have reported sensitivities ranging from 53 to 87%.²⁰ At institutions without CT-PA or for patients who cannot undergo the procedure (e.g. renal insufficiency or morbid obesity), the ventilation/perfusion (V/Q) scan, an imaging technique used to evaluate the circulation of air and blood in the lungs, can be used instead. Unfortunately, the lung scan result most commonly observed in patients has a diagnostic accuracy of only 15-86%, which is insufficient to confirm or exclude PE.^{18, 19}

1.2.2 Nanomaterials for Imaging Thrombosis

The use of nanomaterials to improve the diagnosis of thrombosis is a growing field of research. Studies to date have primarily leveraged two properties through which nanoparticles can improve the detection and diagnosis of thrombosis, particularly for imaging applications. First, nanomaterials can incorporate various novel materials, signaling modalities, and/or amplification strategies to improve signal-to-noise ratio. Second, these nanomaterials can be decorated with affinity ligands (e.g. antibodies, antibody fragments, peptides, small molecules) that recognize specific molecular or cellular targets associated with the condition of interest. A number of studies have developed nano-based imaging agents targeting thrombin, which has the potential to facilitate signal amplification through its proteolytic activity.²¹ Weissleder *et al* have developed a series of thrombin-activated, dequenching near-infrared probes that can differentiate between acute and subacute thrombi *in vivo*,^{22, 23} a characteristic that is important for fibrinolytic therapy because efficacy decreases with thrombus age.²⁴ Tsien *et al* have developed similar thrombin-sensitive cell-penetrating probes for detecting thrombin activity in atherosclerotic plaques. While optical imaging is an established research tool for preclinical small animal models, it is still an emerging modality for clinical practice and questions remain about whether the signal penetration depth is sufficient for imaging applications deeper than surface vessels.²⁵

Fibrin is a promising imaging target because it forms the structural basis of clots and is present in both venous and arterial thrombosis.²¹ The most clinically advanced probe to date is a fibrin-targeted peptide MRI agent, called EP-2104R, coupled with four gadolinium molecules to increase thrombus-to-background ratio through multivalency. Extensive preclinical work with this agent has demonstrated MRI enhancement of PE, atrial thrombi, and coronary stent thrombosis.²⁶⁻³⁰ The use of EP-2104R in humans has been investigated in several Phase I/II

trials. A nanoparticle consisting of a lipid shell encapsulating perfluorocarbon and gadolinium-diethylenetriaminepentaacetic acid (Gd-DTPA) complexes embedded in the shell was targeted to clots using anti-fibrin antibodies. These particles demonstrated strong binding to the thrombus surface and enhanced signal contrast, although *in vivo* usage has yet to be tested.^{31, 32} Other groups have also synthesized fibrin-targeted nanoparticles for CT and ultrasound imaging of thrombi.^{33, 34} Rather than target fibrin directly, other nanoagents are decorated with substrates for Factor XIII, the transglutaminase that cross-links fibrin *in vivo*. These multimodal agents are incorporated into acute thrombi and detected by near-infrared fluorescence imaging or MRI.^{35, 36} In addition to more accurate diagnosis, these fibrin-targeted agents may also improve management of fibrinolytic therapy by providing information about the age, amount, and activity of clots.

In addition to diagnosis and management of therapy, another emerging application of diagnostic nanomaterials is stratification of risk. This application relies on the identification of molecular entities that reveal biological and clinical insights with regard to disease state in order to leverage our ability to target and image them with probes. For example, current imaging modalities used to image plaque anatomy in atherosclerosis do not identify high-risk lesions for rupture and subsequent arterial thrombosis in the form of myocardial infarction or stroke. Identification of these lesions in important vascular beds could be used to manage systemic therapy regimens and even guide local therapy in high-risk patients.²¹ Potential markers are cells or proteins that play a role in plaque destabilization, such as inflammatory cells (e.g. macrophages), apoptotic cells (e.g. annexin V), and proteases (e.g. MMP2, MMP9, cathepsins).³⁷ While all the aforementioned strategies have exclusively leveraged imaging modalities as the

readout, little effort has been focused on developing non-imaging-based diagnostics that retain the ability to reveal important biological and clinical information about the *in vivo* environment.

1.2.3 Synthetic Biomarkers for Urinary Monitoring of Disease

Our lab has recently pioneered the concept of ‘synthetic biomarkers,’ which are exogenously administered nano-based probes that leverage features of human disease and physiology to enable noninvasive urinary monitoring. This technology has emerged to address the challenge of identifying new clinical biomarkers, a process which is limited by our dependence on endogenous molecules. These protease-sensitive agents perform three primary functions *in vivo*: targets sites of disease, sample dysregulated protease activities, and release encoded reporters into hose urine for detection by various methods including mass spectrometry and antibody-based assays. In mouse models of liver fibrosis and cancer, these agents can noninvasively monitor fibrosis and resolution without the need for biopsies and substantially improve early detection of cancer relative to clinical blood biomarkers.³⁸

In this Chapter 1 of this thesis, the synthetic biomarker technology is applied to the detection of thrombosis, a protease-driven disease that is readily accessible to the nanoprobe that circulate throughout the vasculature. The approach of synthetic biomarkers has the potential to enable point-of-care testing, which could benefit patients at risk for recurrent thrombosis who require frequent monitoring, patients who need to monitor anticoagulant levels long-term, and developing nations where thrombosis-associated conditions such as cardiovascular disease and cancer are on the rise, but medical infrastructure (e.g. imaging hardware) for inexpensive and rapid diagnosis is still unavailable.

1.2.4 Treatment and Prevention

Since a previous episode is one of the biggest risk factors of thrombosis, prevention of future events is a critical part of treatment. The primary pharmacological classes used to treat thrombosis are anticoagulants, antiplatelets, and thrombolytics.

1.2.4.1 Anticoagulants

Anticoagulants, drugs that block the coagulation cascade, are a critical component of treatment and prevention for both arterial and venous thrombosis. The primary side effect and fundamental challenge of anticoagulant therapy is bleeding (**Table 1.1**). The ideal anticoagulant is an agent that inhibits thrombosis but not haemostasis, however this ‘holy grail’ of antithrombotic therapy has yet to be found. Substantial progress has been made in understanding the biology and pathophysiology of thrombosis, and translation of this knowledge to pharmaceutical development may lead to safer, more effective drugs in the future. Currently, the types of anticoagulants available can broadly be divided into two main segments: parenteral and oral drugs.

Parenteral anticoagulants

Parenteral anticoagulants are administered intravenously (IV) or subcutaneously (SC), and are thus better suited for short-term use in the hospital setting, particularly for acute care when immediate onset of action is crucial. Unfractionated heparin (UFH), a heterogeneous mixture of branched glycoaminoglycans ranging from 3000-30000 kDa, was discovered to have potent antithrombotic properties in 1916 and is the oldest anticoagulant used in the clinic.³⁹ UFH forms a complex with endogenous antithrombin-III, which then inactivates thrombin, and Factors Xa, IXa, XIa, and XIIa. Thrombin and Factor Xa are most sensitive to inhibition by the

Table 1.1 Bleeding Rates for Selected Anticoagulants.⁴⁰

Agent	Indication	Incidence of major bleeding, %	Reference
UFH	VTE prophylaxis	3.5 (69/1992)	Freedman et al (2000) ¹⁹
	VTE treatment	2.0 (17/748)	Mismetti et al (2005) ²⁰
	ACS	4.5 (386/8606)	Petersen et al (2004) ²¹
LMWH Enoxaparin	VTE prophylaxis	1.7 (63/3621)	Turpie et al (2002) ¹⁴
	VTE treatment	2.1 (16/754)	Mismetti et al (2005) ²⁰
	ACS	4.7 (381/8044)	Petersen et al (2004) ²¹
Dalteparin	VTE prophylaxis	1.5 (15/983)	Hull et al (2000) ²²
	ACS	3.3 (34/1049)	FRIISC II Investigators (1999) ²³
Tinzaparin	VTE treatment	2.0 (6/304)	Simonneau et al (1997) ²⁴
Factor Xa inhibitor Fondaparinux	VTE prophylaxis	2.7 (96/3616)	Turpie et al (2002) ¹⁴
	VTE treatment	1.2 (12/1098)	Buller et al (2004) ²⁵
	ACS	2.2 (217/10,057)	Yusuf et al (2006) ²⁶
DTI			
Lepirudin ^b	HIT	18.8 (21/112)	Greinacher et al (2000) ²⁷
Argatroban	HIT	6.1 (14/229)	Lewis et al (2003) ²⁸
Bivalirudin	ACS with PCI	3.5 ^c (82/2318)	Ebrahimi et al (2005) ²⁹

UFH indicates unfractionated heparin; VTE, venous thromboembolism; ACS, acute coronary syndrome; LMWH, low-molecular-weight heparin; DTI, direct thrombin inhibitors; HIT, heparin-induced thrombocytopenia; PCI, percutaneous coronary intervention.

^aBleeding rates were obtained from meta-analyses or pivotal clinical trials. A major bleed was most often defined as intracranial, fatal, retroperitoneal, intraocular, or needing surgical intervention, with or without the need for transfusion. Individual trials used different definitions of major bleeding.

^bThe dosing regimen previously used in the approval trials for lepirudin for treatment of HIT is now considered too high,³⁰⁻³³ and currently dosing less than that stated in the package insert is recommended.³⁴

^cPatients undergoing PCI are at additional risk for bleeding compared with patients treated with antithrombotic therapy alone.

heparin/ATIII complex. Inactivating thrombin not only stops further fibrin formation, but also blocks thrombin-induced activation of platelets and Factors V and VIII. The preferred routes of administration for heparin are IV or SC, although SC administration requires a higher dose because of reduced bioavailability. In the bloodstream, UFH binds to various proteins, including endothelial cells and macrophages, which reduces anticoagulant activity and contributes to its nonlinear clearance kinetics and variability in treatment among patients with thrombotic disorders. Therefore, the anticoagulant effect of heparin must be monitored using the activated partial thromboplastin time (aPTT), a test that measures the time it takes blood to clot as an indicator of coagulation function, or Factor Xa activity and adjusted to remain within the therapeutic range – 1.5 to 2.5 the control aPTT time or 0.3 to 0.7 U/mL by Factor Xa inhibition. Another limitation of UFH outside its well-known bleeding risk is its ability to induce immune-mediated platelet activation, known as heparin-induced thrombocytopenia (HIT), which actually puts the patient at risk for thrombosis. Despite its drawbacks, UFH is one of the only anticoagulants with a clinical antidote, protamine, which can be administered intravenously to rapidly reverse its anticoagulant effects. This benefit, in addition to decades of clinical experience, accounts for UFHs permanence for hospital use, particularly in critical care applications such as cardiology procedures.⁴¹

The development of low molecular weight heparin (LMWH) has led to several improvements on the pharmacology of heparin therapy. LMWHs (enoxaparin, dalteparin, tinzaparin) are typically prepared by chemical or enzymatic depolymerization of UFH, although related synthetic forms have also been developed (i.e. fondaparinux), and have a mean molecular weight of 4000-5000 kDa. LMWHs demonstrate reduced binding to protein and cells, which leads to more predictable pharmacokinetics and anticoagulant activity relative to UFH. This

reduced binding to endothelial cells contributes to a longer plasma half-life, whereas reduced binding to platelets may explain the lower incidence of HIT. Like UFH, LMWHs still produce their anticoagulant effect by complexing with ATIII. The shorter chain length limits their ability to directly inactivate thrombin, but does not affect their ability to mediate Factor Xa inhibition. Unfortunately, the shorter chains may also underlie the ineffectiveness of protamine as an antidote for LMWHs; in fact, no clinically-approved antidotes currently exist. LMWHs have been evaluated in a large number of clinical trials and are generally at least as safe and effective as UFH for the indications tested. Additionally, the predictable dose-response relationship typically precludes the need for monitoring blood levels. This feature combined with their near complete bioavailability when administered SC has facilitated the switch from UFH to LMWHs in many hospital applications where immediate reversibility is not critical. LMWHs are also contraindicated in select patient populations, including obesity and renal failure, where the disease physiology interferes with the clearance of the drug.

While UFH and LMWHs comprise the class of indirect thrombin inhibitors, direct thrombin inhibitors (DTI), which have the ability to independently block thrombin without the aid of any cofactors, are an emerging class of anticoagulants. Unlike heparin which cannot inhibit fibrin-bound thrombin, DTIs can inhibit both soluble and fibrin-bound thrombin, although the clinical importance of the characteristic is unclear.^{42, 43} DTIs also have several other advantages over heparins including more predictable dose-response due to their lack of binding to plasma proteins, little to no platelet interactions, and absence of immune-mediated thrombocytopenia.^{44, 45} There are currently four clinically-approved parental DTIs: lepirudin, desirudin, argatroban, and bivalirudin. Lepirudin and desirudin are recombinant derivatives of hirudin, a peptide found in the salivary glands of medicinal leeches. Bivalirudin is a synthetic

polypeptide analog of hirudin, while argatroban is a small molecule (527 kDa) inhibitor; both these drugs reversibly inhibit thrombin. DTIs are primarily used in patients with or at risk for HIT, however their indications continue to expand as more clinical studies are completed. While some of these studies have shown incremental improvements in efficacy over heparins, risk of major bleeding remains a significant risk, especially because none of the DTIs have a clinical antidote.^{42, 43}

A number of other coagulation factors from the intrinsic pathway have emerged as interesting candidates for anticoagulant therapy. Blocking FIXa may be an important step in preventing thrombosis because formation of the FVIIIa/FIXa complex is an upstream and rate-limiting step of several positive feedback loops that drive the propagation of thrombin generation.⁴⁶ The REG1/REG2 anticoagulation systems are the most advanced FIX/FIXa inhibitors in development and have progressed to clinical trials.^{47, 48} These systems are derived from aptamers, or short oligonucleic molecules that bind specific molecular targets, which have the attractive feature of readily available control antidotes in the form of the complementary oligonucleotide to the anticoagulant strand.⁴⁹⁻⁵¹ FXIa and FXIIa have become targets of anticoagulant therapy following studies demonstrating thromboprotection against different experimental models of thrombosis in mice lacking either factor.⁵²⁻⁵⁵ In humans, FXI deficiency (hemophilia C) is associated with a mild bleeding phenotype, while FXII deficiency does not exhibit a clinically relevant phenotype; the relationship between these deficiencies and thrombosis needs to be further studied.^{56, 57} Though targeted disruption of intrinsic coagulation is untested in clinical medicine and may exert physiological effects beyond coagulation, these observations provide hope that inhibiting FXIa and FXIIa may prevent thrombosis while

minimizing the interference with haemostasis. Several pharmacological agents that inhibit FXIa and FXIIa are currently in preclinical development.^{58, 59}

Oral anticoagulants

Long-term anticoagulation is necessary for thrombosis prevention following numerous conditions, including myocardial infarction, stroke, DVT/PE, and atrial fibrillation. For chronic use, patients typically transitioned from parenteral to oral anticoagulants, given the clear advantage in ease of administration. Vitamin K antagonists (VKAs), namely warfarin, have been the mainstay of oral anticoagulation for over 60 years.⁶⁰ Warfarin interferes with the interconversion of Vitamin K and Vitamin K epoxide, impairing the Vitamin K-dependent synthesis of thrombin and Factors VII, IX, and X and resulting in the production of inactive forms of these proteins. Warfarin also affects the synthesis of regulatory anticoagulant proteins C, S, and Z and may temporarily act as a procoagulant, though the anticoagulant effect is dominant under most circumstances.⁶¹ Achieving optimal levels of anticoagulation is challenging because of its narrow therapeutic index, slow onset of action, variable pharmacologic effects, and multiple drug and diet interactions. Studies have shown that 44% of bleeding complications with warfarin therapy were associated with supratherapeutic levels of anticoagulation and that 48% of thromboembolic events occurred with subtherapeutic levels.^{60, 62} Therefore, monitoring anticoagulation intensity (most commonly using the prothrombin time assay) and dose titration is critical and may necessitate frequent visits to outpatient clinics for patients who are not in the hospital.⁶⁰ In cases of excessive anticoagulation or bleeding, the effects of warfarin can be reversed with oral or intravenous administration of Vitamin K. If immediate reversal is necessary, supplementation of clotting factors with fresh frozen plasma or prothrombin complex

concentrate is more effective.⁶³ The limitations of warfarin have greatly affected its safety, compliance, and efficacy.

The multitude of challenges associated with the usage of warfarin has fueled the extensive research and development of a new generation of oral anticoagulants. The first group of drugs to receive approval for clinical use includes a DTI (dabigatran) and several direct Factor Xa inhibitors (rivaroxaban, apixaban, edoxaban).^{64, 65} These drugs offer improved safety, efficacy, and ease of use compared to warfarin because of their favorable pharmacological properties. Unlike warfarin, which takes four to five days to reach its peak effect, these drugs reach their peak effects on the order of one to three hours. More predictable pharmacokinetics and dose response allows patients to follow fixed dosing regimens without the need for monitoring. The chemistry of these new drugs also results in fewer drug and dietary interactions. These novel anticoagulants have several disadvantages including the current lack of reliable monitoring methods in cases of suspected toxicity, lack of antidotes for life-threatening bleeds or urgent surgery, and contraindications for specific patient groups such as those with chronic kidney disease or prosthetic heart valves.⁶⁶ Though these drugs continue to gain approval for broader indications, clinicians have approached their use with caution because of their associated risk of bleeding and current lack of reversal methods – clinical studies of these drugs have shown equal to significantly higher risk of bleeding relative to the standard-of-care.⁶⁷⁻⁶⁹

1.2.4.2 Antiplatelets

Antiplatelets are drugs that target molecules involved in platelet activation or aggregation; they are used for both the prevention and acute treatment of arterial thrombosis.⁹ Aspirin is the most commonly used antiplatelet drug, having been utilized in the clinic for over 40 years. By inhibiting cyclooxygenase-1 enzymes, aspirin blocks the synthesis of thromboxane

A₂, a potent activator of platelets. Aspirin reduces the incidence of first myocardial infarction in men at risk of cardiovascular disease as well as patients who have had a myocardial infarction. However, taking aspirin does not guarantee prevention of thrombotic events, with substantial cohorts of patients display 'aspirin resistance', and can cause stomach ulcers and bleeding.⁹

Several other classes of antiplatelet drugs have been studied and developed in since the discovery of aspirin. Adenosine 5'-diphosphate (ADP) receptor antagonists target the receptor P2Y₁₂, which prevents ADP from activating platelets. Clopidogrel (Plavix™) and prasugrel (Effient™) are the most widely used drugs in this class and have been shown to be more effective than aspirin.^{9, 70} Dual antiplatelet therapy combining ADP receptor antagonists and aspirin are being explored for their potential synergistic effects.⁷¹ Another class of drugs are $\alpha_{IIb}\beta_3$ integrin inhibitors reduce platelet aggregation by blocking the binding of activated platelets to fibrinogen and other ligands. Unlike the other antiplatelet drugs that are administered orally, the $\alpha_{IIb}\beta_3$ inhibitors that are current used in the clinic, such as abciximab (ReoPro™), eptifibatide (Integrilin™), and tirofiban (Aggrastat™), are delivered intravenously. They are used for short-term treatment of patients with acute coronary syndromes who are undergoing percutaneous coronary intervention.^{71, 72}

Numerous other oral and intravenous antiplatelet drugs are currently in various phases of development, some of which focus novel targets such as protease-activated-receptor-1 (PAR1), phosphatidylinositol 3-kinase (PI3K), and glycoprotein VI or Ib.⁷³ Safer and more effective drugs will undoubtedly continue to arise as researchers continue to understand the biology underlying platelet activation. Nevertheless, these therapeutics are designed the block platelet activities that are critical pathways in haemostasis as well as thrombosis, therefore similar to

anticoagulants, the risk of potentially fatal bleeding remains one of the adverse effects of primary concern for all antiplatelet drugs.

1.2.4.3 Thrombolytics

Thrombolytic agents, also referred to as ‘clot busters’, are agents that activate plasminogen to form plasmin, which lyses existing thrombi, in order to limit the damage caused by occlusion of a blood vessel.^{9, 74} They are used to treat severe manifestations of thrombotic disorder, including acute myocardial infarction, stroke, DVT, and acute PE. Since these drugs activate the fibrinolytic system, which does not distinguish between haemostatic and thrombotic clots, thrombolytic agents also greatly increase the risk of major bleeding. Therefore, the indications and potential benefits must be carefully weighed against the risk of adverse events before undergoing this therapy. Thrombolytic agents currently used in the clinic include recombinant tissue type plasminogen activator (alteplase, reteplase, tenecteplase), streptokinase, and urokinase.^{74, 75} The success of these agents heavily depends on the timing of the intervention, with earlier treatment generally leading to better outcomes. For example, thrombolytic therapy for stroke is most beneficial when used within three hours and can lead to severe brain hemorrhage.⁷⁶ Therefore, strategies that protect the vasculature with a lower incidence of bleeding are highly important.

1.2.5 Nanomaterials for Treating Thrombosis

The application of nanotechnology to the treatment of thrombosis is a rapidly growing field of interest and a number of approaches addressing various limitations of anticoagulant therapy have been demonstrated in the literature. Much effort has been directed towards improving alternative non-parental routes of administration for UFH and LMWH by improving

oral bioavailability through encapsulation in polymeric or solid lipid nanoparticles,^{77, 78} or reformulating with dendrimer carriers for nasal/pulmonary delivery.⁷⁹ Others have utilized the capacity of nanoparticles for multivalent presentation to improve anticoagulant binding to their targets, thereby potentially lowering the required dosage and improving their therapeutic index. Such strategies also have the added effect of increasing the circulation half-life of small molecular species, which may be beneficial for prophylactic usage. Direct thrombin inhibiting peptides, bivalirudin and PPACK, conjugated to the surface of liposomes or perfluorocarbon nanoparticles demonstrated improved binding efficiency to thrombin and longer circulation times relative to their free peptide forms.^{80, 81} When conjugated to gold nanoparticle scaffolds, thrombin-targeted aptamers also showed improvement in binding and inhibition.⁸²⁻⁸⁴ Finally, the addition of affinity ligands that direct anticoagulant nanoparticles to potential high-risk thrombotic sites, such as atherosclerotic plaques, and increase their local concentration could further improve their efficacy and therapeutic index.⁸⁵

Nanomaterials have been utilized in thrombolytic therapy for targeted delivery of therapeutic moieties to sites of action in order to reduce the dose required for efficient clot lysis and off-target effects with the hopes of decreasing deleterious side effects such as bleeding. Indeed, intracerebral hemorrhage is among the most serious and potentially fatal bleeding associated with thrombolysis, and occurs in 1% of treated patients with myocardial infarction and 6% of treated patients for stroke.⁸⁶ Iron oxide nanoagents attached to plasminogen activators have been targeted to thrombi using external magnetic fields and demonstrate increased thrombolytic potential relative to their free counterparts.^{87, 88} Nanoparticles bearing plasminogen activators have also been actively targeted to thrombi using affinity ligands such as anti-fibrin antibodies or FXIIIa-sensitive peptides.^{89, 90} Another notable strategy is the development of

shear-activated nanoparticles, coated with plasminogen activator, that are designed to deliver drugs to blood vessels obstructed by thrombosis, which have abnormally high fluid shear stress.⁹¹ This biophysical targeting approach demonstrated rapid clot dissolution in mouse models of thrombosis with lower required doses and fewer side effects than free plasminogen activator. While these technologies offer promising improvements to antithrombotic care, as of this writing, none have yet reached clinical testing, which suggests that further preclinical studies may be needed.

1.3 Cancer

In 2012, cancer accounted for 8.2 million deaths worldwide, placing it among the top three causes of death. The projected number of annual cancer cases is projected to rise from 14 million in 2012 to 22 million within the next two decades.⁹² Cancer is a term for a large group of diseases that can affect any part of the body. The disease can arise from single cells that progress from normal to malignant states through a multistage process.⁹³ The defining feature of most cancers is the unchecked growth of the abnormal cells that can then invade adjoining regions of the body and spread to other organs. Cancer is caused by the interaction of numerous factors, including one's genetics, external carcinogens, and aging. Well-documented risk factors include tobacco use, obesity, unhealthy diet, alcohol use, and air pollution. Overcoming the rising rates of cancer will require population-wide changes in behavior, improved technologies for early detection, and more effective treatments.

Diagnosis of cancer generally progresses from a macro-scale assessment of patient well-being towards more accurate, yet potentially invasive, diagnostic assays for confirming disease presence. Patients suspected of having cancer, either through cancer screening tests or a physical exam revealing common symptoms (e.g. weight loss, fatigue, nausea, pain), undergo blood

testing and imaging to probe physiological and structural changes in the suspected region of disease.⁹⁴ Serological analysis of cancer-associated biomarkers continues to evolve as our molecular understanding of cancer improves, however these tests generally cannot provide a definitive diagnosis in isolation.⁹⁵ Imaging modalities used for cancer, including x-ray, MRI, single-photon computed tomography, positron emission tomography, and optical imaging, provide structural and physiological information that may guide subsequent biopsies of suspected lesions.⁹⁶ These present detection threshold for solid tumors is approximately 10^9 cells, which limits the ability of imaging methods to detect early stage disease. Finally, a biopsy is used to remove tissue from the suspected site of disease as well as neighboring lymph nodes for a direct molecular diagnosis of cancer. Histopathological methods are used to ‘grade’ and ‘stage’ the disease by detecting molecular cancer markers, identifying the tissue of origin, and assessing evidence of metastasis, the main cause of cancer-associated death. These factors play an important role in formulating a treatment plan.

Surgery, radiation, and chemotherapy are the most common forms of cancer treatment and are often used in combination. Surgical removal of tumor masses can be highly effective in preventing further spread of disease, especially if performed before metastasis has occurred. In situations where surgery is unsuitable, radiation and chemotherapy have served as the primary tools for fighting cancer. Radiation therapy uses ionizing radiation, administered extracorporeally or internally via brachytherapy, to locally kill tumor cells while minimizing damage to the surrounding normal tissues.⁹⁷ The limitations of radiation are well-documented and include a range of side effects related to exposure of healthy tissue/organs and the inability to treat highly disseminated disease. Chemotherapy generally refers to the administration of cytotoxic agents that target rapidly dividing cells, one of the main properties of cancer. The main

classes of chemotherapeutics include alkylating agents, anti-metabolites, anti-microtubules, and topoisomerase inhibitors.⁹⁸ However, rapid cell division is not an exclusive feature of tumors and systemic exposure of these compounds leads to a range of off-target effects including hair loss, decreased bone marrow proliferation, infertility, nausea, fatigue, and impaired digestive function.

Despite the immense progress in fundamental cancer biology over the past quarter century, comparable advances in clinical treatment have yet to emerge. Molecular approaches such as targeted therapies and cancer immunotherapy have shown great promise in treating certain cancer types, but a majority of our pharmacological arsenal still relies on small molecule chemotherapeutics.⁹⁹⁻¹⁰¹ A key challenge limiting the efficacy of systemic agents for cancer therapy is that as little as 1% or less of an injected drug reaches its target *in vivo*; the remaining 99% distributes in normal tissues, causing adverse effects that frequently restrict dosing to sub-therapeutic levels and lowering the barriers to drug resistance.¹ Nanotechnology may offer the tools needed to one day overcome this challenge.

1.3.1 Transport in Solid Tumors

Over 80% of cancers are solid tumors that grow as a mass of cells in a particular organ or tissue. The abnormal structure and composition found in these tumor microenvironments has a profound impact on cancer treatment. The rapid proliferation of cancer cells forces vessels apart, reducing vascular density and creating a population of cells distant from blood vessels. This process is exacerbated by the poorly organized vasculature architecture, heterogeneous and irregular blood flow, and the compression of blood and lymphatic vessels. Furthermore, the disorganized vasculature and lack of functional lymphatics causes increased interstitial fluid pressure (IFP), which opposes convective transport of agents from blood to tumor. Finally, the

composition and structure of the extracellular matrix (ECM) can slow the movement of molecules within tumors.^{102, 103}

One of the primary barriers to the delivery of a blood-borne molecule is the extravasation of the molecule from blood vessel to tumor interstitium. This process is governed by diffusion, convection, and presumably transcytosis. Diffusion is proportional to vessel surface area (S) and the difference between plasma (C_v) and interstitial (C_i) concentrations. Convection is proportional to S and the difference between the vascular (P_v) and interstitial (P_i) hydrostatic pressures, minus the osmotic reflection coefficient (σ) times the difference between the vascular (π_v) and interstitial (π_i) osmotic pressures. The diffusion flux is related to the concentration gradient by the vascular permeability coefficient (P) and the convection is related to the pressure gradient by the hydraulic conductivity (L_p).¹⁰³

$$\begin{aligned} \text{Diffusion} &= PS(C_v - C_i) \\ \text{Convection} &= L_p S [(P_v - P_i) - \sigma(\pi_v - \pi_i)] \end{aligned}$$

In normal tissues, convection is the dominant mode of transport for macromolecules, whereas diffusion is more important for small molecules.¹⁰⁴ However, the situation in tumors can be significantly different because of vascular leakiness and interstitial hypertension. Larger pore sizes in tumors may represent wider interendothelial junctions.^{105, 106} Despite increased overall permeability, not all blood vessels are leaky. Not only does vascular permeability vary from one tumor another, but also spatially and temporally within the same tumor.¹⁰³ Several studies have indicated that convection is not the dominant mode of transport in non-peripheral regions of solid tumors, where the microvascular pressure is nearly equal to the interstitial fluid pressure.^{104, 107, 108} Convection may still play a crucial role in drug delivery to peripheral tumor tissues, where a significant drop in interstitial tumor pressure occurs.¹⁰⁹ This pressure gradient facilitates

extravasation of macromolecules in the periphery; consequently, higher accumulation of macromolecules may be observed at the interface between tumor and normal tissues.^{103, 109}

Tumor vessel permeability may be increased by enhancing the local concentration of vasopermeability cytokines such as VEGF, IL-2, or TNF. These signaling molecules increase the physical permeability of the vasculature by inducing the formation of fenestrations within endothelial cells or increasing the size of intercellular gaps.¹¹⁰⁻¹¹² Systemic administration of IL-2 peptides fused with tumor targeting antibodies can specifically increase permeability of the tumor vasculature leading to increased tumor uptake and therapeutic efficacy of subsequently administered drugs.^{113, 114} Many physical methods of modulating vessel permeability have been demonstrated, including intravascular infusion of hyperosmolar solutions¹⁰⁴ and hyperthermia.¹¹⁵⁻¹¹⁸ However, one potential danger of increasing vascular permeability is the possible increase in metastasis as tumor cells may be able to intravasate more easily.^{119, 120}

Another approach to increasing transvascular flux involves increasing perfusion or convection rather than macromolecular permeability. Pharmacological agents can be used to increase blood pressure, which has been shown to increase perfusion by opening collapsed vessels and convective flow into tumors; these responses are typically short-lived as tumor and vessel pressures rapidly equilibrate.¹²¹⁻¹²⁴ Others have increased convection into tumors by reducing tumor IFP through radiation, PDGF inhibitors, and other pharmacological agents.¹²⁵⁻¹²⁸ The reduced IFP has been shown to increase tumor uptake of co-administered small molecules and antibodies, although the effect is also transient.

Enhanced tumor perfusion and convection may also be achieved by vascular ‘normalization’ with anti-angiogenic drugs.^{129, 130} Inhibiting pro-angiogenic signaling molecules in tumors causes tumor vasculature to take on a more normal physiology including reduce hyper-

permeability, reduced IFP, increased vessel perfusion, and increased transcapillary convection.¹³¹⁻¹³³ These changes have led to increases in tumor penetration and therapeutic efficacy of subsequently administered small molecules.^{132, 134} But due to decreases in vessel permeability, ‘normalization’ may be less effective at increasing uptake of larger macromolecules such as antibodies.^{133, 135}

1.3.2 Nanoparticles for Cancer Therapy

For nanodelivery vehicles to be effective, they must escape renal and reticuloendothelial clearance, home to the site of disease, and extravasate out of the blood vessel and into the tumor interstitial space, before binding to the cellular target. Nanoparticles offer unique properties that enable cancer-specific delivery of therapeutic and imaging agents. They exhibit minimal renal filtration and favorable pharmacokinetic profiles, have large surface area to volume ratios which allows functionalization with targeting moieties, and can be constructed from different materials to either encapsulate therapeutics or to provide optical, magnetic, and electrical properties for diagnostics. Many nanomaterials have been successfully utilized for drug delivery, including liposomes, polymeric nanoparticles, dendrimers, and micelles.^{2, 136, 137} While a number of these nanoparticle-based systems have been approved for cancer imaging and therapy,¹³⁸⁻¹⁴¹ developing biocompatible and well-characterized systems that demonstrate significant differential uptake efficiency in malignant tissue over normal tissue remains an ongoing challenge to rapid and effective clinical translation.

Several nanoparticle-based therapeutics, including DoxilTM, DaunoXomeTM, and AbraxaneTM, are currently FDA-approved for clinical use in oncology.³ Doxil utilizes pegylated liposomes to increase the stability of doxorubicin and prolong its release; similarly, DaunoXome is a liposomal formulation of the drug daunorubicin. Abraxane uses nanoparticulate albumin to

increase the half life of paclitaxel. Since liposomes are formed through the self-assembly of individual lipids, they can be decorated with tumor targeting ligands or imaging contrast agents¹⁴². Biodegradable polymers such as poly(lactic-co-glycolic acid) (PLGA) and polymerosomes can be engineered into nanoparticles that slowly releases the encapsulated drug overtime.^{143, 144} Various lipid-based polymers can also be combined into a “nanocell” to achieve temporally and spatially controlled release of multiple drugs.¹⁴⁵ Dendrimers, polymers with repeatedly branching structures surrounding an inner core, are yet another nanoparticle formulation for drug delivery applications. They can be functionalized and encapsulate drugs for cancer cancer targeting, imaging and treatment.¹⁴⁶⁻¹⁵⁰

The intrinsic therapeutic properties of nanomaterials have also been harnessed in cancer therapy. Examples include gold nanoshell and nanorod-mediated heat generation upon near-infrared irradiation, which damages the tumor tissue via local hyperthermia.^{151, 152} Despite innovations in nanoparticle-based drug delivery, a comparatively small number of passively-targeted nanomaterials have been successfully translated to the clinic. To achieve the tumor specific delivery with no off-target effects, new delivery paradigms and more selective targets are required.

The ability to target therapeutics to sites of disease while avoiding uptake by healthy organs could dramatically improve treatment efficacy and minimize side effects.¹⁵³⁻¹⁵⁵ By encapsulating cargoes that are otherwise rapidly cleared by the body, nanoparticles can function as useful carriers to increase the cargo size above the renal filtration limit, prolong circulation time, and maximize tumor uptake. Furthermore, the unique molecular signature of the tumor microenvironment, including cell-surface receptors, blood vessel and tumor lymphatic markers,

extracellular matrix, soluble factors, and tumor transport characteristics may be exploited for targeting.¹⁵⁶⁻¹⁵⁹

Nanoparticle targeting to tumors is achieved through passive or active targeting mechanisms. Passive targeting utilizes the unique structural and transport characteristics of the tumor vasculature, a phenomenon known as the enhanced permeability and retention (EPR) effect¹⁶⁰. In this mode of targeting, nanoparticles extravasate out of the vasculature into the tumor interstitium through large, poorly-formed pores and are retained at the site of disease due to a lack of functional lymphatics in solid tumors.^{106, 157, 160-162} Therefore, by extending the circulation half-life of a nanoparticle, one can improve passive accumulation by affording the particles more time to escape from the leaky vasculature into the tumor.¹⁶³⁻¹⁶⁵

Active targeting exploits ligand-directed binding of nanoparticles to unique receptors in the tumor microenvironment.¹⁶⁶⁻¹⁶⁸ These ligands include small molecules,¹⁶⁹ antibodies,^{149, 170} and aptamers.^{139, 171} Novel screens using bacteriophage-displayed peptide libraries have also identified peptides that have extraordinary tumor homing specificity.^{138, 172} The efficacy of actively targeted delivery is still heavily debated as recent studies have suggested that particle accumulation is largely governed by EPR, while tumor-specific ligands direct binding of nanoparticles to cancer cells and alter intra-tumoral distribution after they have extravasated from the tumor endothelium.¹⁷³⁻¹⁷⁶ However, this hypothesis may not apply to active targeting of the tumor vasculature as extravasation from vessels is not required. Vascular targets for nanoparticle systems have included vascular endothelial growth factor receptors (VEGFRs), $\alpha_v\beta_3$ integrins, matrix metalloproteinases receptors (MMPs), and vascular cell adhesion molecule-1 (VCAM-1).¹⁷⁷ Another promising solution is the recent discovery of a class of tumor-specific and tissue penetrating peptides.^{178, 179} These peptides contain a tumor targeting motif (e.g. $\alpha_v\beta_3$

integrin RGD sequence) and an arginine/lysine-X-X-arginine/lysine (RXXR) motif that is unveiled through proteolytic processing on the C-terminus, which then binds to neuropilin-1 and facilitates a subsequent increase in tumor tissue permeability and enhancement in cargo delivery.

A further limitation of active targeting strategies that is applicable even to vascular targeted systems is the number of accessible target receptors or antigens. As the dosage of a targeted nanocarrier is increased, the number of available receptors or targets will eventually become saturated, and additional increases in dosing will not result in further targeted delivery.¹⁸⁰ The remaining nanocarriers must selectively accumulate in tumor tissue based solely on passive targeting, potentially leading to a smaller proportion of the administered dose reaching the desired site.¹⁸¹

1.3.3 Systems of Nanoparticles for Amplified Delivery

A common characteristic in both passive and active targeting approaches is that nanoparticle designs are engineered at the scale of individual particles by tuning properties such as particle shape, size, surface chemistry, and ligand type and abundance.²⁻⁴ In contrast, biological systems in nature generate complex behaviors through interactions between multiple components across molecular, cellular, organismal, and/or even populational length scales to enable emergent functions such as computation, communication, and amplification. The rapid tissue repair response initiated by blood coagulation is a representative example of higher-order coordination of countless nanoscale interactions that culminates in the targeted formation of a platelet-fibrin plug at the site of injury.⁹ Inspired by these natural biological systems, our laboratory has pursued a systems engineering approach to designing interaction, communication, and cooperativity between nanoparticles and other biological or synthetic components to amplify delivery to tumors (**Figure 1.2**).

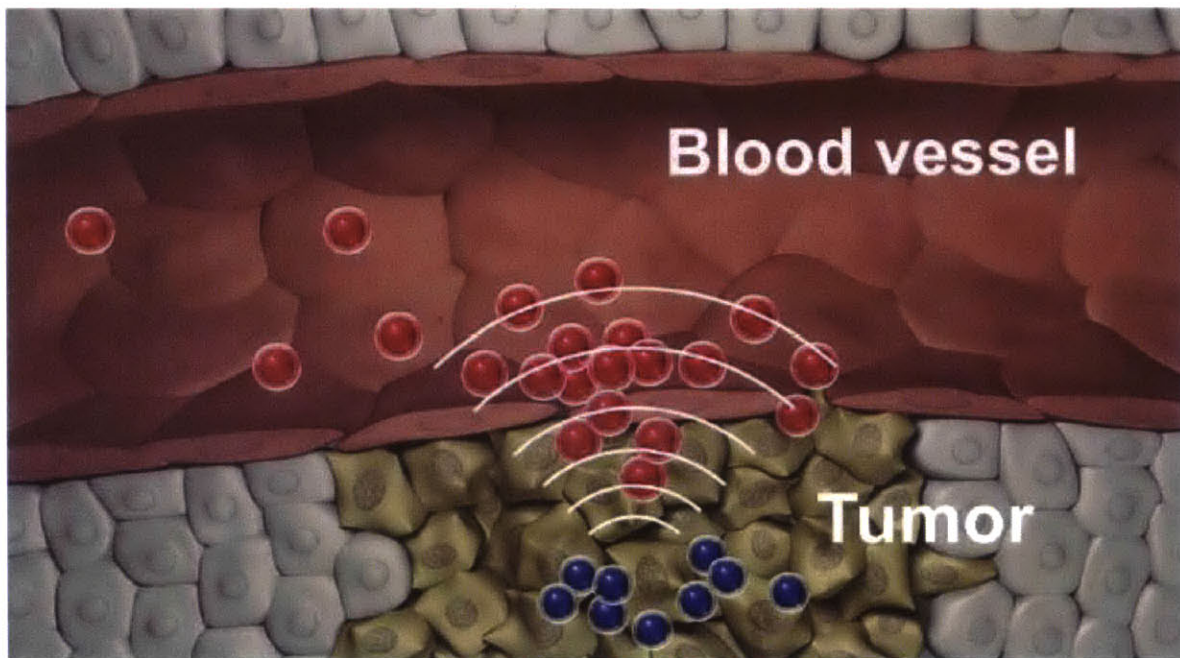


Figure 1.2. Nanoparticle communication for amplified tumor targeting.¹⁸²

In the first formulation of this cooperative strategy, intravenously-injected gold nanorods that passively target xenograft tumors in mice were remotely heated by an external near-infrared laser, which activated the coagulation cascade in tumor vessels to generate an abundant biochemical signal for a second population of clot-targeting nanoparticles.^{151, 182} In the second formulation, external heating of gold nanorods was again utilized to heat the tumor microenvironment, in this case to induce the expression of a tumor-specific stress receptor called p32.^{183, 184} This receptor then served as an abundant protein signal for a second population of p32-targeting nanoparticles.¹⁸⁵ These cooperative strategies amplified the tumor delivery of drug-loaded nanoparticles by 10-40 times and significantly reduced the growth of tumor xenografts in a preclinical therapeutic trial.

These systems demonstrate the immense potential of a systems approach to nanoparticle targeting, however the use of gold nanorod-mediated heating requires an exogenous light input and precise knowledge of the tumor location, which precludes application of these approaches to the treatment of metastatic cancer. The objective in Chapter 3 of this thesis is to build upon this cooperative targeting approach to amplify nanoparticle delivery by using a more clinically relevant, systemically-administered inducer of target receptors: a vascular disrupting agent.

1.3.4 Vascular Disrupting Agents

The growth and survival of cancer cells depends on the establishment and expansion of the tumor blood vessel network to deliver oxygen and nutrients. Consequently, the tumor vasculature has become an attractive target for new approaches to cancer therapy. Much attention has been given to the development of anti-angiogenic approaches, which aim to curtail the process of neovascularization, which has resulted in the clinical approval of the first anti-angiogenic therapeutics: bevacizumab (Avastin), sorafenib (Nexavar), and sunitinib (Sutent).¹⁸⁶

An alternative strategy, based on the recognition of unique vascular characteristics and abnormalities in structure of tumors, aims to rapidly and selectively shutdown established vasculature, leading to secondary tumor-cell death through depletion of oxygen and nutrients and build-up of waste products.¹⁸⁷ These agents have aptly been named vascular disrupting agents (VDAs).

Small molecule VDA's can generally be divided into two subclasses: agents related to flavones acetic acid (FAA) and 5,6-dimethylxanthenene-4-acetic acid (DMXAA) and tubulin-binding agents related to combretastatin. While the mechanism of action of FAA and DMXAA is still poorly understood, their main effect on vascular endothelial cells is thought to involve a cascade of effects, including the induction of cytokines, such as TNF- α , leading to the induction of hemorrhagic necrosis in tumors as a result of vascular collapse.¹⁸⁸ Tubulin-binding agents are believed to selectively disrupt the cytoskeleton and cell-to-cell junctions of proliferating endothelial cells, resulting in endothelial cell shape changes that lead to loss of blood flow.^{187, 189,}
¹⁹⁰ Loss of cell-to-cell contact leads to increased vascular permeability to proteins and increased interstitial fluid pressure, which may be sufficient to reduce vessel diameter.¹⁹⁰⁻¹⁹² Plasma leakage leads to increased blood viscosity, resulting in decreased blood formation and rouleaux formation.¹⁸⁷ Exposure of the already often abnormal basement membrane results in platelet activation and the induction of the coagulation cascade with subsequent thrombus formation.¹⁸⁹ This cascade of events promotes vascular shutdown more selectively in tumor endothelium than normal endothelium. The lead combretastatin compound is disodium combretastatin A-4 3-O-phosphate, the prodrug of combretastatin A-4 that has advanced the furthest into clinical trials of all small molecule VDAs thus far.¹⁹³⁻¹⁹⁷

Numerous VDAs have already entered Phase I through Phase III of clinical trials.^{187, 198}

As a single treatment modality, VDA-treated tumors consistently display massive central necrosis marked by the survival of a thin viable rim around the tumor periphery. This viable peripheral rim is attributed to areas at the edge of the tumor being nutritionally supported to some extent by vessels in the neighboring normal tissues.¹⁸⁶ The greatest potential of VDAs lies in their combination with conventional therapies, and trials on these combination regimes are already underway. Conventional chemotherapeutics and radiation are effective against highly proliferating and well-oxygenated cells, which are more evident at the periphery of tumors. Additionally, blood flow is more effective at the periphery, allowing greater access to systemic anticancer agents. Thus, the rationale for combining VDAs with conventional treatments is clear and preclinical studies provide evidence of efficacy for combretastatin-A4-P, DMXAA, and other VDAs with a range of agents from radiation to platinum drugs and taxanes.¹⁹⁹⁻²⁰⁵

Scheduling is an important consideration in these combination treatments in light of the rapid tumor vascular shutdown that occurs after VDA treatment. It was initially considered best to avoid administering radiotherapy or chemotherapy shortly after VDA administration when blood flow to tumor regions that will likely survive VDA treatment is reduced. These areas may be hypoxic, and therefore more resistant to radiotherapy, as well as less-accessible to blood-borne chemotherapeutics. These considerations were elaborated in preclinical trials and applied to clinical trials involving combretastatin-A4-P.^{199, 202, 205} However, more recent studies have highlighted the potential benefit of administering chemotherapy after VDA pretreatment in order to leverage the enhanced vascular permeability to increase tumor delivery of drugs as well as avoid the antagonizing effects that certain drug classes (e.g. microtubule-stabilizing agents like paclitaxel) may have on VDA efficacy.^{206, 207} Identifying the optimal sequence and timing for

administering VDAs in combination therapy remains a critical component that must be further refined in order to realize the potential of this novel class of therapeutics.

1.4 Scope of the Dissertation

The aim of this thesis is to engineer nanoparticle systems that interact and exploit aspects of the host anatomy and biology *in vivo* to perform novel functions that ultimately improve the diagnosis and treatment of thrombosis and cancer. In Chapter 2, nanoparticles are engineered to *sense* dysregulated protease activity associated with thrombosis and generate reporters that can be noninvasively quantified in the urine. Chapter 3 describes the development of nanoparticles that homeostatically *regulate* the biological cascade responsible for haemostasis to prevent the aberrant formation of clots. And finally, Chapter 4 investigates a two-component system whereby the first therapeutic entity upregulates a molecular signal within a malignant environment to *amplify* the local recruitment of a secondary population of targeted nanoparticles. Together, these systems highlight the potential for interactive nanoparticle systems to perform highly complex tasks *in vivo* by leveraging and modulating endogenous biological processes.

Chapter 2: Nanoparticles that Sense Thrombin Activity as Urinary Biomarkers of Thrombosis

2.1 Abstract

Thrombin is a serine protease and regulator of haemostasis that plays a critical role in the formation of obstructive blood clots, or thrombosis, that is a life-threatening condition associated with numerous diseases such as atherosclerosis and stroke. To detect thrombi in living animals, we design and conjugate thrombin-sensitive peptide substrates to the surface of nanoparticles. Following intravenous infusion, these ‘synthetic biomarkers’ survey the host vasculature for coagulation and in response to substrate cleavage by thrombin, release ligand-encoded reporters into the host urine. To detect the urinary reporters, we develop a companion 96-well immunoassay that utilizes antibodies to bind specifically to the ligands, thus capturing the reporters for quantification. Using a thromboplastin-induced mouse model of pulmonary embolism, we show that urinary biomarker levels differentiate between healthy and thrombotic states and correlate closely with the aggregate burden of clots formed in the lungs. Our results demonstrate that synthetic biomarkers can be engineered to sense vascular diseases remotely from the urine and may allow applications in point-of-care diagnostics.

2.2 Introduction

Urine analysis has a rich and longstanding clinical history as a tool for monitoring health and disease, and remains an integral component of a medical examination.²⁰⁸⁻²¹⁰ Well over one hundred tests can be performed to indicate conditions as diverse as pregnancy,^{211, 212} diabetes,²¹³⁻²¹⁶ kidney diseases,²¹⁷⁻²¹⁹ metabolic disorders,^{220, 221} and others. Recently, the discovery of urinary analytes that were previously thought to be present mainly in circulating blood because

of their large hydrodynamic radii (e.g. enzymes, exosomes and others) has expanded the diagnostic repertoire to include urinary biomarkers against diseases of distant organs such as breast and brain cancer.^{222, 223} Inspired by the elegant physiology of the renal system—which has evolved the capacity to selectively filter liters of blood to remove byproducts of biological processes within minutes—we recently developed a class of protease-sensitive nanoparticles, called ‘synthetic biomarkers’, that in response to dysregulated protease activity at the sites of disease, release reporters into the circulation that are then concentrated into the host urine for noninvasive monitoring.³⁸ In murine models of liver fibrosis and cancer, we showed that synthetic urinary biomarkers have the potential to noninvasively monitor solid organs and improve early stage detection of cancer compared to tumor-secreted blood biomarkers.

Here we hypothesized that synthetic biomarkers could be tailored to survey intravascular sites for acute thrombosis, the activation of a cascade of protease activity that orchestrates the formation of obstructive blood clots within vessels (**Figure 2.1A**). Thrombi are a critical pathophysiological feature of numerous vascular diseases including acute coronary syndrome, stroke, and venous thromboembolism.²²⁴ The most important serine protease in the coagulation cascade is thrombin, which not only catalyzes the conversion of fibrinogen to fibrin that serves as the structural scaffold of a clot, but also regulates haemostasis through positive and negative feedback circuits.^{225, 226} To date, a number of studies have described the use of near-infrared fluorogenic probes to detect thrombin activity in the setting of thrombus formation as well as other thrombin-dependent diseases such as atherosclerosis.^{22, 23, 227} More recently, these probes have been modified to include cell penetrating mechanisms that are activated after cleavage to improve the retention of the imaging agent and maintenance of the detection signal.^{227, 228} In the clinic, blood biomarkers such as prothrombin fragment 1.2 (a byproduct of prothrombin cleavage

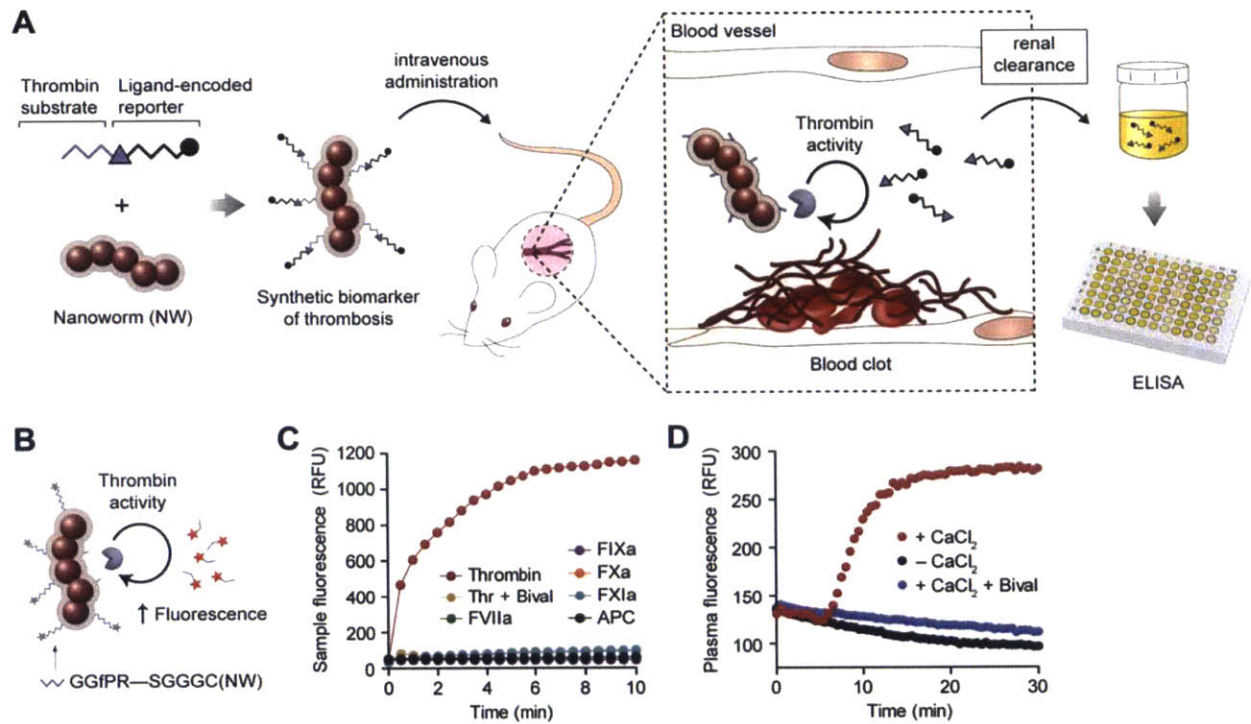


Figure 2.1. (A) Schematic of approach. Synthetic biomarkers composed of NWs conjugated with a thrombin-sensitive substrate in tandem with a ligand-encoded reporter. These agents survey the vasculature for the sites of clot formation where thrombin activity cleaves and releases the reporters into urine for analysis by ELISA. (B) Schematic of fluorogenic NW assay for detecting protease activity. (C) Kinetics of fluorogenesis produced by the activity of thrombin (red) and other coagulation proteases ($n = 3$ per condition). Thr, thrombin; Bival, bivalirudin. (D) Kinetics of fluorogenesis in plasma after the addition of CaCl_2 to activate coagulation ($n = 3$ per condition).

into thrombin) and D-dimer (a byproduct of fibrin degradation) are often used as indicators of thrombosis; however, these tests are highly susceptible to artifacts introduced by a blood draw, have poor specificity, and more accurately reflect upstream or downstream cleavage events (i.e. Factor Xa activation of prothrombin or plasmin activity during fibrinolysis, respectively) rather than thrombin activity.²²⁹⁻²³¹ In this report, we engineer nanoparticles that survey the host vasculature for thrombi and in response to thrombin activity, release reporters into the urine as an integrated measure of the aggregate burden of systemic clots.^{38, 232} We describe a method to encode these reporters with structurally distinct ligands that allow antibody-based detection by enzyme-linked immunosorbent assay (ELISA) in standardized 96-well plates that makes this platform readily amenable for use in clinical laboratories.

2.3 Results and Discussion

Engineering thrombin-sensitive synthetic biomarkers. The construction of synthetic biomarkers for thrombosis involves modifying the surface of iron oxide nanoworms (NW), a nanoparticle formulation previously developed by our collaborators,^{233, 234} with substrate-reporter tandem peptides that are cleavable by thrombin and detectable by ELISA (**Figure 2.1A**). NWs were chosen for their safety profile and large hydrodynamic diameter (~40 nm, **Figure 2.2A**), which prevents surface-conjugated peptides from filtering directly into the urine (~5 nm glomerulus size-exclusion limit) before cleavage.^{17, 28} To first develop a suitable substrate, we extended the thrombin cleavable sequence fPR-x-S (x = site of cleavage, $k_{\text{cat}}/K_m \sim 9.33 \times 10^6$)²³⁵⁻²³⁸ to include glycine spacers and a C-terminal cysteine to allow coupling to NWs via sulfhydryl chemistry.²³⁴ To test substrate specificity, we conjugated fluorophore-labeled derivatives onto NWs (sequence = (K-Fisc)GGfPRSGGGC, **Figure 2.3A**) at a valency (~40 peptides per NW by absorbance spectroscopy, **Figure 2.2B**) sufficient to reduce fluorescence by

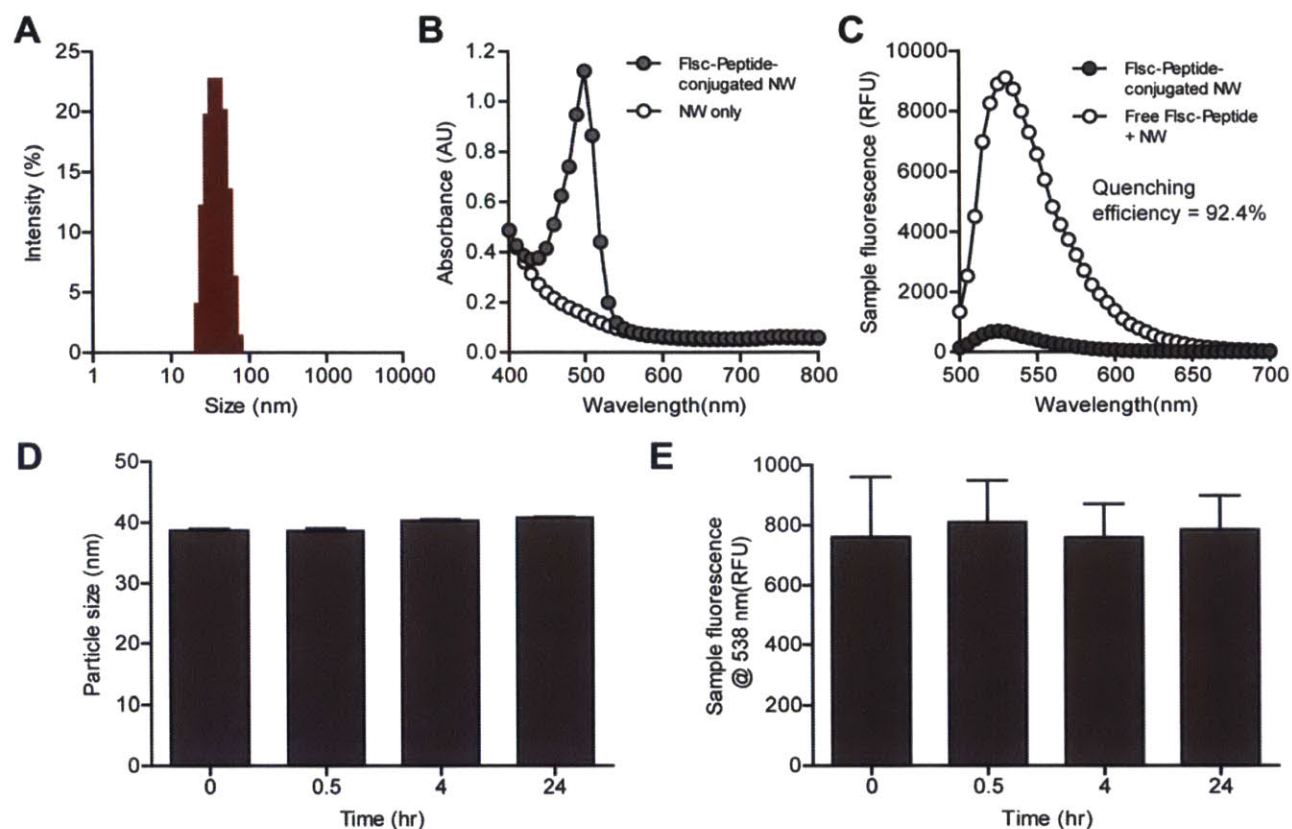


Figure 2.2. *In vitro* characterization of NWs. (A) Size distribution of iron oxide NWs as determined by dynamic light scattering. (B) Absorbance spectra of NWs conjugated with fluorescein-labeled peptides (~500 nm) and free NWs (white). (C) Fluorescence spectra of NWs conjugated with fluorescein-labeled peptides and NWs incubated with equivalent amount of free fluorescein-labeled peptides (Excitation: 470 nm; emission: 500-700 nm; cutoff: 495 nm; quenching efficiency = 92.4%). (D) Average size of NWs incubated in 10% serum at 37°C over time as determined by dynamic light scattering (n = 3 per condition, s.d.). (E) Average fluorescence of NWs incubated in 10% serum at 37°C over time (Excitation: 485 nm; emission 538 nm; cutoff: 530 nm). NWs do not appear to dequench under these conditions (n = 3 per condition, s.d.).

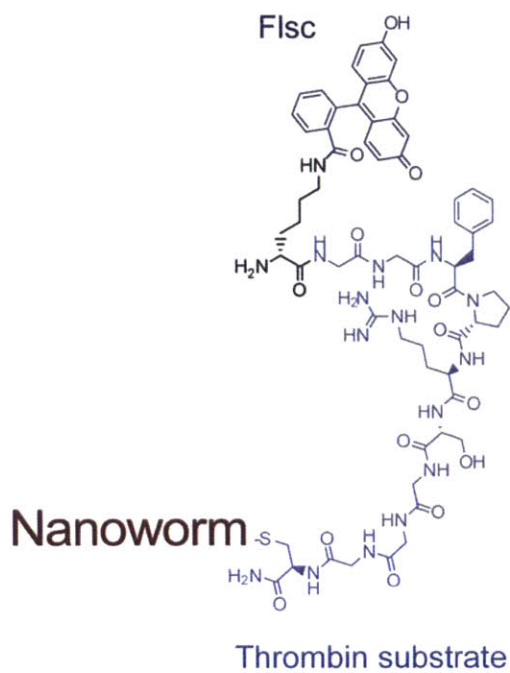
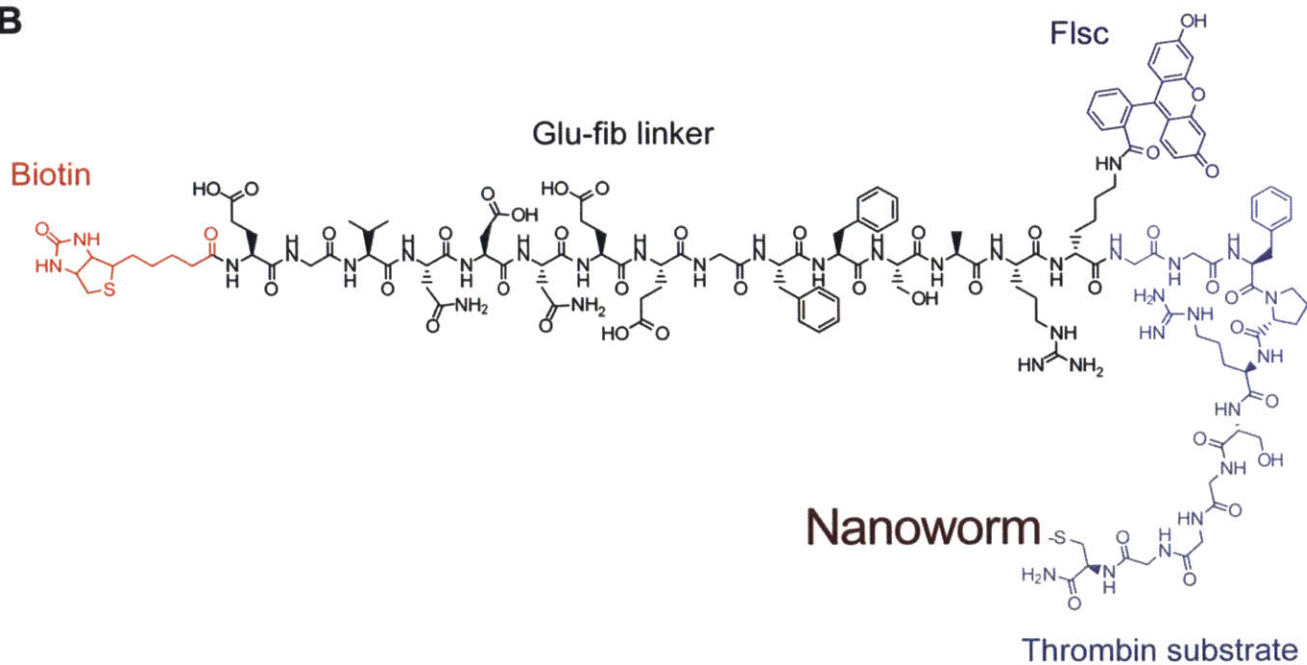
A**B**

Figure 2.3. Structures of peptide-conjugated NWs. (A) (K-Flsc)GGfPRSGGGC conjugated to NWs for *in vitro* protease assays. (B) Biotin-eGvndneeGffsar(K-Flsc)GGfPRSGGGC conjugated to NWs for urinary monitoring of thrombosis (Biotin = red, Glu-Fib = black, Flsc = purple, thrombin substrate = blue, NW = brown).

over 90% via homoquenching (**Figure 2.2C**) and then incubated the NWs (200 nM by peptide, 5 nM by NW) with purified thrombin (2 μ M) or a panel of blood clotting proteases (FXa (160 nM), APC (60 nM), FIXa (90 nM), FVIIa (10 nM), FXIa (31 nM)) each present at its maximal physiological concentration (**Figure 2.1B**). Freely emitting peptide fragments that were released by thrombin activity rapidly increased sample fluorescence (red, **Figure 2.1C**). By contrast, negligible proteolysis was observed from the panel of non-cognate proteases, as well as by thrombin in the presence of bivalirudin (Bival), a clinically-approved direct thrombin inhibitor. To further investigate the ability to sense thrombin activity from blood, we spiked NWs into human plasma samples inactivated with sodium citrate (an anticoagulant that chelates the co-factor calcium) and monitored plasma fluorescence after the addition of excess calcium chloride (CaCl_2) to trigger coagulation, or phosphate buffered saline (PBS) as a control. Aligned with our previous observations with purified enzymes, plasma fluorescence markedly increased upon activation of the clotting cascade but not in control samples or in the presence of bivalirudin (**Figure 2.1D**). To test stability, we incubated fluorogenic NWs in 10% serum at 37°C overnight and did not detect any significant differences in size (**Figure 2.2D**) that would indicate precipitation or increases in sample fluorescence (**Figure 2.2E**) that would indicate non-specific substrate cleavage. Collectively, these results established the ability of our NWs to specifically sense the proteolytic activity of thrombin within the complex milieu of plasma, consistent with previously described thrombin-specific fluorogenic probes.²³

Detection of ligand-encoded reporters by ELISA. We next set out to build a system of ligand-encoded reporters that would allow quantification of protease activity in a 96-well format by ELISA, the primary detection platform for many clinical tests. Conventional ELISAs detect a target analyte via a sandwich complex composed of two affinity agents that bind to distinct

epitopes on the analyte (**Figure 2.4A**). To build a synthetic reporter, we modified the protease-resistant peptide Glutamate-Fibrinopeptide B (Glu-fib, sequence = eGvndneeGffsar, lower case = D-isomer)—which we selected for its high renal clearance efficiency²³⁹—at the termini with structurally-distinct ligands (i.e. Flsc or AF488) and biotin (labeled R₁ and R₂ respectively; **Figure 2.4A**). To test the immunoassay, these reporters were then spiked into urine and applied to 96-well plates pre-coated with capture antibodies (α -Flsc or α -AF488) before the presence of R₁ or R₂ was detected by the addition of neutravidin-horseradish peroxidase (HRP) and its catalytic development of 3,3',5,5'-tetramethylbenzidine (TMB). As predicted from the specificities of the antibodies, a significant change in color appeared only in wells containing matched antibody-ligand pairs (+/- or -/+ wells, **Figure 2.4B**) and was not affected by the presence of non-cognate reporters (+/+ wells). Identical trends were observed at the limits of detection for both capture antibodies (~3 pM, **Figure 2.4C**, **Figure 2.5**), indicating that our synthetic reporters were detected with high specificity and sensitivity comparable with protein-based ELISAs.²⁴⁰ With an optimized thrombin substrate and a reporter system in place, we then incubated NWs decorated with our final tandem peptide construct (sequence = biotin-eGvndneeGffsar(K-Flsc)GGfPRSGGGC, **Figure 2.3B**) with increasing levels of thrombin and found that the amount of cleavage products released into solution (isolated by size filtration) was dose dependent, reaching a plateau due to cleavage of all available substrates and establishing our ability to monitor thrombin activity by ELISA (**Figure 2.4D**). Collectively, these results indicate that the specificity of ligand-antibody interactions can be used to build panels of orthogonal reporters for monitoring protease activity by standardized 96-well assays.

Characterization of thromboplastin-induced pulmonary embolism. We next investigated the ability of our synthetic biomarkers to detect thrombosis in living mice induced via

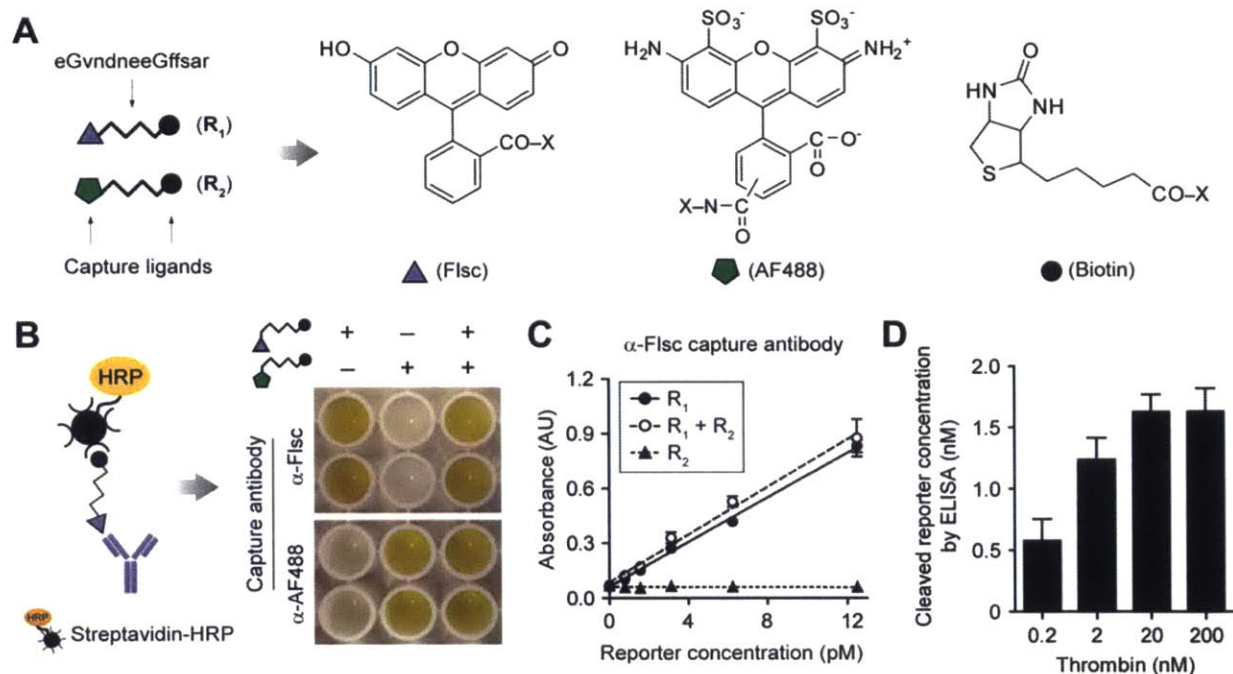


Figure 2.4. Designing ligand-encoded reporters for detection by ELISA. (A) Schematic of ligand-encoded reporters R₁ and R₂ along with chemical structures of associated ligands. (B) Schematic of ELISA sandwich complex and photograph of developed 96-well plates showing specific detection of R₁ and R₂ spiked into control urine samples. (C) Absorbance values ($\lambda = 450$ nm) of wells coated with anti-Fisc antibodies used to detect serial dilutions of R₁, R₁ + R₂, and R₂ in urine ($n = 3$ per condition, s.d.). (D) Quantification of the level of cleaved reporters (R₁) released from NWs after incubation with increasing concentrations of thrombin ($n = 3$ per dose, s.d.).

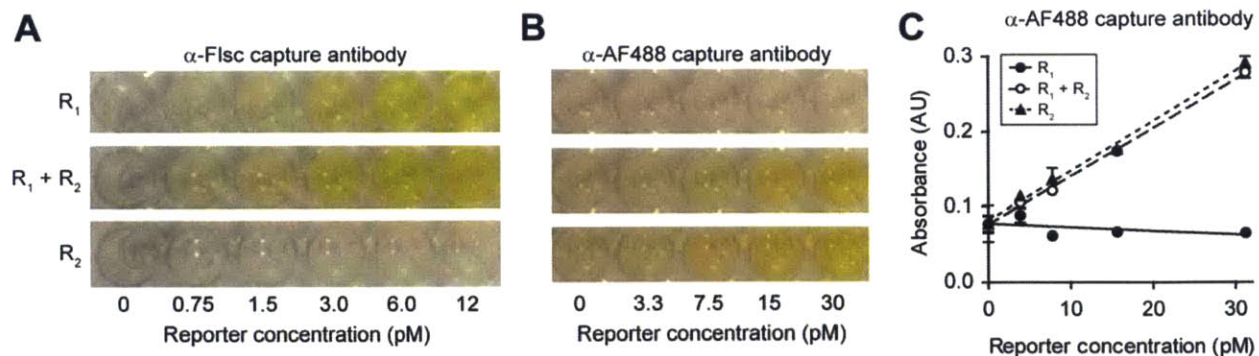


Figure 2.5. Photograph of developed 96-well plates showing serial dilutions of R₁, R₁ + R₂, and R₂ in urine detected using an (A) anti-Fisc or (B) anti-AF488 capture antibody. (C) Absorbance values ($\lambda = 450$ nm) of wells coated with anti-AF488 antibodies used to detect serial dilutions of R₁, R₁ + R₂, and R₂ in urine ($n = 3$ per condition, s.d.).

intravenous (i.v.) administration of thromboplastin. This model has been used in the hematology literature to explore the role different vascular receptors play in host susceptibility to thrombosis and to probe the efficacy of new antithrombotic agents.²⁴¹⁻²⁴³ Thromboplastin triggers the clotting cascade through the extrinsic pathway via complexation of tissue factor and factor VII, and blood clots embolize to the lungs in this model, recapitulating the life-threatening clinical condition of pulmonary embolism (PE). To quantify PE formation, we co-injected mice with thromboplastin and the clot precursor fibrinogen labeled with the near-infrared fluorophore VT750 so that the formation of fibrin clots by thrombin-mediated proteolysis of fibrinogen could be quantified by fluorescent analysis of whole organs (**Figure 2.6A**). Within 30 minutes of administration, we observed a more than 6-fold increase in the level of fibrin(ogen) deposited within the lungs and significant decreases in the kidneys and liver ($P < 0.005$ by Student's *t*-test, $n = 3$ mice; **Figure 2.6B**), consistent with venous blood flow patterns that transport thrombi formed upon i.v. administration directly to the lungs from the heart, leading to depletion of VT750-fibrinogen in the other organs. Histochemical analysis of tissue sections corroborated these findings by revealing the presence of blood clots in lung sections (blue arrow, **Figure 2.6C**) that were absent in the other major organs (brain, heart, kidney, liver and spleen; **Figure 2.7**) and in control animals. Animals given escalating but sublethal doses (observed LD50 $\sim 3 \mu\text{l}$ per g b.w.) of thromboplastin accumulated fibrin(ogen) in the lungs in proportion to the dosage, and PEs were readily prevented in animals pretreated with bivalirudin ($P < 0.005$ by one-way ANOVA with Tukey post test, $n = 3-5$ mice; **Figure 2.6D**, **Figure 2.8**), confirming that clot formation is largely driven by the activity of thrombin. Altogether, these results established our ability to precisely control total clot burden in a model that resembles the clinical pathology of venous thrombosis.^{9, 242}

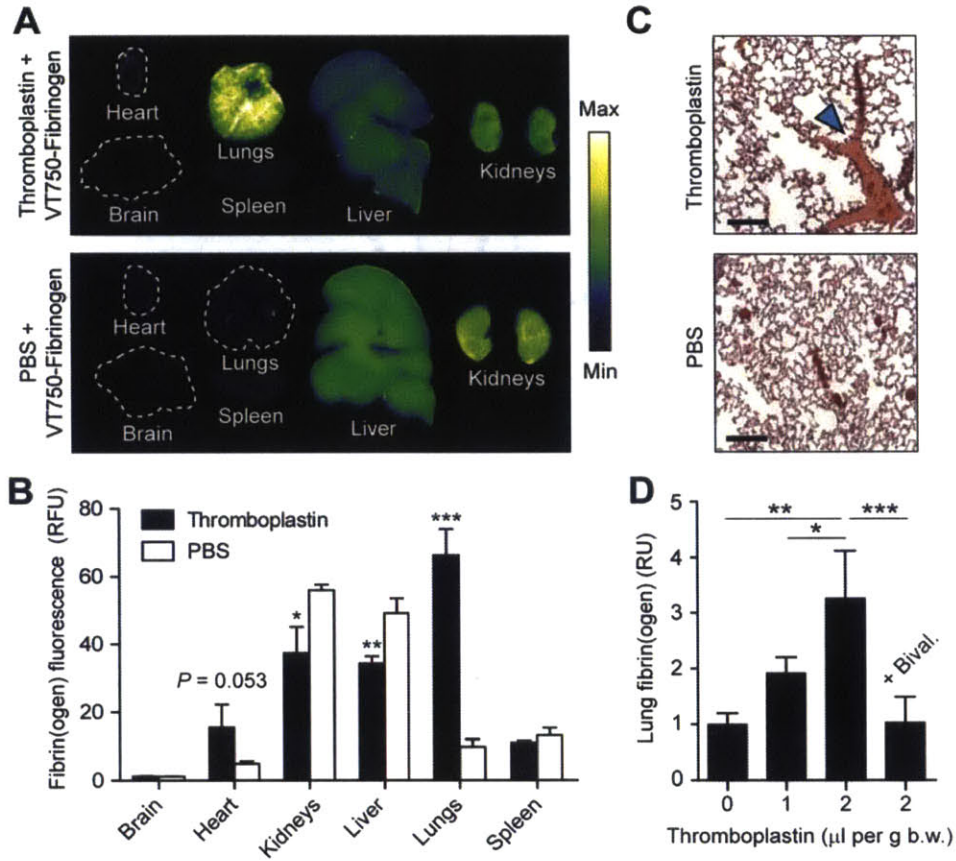


Figure 2.6. Induction of thrombosis by thromboplastin. (A) Near-infrared fluorescent scans of excised organs to monitor the deposition of VT750-labeled fibrinogen following intravenous administration of thromboplastin ($2 \mu\text{L}/\text{g}$ body weight) or PBS. (B) Quantification of the level of VT750-fibrin(ogen) deposited in organs harvested from thrombosis and control mice ($*P < 0.05$, $**P < 0.01$, $***P < 0.005$, Student's *t*-test; $n = 3$ per group, s.d.). (C) Hematoxylin and eosin staining of lungs harvested from thrombosis and healthy mice (scale bar = $100 \mu\text{m}$). Blue arrow denotes fibrin clot. (D) Quantification of fibrin deposited in the lungs in response to escalating doses of thromboplastin. Bival, bivalirudin ($*P < 0.05$, $**P < 0.01$, $***P < 0.005$, one-way ANOVA with Tukey post test; $n = 3\text{--}5$ mice, s.e.).

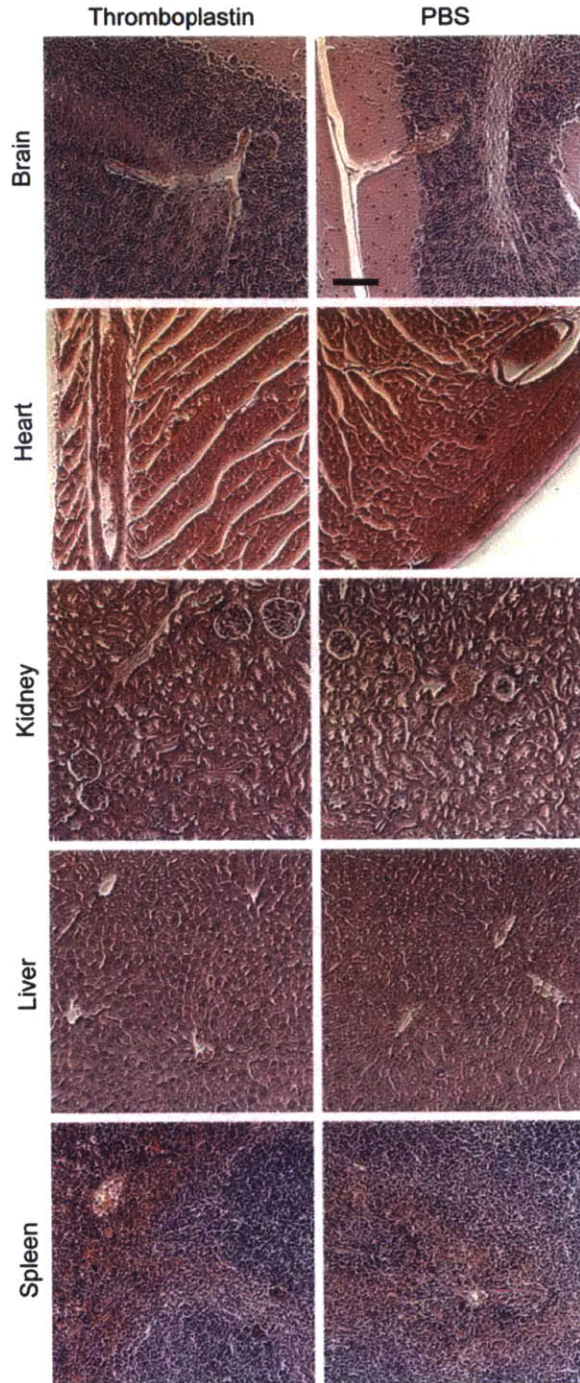


Figure 2.7. Hematoxylin and eosin staining of organ sections excised from mice following intravenous injection of thromboplastin (2 μ L/g b.w.) or PBS (scale bar = 100 μ m). No fibrin clots were observed in any of the organ sections.

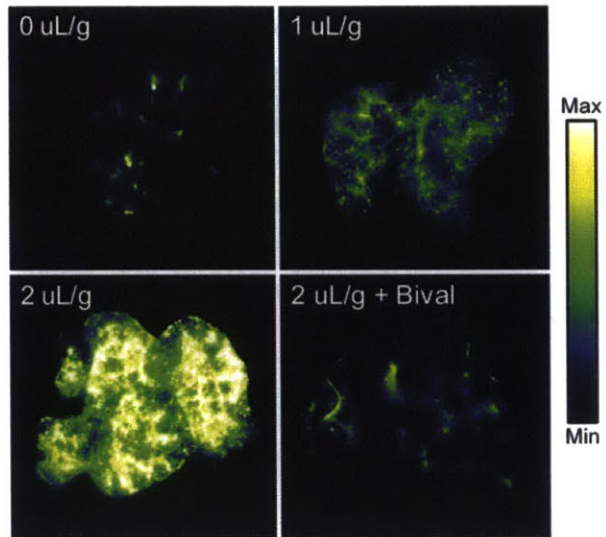


Figure 2.8. Near-infrared fluorescent scans of the level of VT750-fibrin(ogen) deposited in the lungs in response to increasing doses of thromboplastin and its inhibition by bivalirudin (Bival).

Detection of pulmonary embolism from urine. Next, we characterized the pharmacokinetics of our synthetic biomarkers in the context of thrombosis. We injected mixtures of VT750-labeled NWs and thromboplastin into mice and observed no significant differences in NW distribution between the thromboplastin and control groups in all of the excised organs—including the lungs—indicating that thrombosis did not alter the biodistribution of the NW scaffold ($P > 0.05$ by Student's *t*-test, $n = 3$ mice; **Figure 2.9A**, **Figure 2.10**). To monitor peptide cleavage and trafficking of the cleaved fragments, we co-administered NWs conjugated with fluorescently-quenched substrates and observed significant increases in fluorescence in the lungs and kidneys by ~ 1.8 and ~ 2.5 fold over healthy animals respectively ($P < 0.01$ by Student's *t*-test, $n = 3$ mice; **Figure 2.9B**, **Figure 2.11**). Paired with our earlier observations showing that thromboplastin did not alter the biodistribution of the NWs and induced blood clots that were localized to the lung (i.e. clots were not found in the kidneys), this finding provided evidence of peptide cleavage in the lungs and kidney accumulation of freely-emitting fluorescent fragments. Immunofluorescent staining of lung sections further showed NW (green) localization with fibrin (red) at the sites of coagulation, that was absent in control sections (**Figure 2.12**), supporting our hypothesis that circulating NWs can access local thrombi. To visualize the clearance efficiencies of the peptide fragments, we monitored mice by *in vivo* fluorescence imaging and observed a strong increase in fluorescent signal that was localized to the bladder of thrombotic mice relative to controls (**Figure 2.9C**). Taken together, our data illustrated that our synthetic biomarkers can systemically survey the vasculature for thrombin activity and release reporters at sites of thrombosis which are then cleared efficiently into the host urine.

In considering clinical translation, we sought to develop a method to account for variations in the production rate of urine expected in individuals that could affect the urine

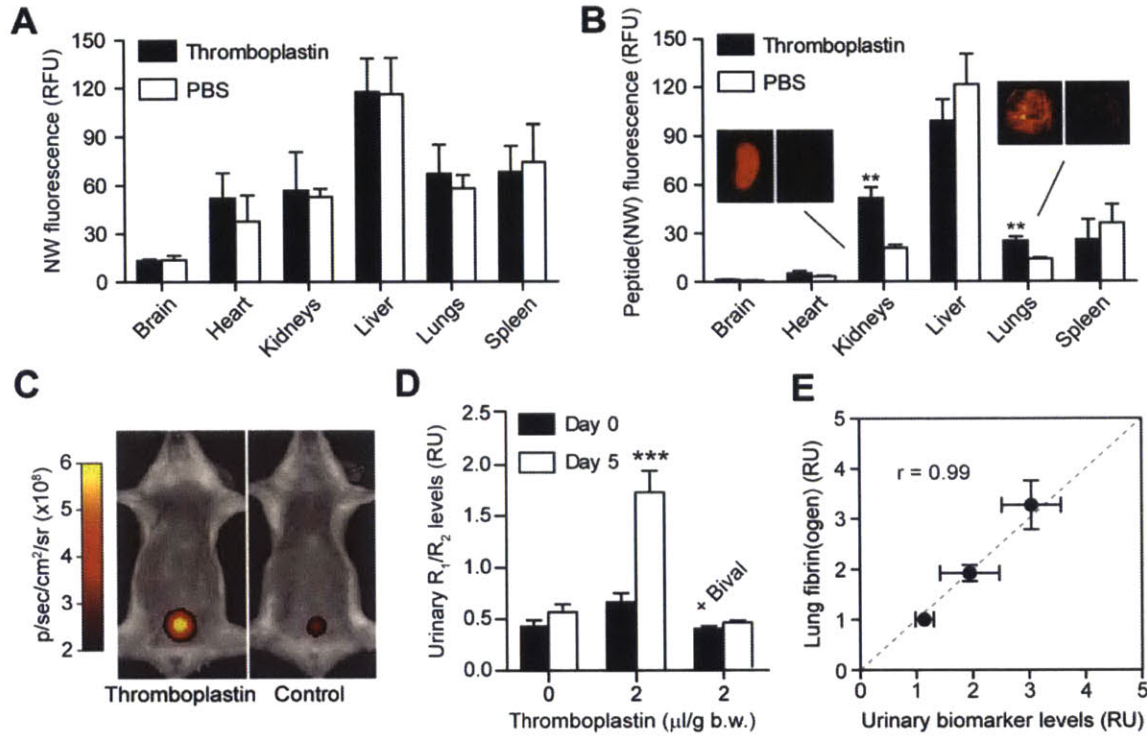


Figure 2.9. Noninvasive urinary detection of pulmonary embolism. (A) Quantification of the distribution of VT750-labeled NWs in organs excised from mice treated with thromboplastin or PBS ($n = 3$ mice, s.d.). (B) Quantification of the fluorescent signal of organs after mice were infused mixtures of NWs conjugated with quenched substrates (labeled with VT750) and thromboplastin or PBS (** $P < 0.01$, Student's t -test; $n = 3$ mice, s.d.). Inset shows representative fluorescent scans of the kidneys and the lungs. (C) *In vivo* fluorescent image after administration of NWs showing increased fluorescent signal localized to the bladders of mice challenged with thromboplastin. (D) Normalized urinary reporter levels (R_1/R_2) from healthy mice (Day 0) and in response to thromboplastin and bivalirudin (Day 5). Bival, bivalirudin (** $P < 0.005$, two-way ANOVA with Bonferroni post test; $n = 5$ mice, s.e.). (E) Correlation plot of the clot burden in the lungs versus urinary biomarker levels (Pearson's $r = 0.999$; $n = 5-10$ mice, s.e.).

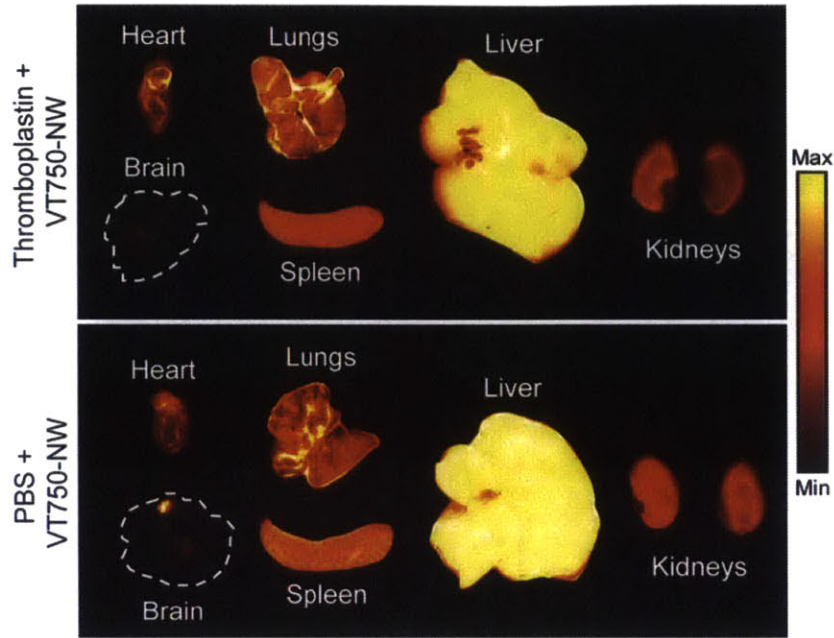


Figure 2.10. Near-infrared fluorescent scans of excised organs to assess VT750-NW distribution following intravenous injection of thromboplastin (2 $\mu\text{L/g}$ b.w.) or PBS.

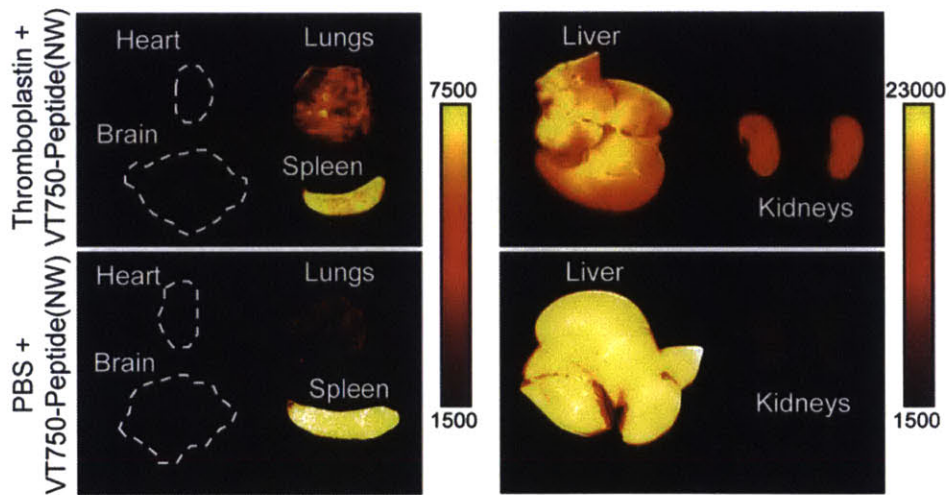


Figure 2.11. Near-infrared fluorescent scans of excised organs to monitor substrate-NW cleavage in response to thromboplastin (2 $\mu\text{L/g}$ b.w.) or PBS.

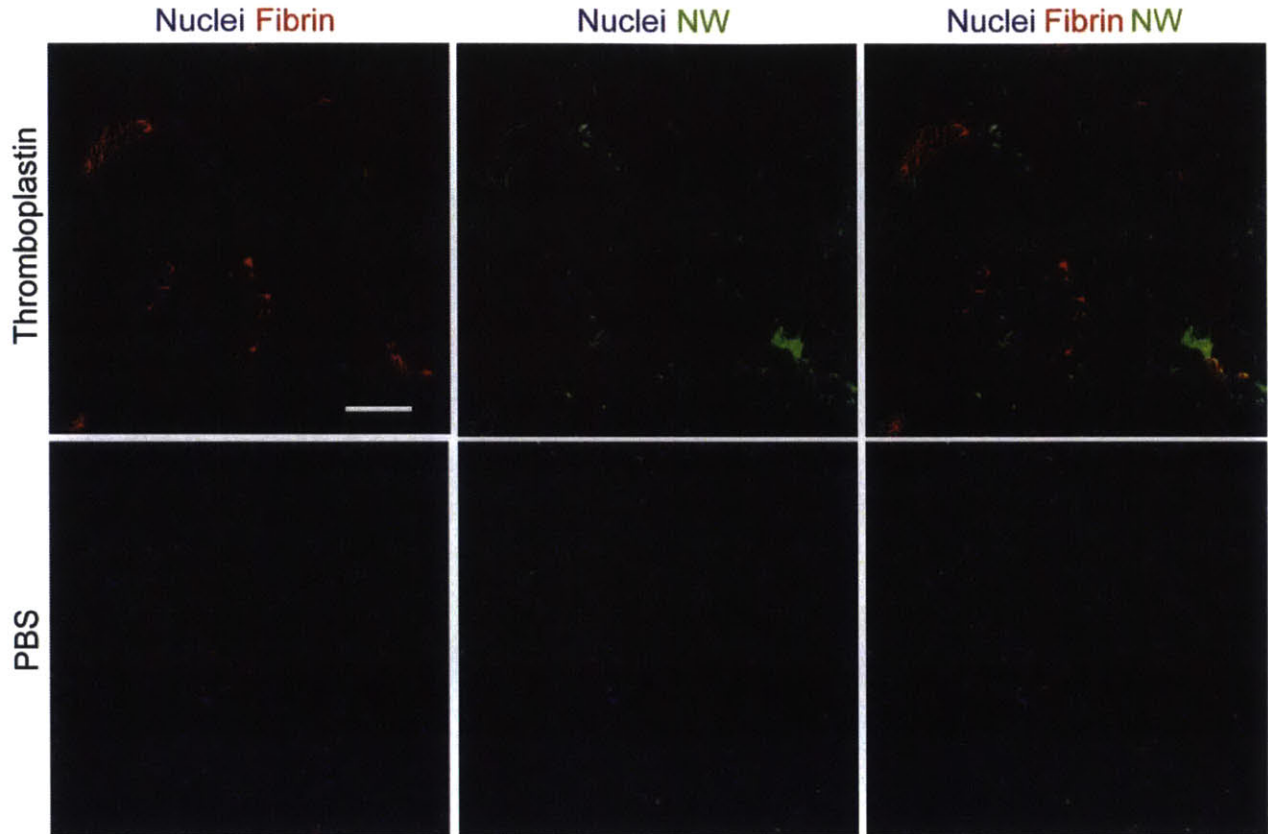


Figure 2.12. Immunofluorescent staining of lung sections following intravenous injection of thromboplastin or PBS. Staining of fibrin clots (red), NWs (green), and nuclei (blue) in the lung (scale bar = 100 μm).

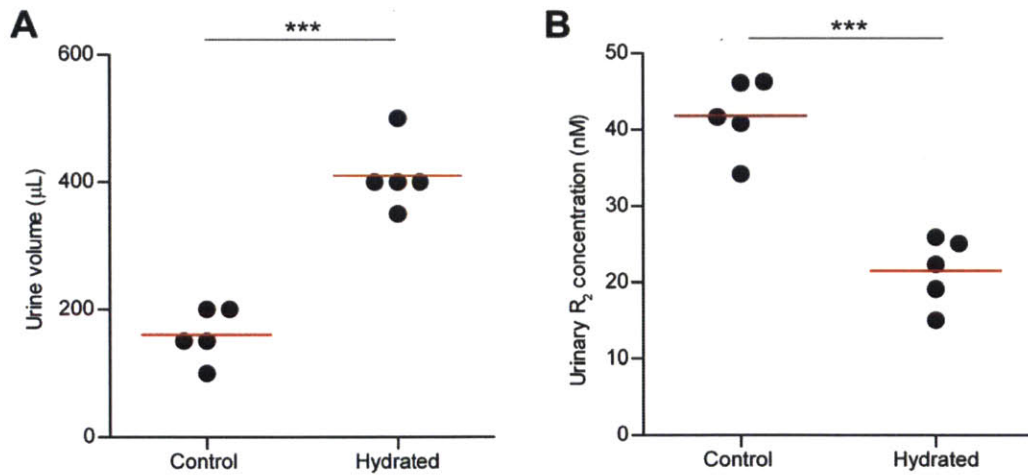


Figure 2.13. Monitoring urine concentration by administering R_2 intravenously in mice. (A) Urine volume collected from control mice *versus* mice hydrated with 10% body weight equivalent of PBS injected subcutaneously, two hours after administration ($***P < 0.005$, Student's t -test; $n = 5$ mice.). (B) Quantification of R_2 in urine collected from control *versus* hydrated mice *via* ELISA ($***P < 0.005$, Student's t -test; $n = 5$ mice.).

concentration of our reporters. Urinary production rates are mainly dependent on the hydration state of the host (ranging from 50–1200 mOsm/kg H₂O in humans)²⁴⁴ and affected by many external factors (e.g. circadian rhythm, diet, activity, and others). Approaches to determine the concentration of urine include measuring the level of creatinine,^{245, 246} a byproduct of muscle metabolism that filters into the urine at a steady state when at rest, or i.v. administration of inulin,²⁴⁷⁻²⁴⁹ a polysaccharide that is not actively absorbed or secreted by the kidneys and whose appearance in urine is directly related to the rate of urine production. Motivated by the clinical precedent set by inulin, we hypothesized that because our free reporters (R₁, R₂) are built from Glu-fib which is likewise biologically inert,²³⁹ their filtration into urine following i.v. administration would be indicative of the concentration of urine. To test this, we excessively hydrated a cohort of mice with a subcutaneous bolus of saline equivalent to 10% of their body weight followed by i.v. administration of free R₂. Compared to control mice infused with R₂ only, hydrated mice produced over 2.5 fold more urine within 2 hours ($P < 0.005$ by Student's *t*-test, **Figure 2.13A**) and their urinary concentration of R₂ decreased by ~50% ($P < 0.005$ by Student's *t*-test, **Figure 2.13B**), showing that our free reporters could be used to monitor the hydration state and urine concentration of the animals. We next sought to monitor thromboplastin-induced PEs by urine analysis of the response of our synthetic biomarkers to thrombin activity. To simulate serial monitoring that frequently occurs in inpatient settings, we first determined the basal activity in healthy cohorts of animals each receiving thrombin-sensitive NWs and a free reporter (R₂) for urine normalization (**Figure 2.9D**). After five days to allow NWs to fully clear (half-life ~6 hours),³⁸ we administered a mixture of thromboplastin, NWs, and R₂ into the same mice and quantified reporter levels by ELISA. When compared to their healthy state (Day 0), the induction of PEs (Day 5) resulted in significant elevations in the

level of urinary cleavage fragments by up to three fold ($P < 0.005$ by two-way ANOVA with Bonferroni post test, $n = 5$ mice; **Figure 2.9D**). In mice treated with bivalirudin prior to thrombotic challenge (dose = 2 μl per g b.w.), reporter levels were abrogated, consistent with our earlier findings showing the ability of bivalirudin to inhibit thrombin activity and prevent the formation of PEs. When the urinary biomarker marker levels from thromboplastin-challenged mice were directly compared to the amount of fibrin(ogen) deposited at identical doses of thromboplastin (**Figure 2.6D**), we found a striking correlation to the disease burden with a correlation coefficient of 0.99 (Pearson's r , **Figure 2.9E**). Collectively, our findings showed that synthetic biomarkers can monitor thrombin activity in living mice and quantitatively measure the aggregate burden of sublethal PEs from the urine by ELISA.

2.4 Conclusion

By harnessing the capacity of peptide-decorated NWs to circulate and sense their local vascular microenvironment, we have engineered synthetic biomarkers that can detect thrombin activity *in vivo* and noninvasively quantify the aggregate amount of active clots. Unlike other nanoparticle sensors that function by producing a localized signal,^{22, 23, 227, 228, 250-252} our NWs sense protease activity by releasing reporters locally at the sites of thrombus formation but are then filtered and detected remotely from the urine. Interestingly, in imaging studies using fluorogenic thrombin-cleavable probes, this 'washout' of the cleaved fragments was also directly observed by monitoring the attenuation of the strength of the detection signal localized at the thrombi.²² Similar to circulating biomarkers, our approach can reveal thrombosis at sites deep within the body, such as the lungs, that are difficult to detect with fluorogenic probes due to tissue absorption and scattering of light.²⁵³ This property allows urine analysis to integrate and quantitatively assess the burden of vascular clots, which would otherwise require systemic

exploration by imaging. In addition, we developed a panel of heterobifunctional reporters that can be detected by standardized 96-well plate assays, removing the need for mass spectrometry as described in our previous study.³⁸ This reporter system is readily extensible by incorporating additional ligand-capture agent pairs and is amenable for detection by other methods including paper-based tests at the point of care.²⁵⁴⁻²⁵⁶ Potential improvements to this platform include the use of new thrombin-sensitive substrates that are significantly more specific to reduce background activities from other plasma proteases,^{238, 257} and further functionalizing NWs, which are super-paramagnetic,²³⁴ with fibrin-targeted ligands to allow contrast-enhanced magnetic resonance imaging (MRI) of individual clots simultaneously with urine analysis.^{27, 37, 172} To allow clinical translation, we chose to use NWs because we previously showed that they are well-tolerated by mice and similar FDA-approved formulations of iron oxide nanoparticles (e.g. Ferridex ®) are already used in patients,^{38, 258-263} however, thrombin substrates may also be attached to other long-circulating nanoparticles, such as dextran or liposomes, to prevent peptide filtration into urine until cleavage by proteases.

Looking forward, several clinical applications warrant further investigation with this approach. Because sensing thrombin activity requires NWs to access the sites of coagulation, the local architecture of the vessels, clotting kinetics of the thrombi and degree of occlusion would all likely influence the rate of peptide cleavage and clearance efficiencies of the reporters.^{22, 227, 228} Therefore, additional studies that utilize specific clinical models, such as deep vein thrombosis (DVT), would be important to determine the type of clots this approach could be used to detect. Further, whereas MRI or ultrasound can resolve anatomical features of clots, they cannot discriminate stable from extending thrombi without serial imaging. Related studies in atherosclerosis showed that thrombin activity could be used to differentiate stable from severe

plaques, highlighting the potential benefits of an activity-based measurement compared to imaging alone.²²⁷ In summary, we believe this work further broadens the repertoire of nanomedicines that could be used for noninvasive monitoring of disease, and we anticipate generalization to additional clinical settings in which dysregulated thrombin activity is prominent.

2.5 Materials and Methods

Peptide nanoworm synthesis. Aminated iron oxide NWs were synthesized according to previously published protocols.²³⁴ Peptides (biotin-eGvndneeGffsar(K-Flsc)GGfPRSGGGC, lower case = D-isomer) were synthesized by the Tufts University Core Facility peptide synthesis service. To conjugate peptides to NWs, NWs were first reacted with succinimidyl iodoacetate (Pierce) to introduce sulfhydryl-reactive handles. Cysteine terminated peptides and 20 kDa polyethylene glycol-SH (Laysan Bio.) were then mixed with NWs (95:20:1 molar ratio) for one hour at room temperature (RT) and purified by fast protein liquid chromatography. Stock solutions were stored in PBS at 4°C. The number of fluorescein-labeled peptides per NWs was determined by absorbance spectroscopy using the absorbance of fluorescein (490 nm) and its extinction coefficient ($78,000 \text{ cm}^{-1}\text{M}^{-1}$). For pharmacokinetic studies, NWs were first reacted with NHS-VT750 (PerkinElmer) prior to PEGylation as above. For fluorogenic assays, thrombin substrates were synthesized with a terminal fluorescein or VT750 in lieu of a reporter.

In vitro stability assays. NWs (1 μM by peptide, 25 nM by NW) were incubated in 10% fetal bovine serum at 37°C. At selected timepoints, the particle size was measured by dynamic light scattering (Malverin Zetasizer Nano Series) and the fluorescence intensity was measured by microplate reader (SpectroMax Gemini EM).

In vitro protease assays. NWs (200 nM by peptide, 5 nM by NW) were mixed with human thrombin (2 μM), FVIIa (10 nM), FIXa (90 nM), FXa (160 nM), FXIa (31 nM), and activated protein C (60 nM) all purchased from Haematologic Technologies in a 384-well plate at 37°C in activity buffers according to the manufacturer's instructions and monitored with a microplate

reader (SpectroMax Gemini EM). For plasma studies, NWs were mixed with 50 μ L of control human plasma (Thermo Scientific) and 50 μ L of 80 mM CaCl₂ (Sigma) or PBS. For thrombin inhibition experiments, bivalirudin (Anaspec) was added to a final concentration of 5 mg/mL and pre-incubated for two minutes prior to addition of NWs. For the ELISA studies, NWs (100 nM by peptide, 2.5 nM by NW) were incubated with thrombin for 10 min. at 37°C and cleaved reporters (R₁) were purified from NWs by centrifugal size filtration (3 kDa MWCO).

ELISA detection of bifunctionalized reporters. The bottom of 96-well plates (Thermo Scientific) were coated with either 0.8 μ g/mL of anti-FIsc (GeneTex, GTX19224) or 0.4 μ g/mL of anti-Alex Fluor 488 (Invitrogen, A11094) diluted in PBS overnight at 4°C. Plates were blocked with 1% w/v bovine serum albumin (Sigma) in PBS for 1 hr before 100 μ L of samples were added. Reporters captured on the plate were then detected by adding 100 μ L of 0.2 μ g/mL neutravidin-HRP (Pierce), developed with 50 μ L TMB solution (Thermo Scientific) for 5–15 minutes and quenched with 50 μ L of HCl before the absorbance of the wells was determined by microplate analysis (SpectraMax Plus, Molecular Devices) at 450 nm. Plates were washed 3x with PBST between each steps and incubation occurred at RT unless otherwise stated.

Characterization of thromboplastin-induced thrombosis. Each vial of thromboplastin containing 3–4 mg (from rabbit brain, Sigma) was dissolved in 2 mL of PBS. To quantify fibrin deposition, bovine fibrinogen (Sigma) was reacted with 3-fold molar excess of VT750 for 1 hr at RT, and purified by centrifugal size filtration (100 kDa MWCO, Millipore). Swiss Webster mice (Taconic) were lightly anesthetized with isoflurane and administered mixtures of VT750-fibrinogen (1 nmol by VT750) with thromboplastin (n = 3 mice per dose) via tail vein injections. After 30 minutes, mice were euthanized by CO₂ asphyxiation and organs were scanned on the

LI-COR Odyssey Infrared Imaging System. Fluorescence in each organ was quantified using ImageJ software (NIH). To test thrombin inhibition, mice were intravenously administered bivalirudin (10 mg/kg) five minutes prior to co-injection of thromboplastin. For histology, lungs were inflated with 4% paraformaldehyde while all other organs were incubated in 4% paraformaldehyde for 1-2 hours at RT. All organs were stored in 70% ethanol until paraffin-embedding, sectioning, and staining (Koch Institute Histology Core).

NW pharmacokinetics. To analyze NW and peptide pharmacokinetics, mice were given either VT750-labeled NWs (5 μ M by VT750) or NWs conjugated with VT750-labeled peptides (600 nM by peptide) in conjunction with thromboplastin. To analyze tissue sections by immunostaining, NWs (600 nM by peptide, 15 nM by NW) and thromboplastin (2 μ L/g b.w.) were administered to mice and major organs were harvested after 30 minutes. Representative lung sections were stained for NWs (anti-Flsc primary, Invitrogen, A11090), fibrin (Nordic, GAM/Fbg/Bio) and Hoechst (Invitrogen, H3569) before analysis by fluorescence microscopy (Nikon Eclipse Ti).

Effect of hydration state on urine concentration. The free reporter R₂ (biotin-eGvndneeGffsar(K-AF488)) was synthesized by the Tufts University Core Facility peptide synthesis service. Mice (n = 5 mice) were anesthetized and injected subcutaneously with a PBS bolus equivalent to 10% of their body weights. After two hours, R₂ (125 nm) was administered to mice via a tail vein injection. Mice were placed over 96-well plates surrounded by cylindrical sleeves for 30 minutes post-NW injection to allow mice to void. Urine samples were stored at -80°C until ELISA analysis.

Urinary monitoring of thrombosis. Experiments were conducted in a paired setup. Thrombin-sensitive NWs (600 nM by peptide, 15 nM by NW) and R₂ (125 nM) were co-injected into healthy mice (n=5–10 mice) to determine background protease activity and placed over 96-well plates to collect urine. Five days later, mice were again dosed with NWs, R₂ and thromboplastin before urine was collected from mice 30 minutes post-NW injection. For thrombin inhibition experiments, mice were intravenously administered bivalirudin (10 mg/kg) five minutes prior to NW/R₂ injections. Urine samples were stored at -80°C until ELISA analysis.

Statistical analyses. ANOVA analyses and Student's *t*-test were calculated with GraphPad 5.0 (Prism). Pearson's *r* coefficient was calculated with Excel (Microsoft Office).

All animal work was approved by the committee on animal care (MIT, protocol #0411-036-14).

2.6 Acknowledgements

Dr. Gabriel Kwong, Andrew Warren, and Dr. David Wood were co-authors on this work. We thank the Swanson Biotechnology Center (MIT) for use of their animal imaging facilities and assistance with tissue sectioning. This work is supported by a grant from the Koch Institute Frontier Research Program through the Koch Institute Frontier Research Fund and the Kathy and Curt Marble Cancer Research Fund, the Mazumdar-Shaw International Oncology Fellows Program, and the MIT Deshpande Center Innovation Grant. K.Y.L. acknowledges support from CCNE (5 U54 CA151884-03). Dr. G.A.K. acknowledges support from the Ruth L. Kirschstein National Research Service Award (F32CA159496-02) and holds a Career Award at the Scientific

Interface from the Burroughs Wellcome Fund. Dr. S.N.B is an HHMI Investigator. The authors wish to dedicate this paper to the memory of Officer Sean Collier, for his caring service to the MIT community and for his sacrifice.

Chapter 3: Self-Titrating Anticoagulant Nanocomplexes that Restore Homeostatic Regulation of the Coagulation Cascade

3.1 Abstract

Antithrombotic therapy is a critical portion of the treatment regime for a number of life-threatening conditions, including cardiovascular disease, stroke, and cancer; yet proper clinical management of anticoagulation remains a challenge because these agents increase the propensity for bleeding in patients. Here, we describe the development of a bioresponsive peptide-polysaccharide nanocomplex that utilizes a negative feedback mechanism to self-titrate the release of anticoagulant only in response to pathological levels of coagulation activity. This nanoscale self-titrating activatable therapeutic, or nanoSTAT, consists of a cationic thrombin-cleavable peptide and heparin, an anionic polysaccharide and widely used clinical anticoagulant. Under non-thrombotic conditions, nanoSTATs circulate inactive, neither releasing anticoagulant nor significantly prolonging bleeding time. However, in response to life-threatening pulmonary embolism, nanoSTATs locally release their drug payload and prevent the formation of thrombosis. This autonomous negative feedback regulator may improve antithrombotic therapy by increasing the therapeutic window and decreasing the bleeding risk of anticoagulants.

3.2 Introduction

Homeostatic regulation plays a critical role in human health and underlies diverse biological processes, including hormone release,²⁶⁴ ionic balance,^{265, 266} and cell-mediated immunity.^{267, 268} In particular, living systems employ negative feedback circuits to maintain processes within physiologic limits, preventing unrestricted amplification cascades or positive

feedback cycles.²⁶⁹⁻²⁷¹ A key homeostatically regulated process with significant medical relevance is blood coagulation, the protease-driven positive-feedback cascade by which clots are formed to stop blood loss from injured vessels. Dysregulation of this process, whether pathological or drug-induced, leads to adverse outcomes: insufficient coagulation promotes life-threatening hemorrhage, while uncontrolled coagulation drives thrombosis – or intravascular clotting – the potentially fatal medical condition underlying pulmonary embolism, stroke, and organ infarction.⁹ Clinical prevention of thrombosis revolves around the administration of anticoagulants, the levels of which must be tightly controlled within a narrow therapeutic window to prevent coagulation and limit life-threatening bleeds that are their primary side effect.²⁷² Consequently, anticoagulants require strict dose titration and monitoring,^{273, 274} and there remains a pressing need for safe, yet effective agents to improve the treatment of thrombosis.

The advent of nanotechnology has enabled a plethora of engineering approaches for improving the efficacy and safety profiles of drugs.^{1, 3} A number of these nanoscale drug delivery schemes have drawn inspiration from the ability of biological systems in nature to coordinate multiple molecular components to produce emergent behaviors in order to design nanosystems that communicate across multiple length scales, form positive feedback loops, and drive accumulation of drugs at disease sites.^{172, 182, 275} Here, inspired by the human body's capacity to precisely orchestrate and control biological reaction networks, we sought to engineer nanoagents that could autonomously regulate coagulation by self-titrating the release of a systemically administered anticoagulant, thereby improving its safety profile. Existing delivery strategies for anticoagulants have explored the use of biodegradable polymers for controlled release,²⁷⁶⁻²⁷⁸ multivalent presentation to increase potency,^{83, 85} or reformulated drugs to enable

alternative routes of administration.⁷⁷ While anticoagulants have previously been packaged in nanoparticle form, these open-loop systems deliver their cargo without any form of feedback regulation and cannot autonomously titrate the release of drugs in response to dynamic circulatory conditions within the body.

In this study, we reformulate unfractionated heparin (UFH), the prototypical clinical anticoagulant,³⁹ into a self-assembled nanocomplex that is responsive to thrombin, a key protease of the coagulation cascade, by leveraging the charge interaction of cationic peptides composed of thrombin-cleavable substrates with the naturally anionic heparin (**Figure 3.1A**). The resultant complexes release heparin in response to thrombin activity, which then interacts with endogenous antithrombin (ATIII) to inhibit thrombin, the initial trigger of drug release, thereby creating a negative feedback control circuit (**Figure 3.1B**). This thrombin-activated release mechanism deploys more anticoagulant during thrombosis, when the generation of thrombin outpaces endogenous regulatory checkpoints, compared to healthy coagulation that is normally tightly regulated. We explore the composition of pegylated nanocomplexes and characterize their *in vitro* and *in vivo* release of heparin, efficacy in a pulmonary embolism model of thrombosis, and impact on systemic bleeding time. This nanoscale self-titrating activatable therapeutic (nanoSTAT) has the potential to prevent thrombosis with fewer bleeding side effects than its free counterpart.

3.3 Results

Synthesis and characterization of nanoSTATs. Unfractionated heparin is a mainstay drug used in the hospital setting, yet it is particularly difficult to dose due to its unpredictable pharmacokinetics, thus its use requires clotting time measurements and dose re-adjustment every 3–4 hours to maintain drug levels within the therapeutic range.^{41, 279, 280} Because it is highly

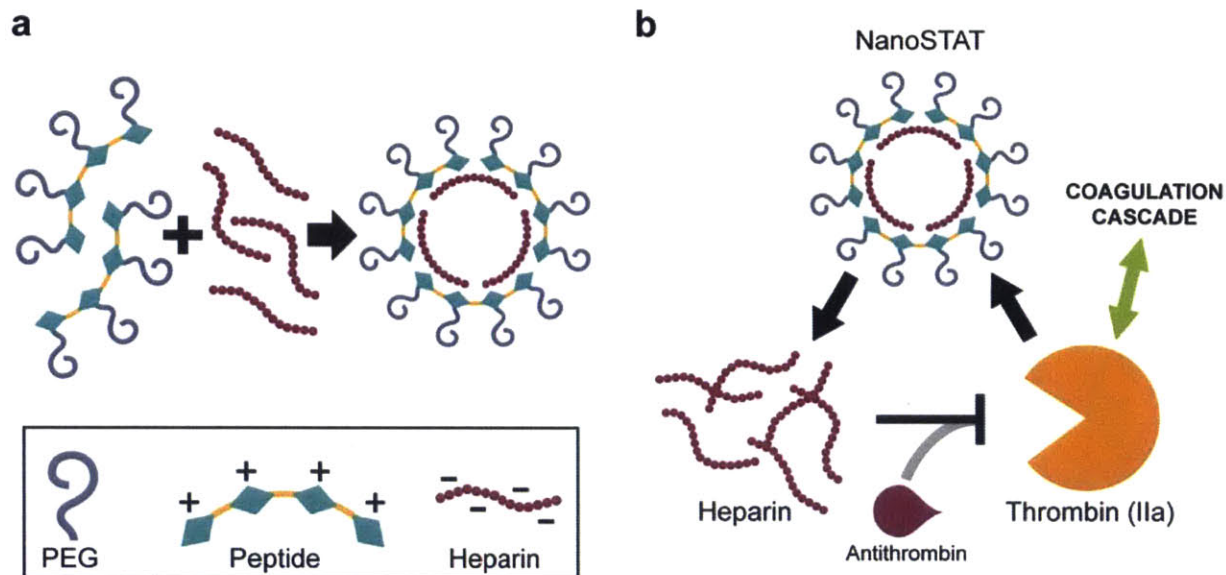


Figure 3.1. Schematic of self-titrating activatable therapeutic. (A) Self-assembly of cationic PEG-Peptide and anionic heparin to form nanoSTATs. (B) Negative feedback system for self-titrating release of heparin in response to thrombin activity.

anionic, heparin is readily sequestered by cationic peptides,²⁸¹ such as its clinical antidote protamine, which is characterized by a very high net positive charge.²⁸² Therefore, we designed a cationic peptide sequence with multiple arginine/lysine-rich regions separated by thrombin-cleavable substrates (LVPR.RK4 sequence = rkrk-(LVPRG-rkrk)₃, lower case = D-isomer) that is capable of inhibiting heparin activity while intact, yet releases active heparin following degradation by thrombin.²⁸³ To further stabilize the nanocomplexes in ionic solutions, prevent non-specific protein interactions, prolong circulation time, and improve biodistribution, we conjugated the FDA-approved polymer, poly(ethylene glycol) (PEG, 5 kDa), to a subset of the lysine residues using amine-reactive ester chemistry.^{4, 284} When the heparin (~18 kDa) and PEG-LVPR.RK4 conjugate were mixed together, they self-assembled into spherical nanoscale complexes, or nanoSTATS, as confirmed by transmission electron microscopy (**Figure 3.2A**).

To explore the impact of component ratios on complex formation, we varied PEG:LVPR.RK4 reaction ratios between 0:1 to 5:1 (mol/mol) and LVPR.RK4:heparin mixing ratios between 5:1 to 10:1 (mol/mol) and measured the resultant nanoSTAT particle size and zeta potential in phosphate-buffered saline (PBS) or 10% exosome-free fetal bovine serum *via* dynamic light scattering (DLS). In both solutions, increasing the LVPR.RK4:heparin mixing ratio from 5:1 to 10:1 caused the nanoSTAT hydrodynamic diameter to aggregate in size from the nano- (~150 nm) to the micro-scale (~2-3 microns), while increasing the PEG:LVPR.RK4 reaction ratio decreased the complex size (**Figure 3.2B**). The zeta potential of nanoSTATs was generally negative, particularly in 10% serum, with the addition of PEG bringing the charge closer to neutrality (**Figure 3.2C**). A component ratio of 25:5:1 PEG:LVPR.RK4:heparin generated the smallest particles (hydrodynamic diameter ~70 nm) and was used for the remainder of *in vitro* and *in vivo* experimentation. Finally, since some charged nanomaterials are

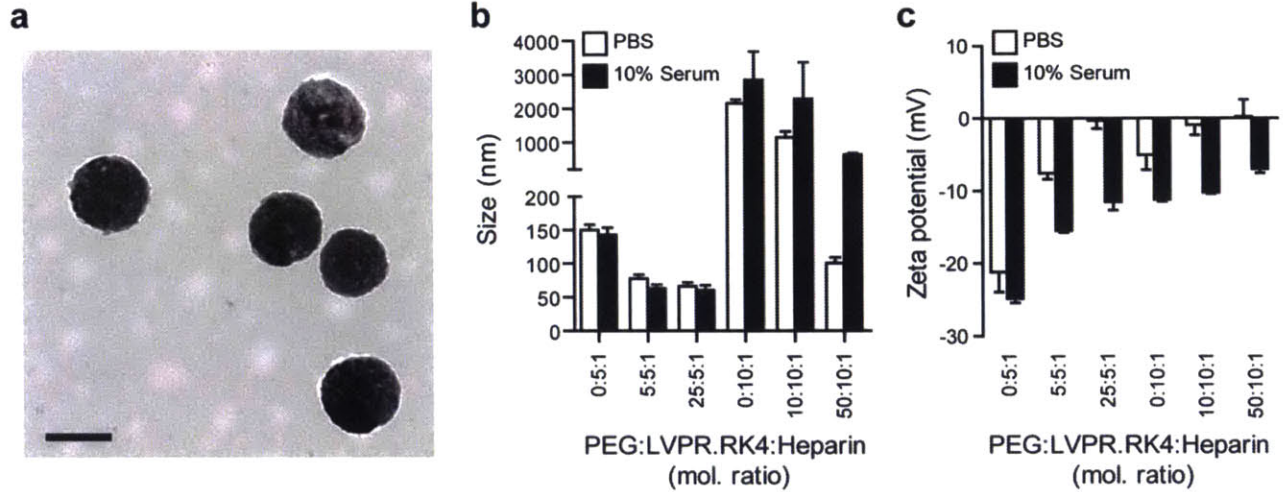


Figure 3.2. *In vitro* characterization of nanoSTATs. (A) Transmission electron microscopy image of nanoSTATs (scale bar = 100 nm). (B) Mean hydrodynamic diameter of nanoSTATs at varying PEG:LVPR.RK4:Heparin ratios in PBS and 10% serum ($n = 3$ per condition, s.d.). (C) Zeta potential of nanoSTATs at varying PEG:LVPR.RK4:Heparin ratios in PBS and 10% serum ($n = 3$ per condition, s.d.).

known to produce cytotoxic profiles,^{285, 286} we incubated human endothelial cells (HUVECs) with nanoSTATs at representative therapeutic heparin concentrations and established that no toxicity was observed up to 10 U/mL, which corresponds to a ~1000 U/kg heparin dose in the bloodstream, or an order of magnitude higher than standard dosing regimens (**Figure 3.3**).²⁸⁷

Veiling and unveiling of nanoSTATs in vitro. Next, we assayed whether nanoSTATs could regulate the release of heparin in response to clotting activity. We exploited the serine protease thrombin as the drug release trigger on the basis of its critical role in catalyzing the formation of fibrin clots, regulating haemostasis through positive and negative feedback circuits, and sensitivity to inhibition by heparin.²²⁵ To characterize thrombin-triggered disassembly, we incubated nanoSTATs with or without thrombin (500 nM) at 37°C and assayed the samples by analytical FPLC. The control sample chromatogram exhibited a sharp peak at ~7mL corresponding to intact nanoSTATs, which was absent in the presence of thrombin and instead replaced by a broad peak from ~11–17mL, corresponding to the profile of free heparin (**Figure 3.4**). To determine the accessibility of heparin when complexed, we mixed nanoSTATs with Azure II, a metachromatic dye that exhibits a shift in absorbance upon electrostatic interaction with heparin. We observed that intact nanoSTATs exhibited little interaction with Azure II while nanoSTATs incubated with thrombin (500 nM) were capable of initiating a significant increase in absorbance at 530nm (**Figure 3.5**).⁷⁷ Taken together, these data demonstrate that heparin is shielded from external charge interactions when complexed, and that thrombin cleavage of the PEG-LVPR.RK4 causes the dissociation of the charge-based nanoSTATs and results in the release of heparin.

To investigate whether the complexation of heparin modulates its anti-clotting activity, we performed an anti-Factor Xa (FXa) assay on samples of intact and thrombin-cleaved

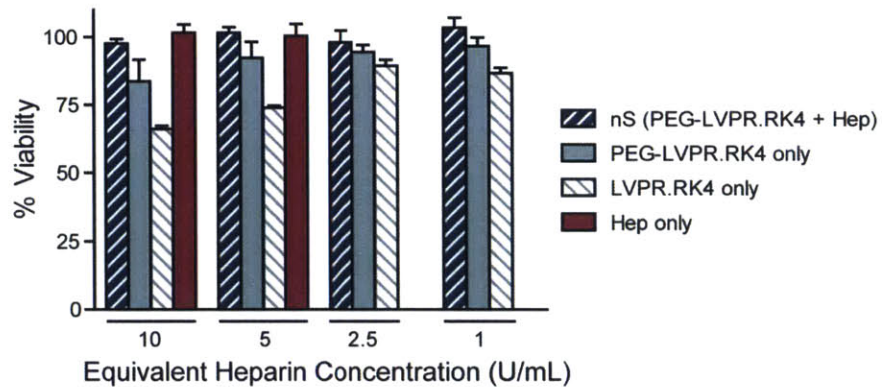


Figure 3.3. Cell viability assay. Percent viability of HUVECs incubated with varying concentrations of nanoSTATs (nS), PEG-LVPR.RK4, LVPR.RK4, and free heparin as determined by a MTS assay (n = 3 per condition).

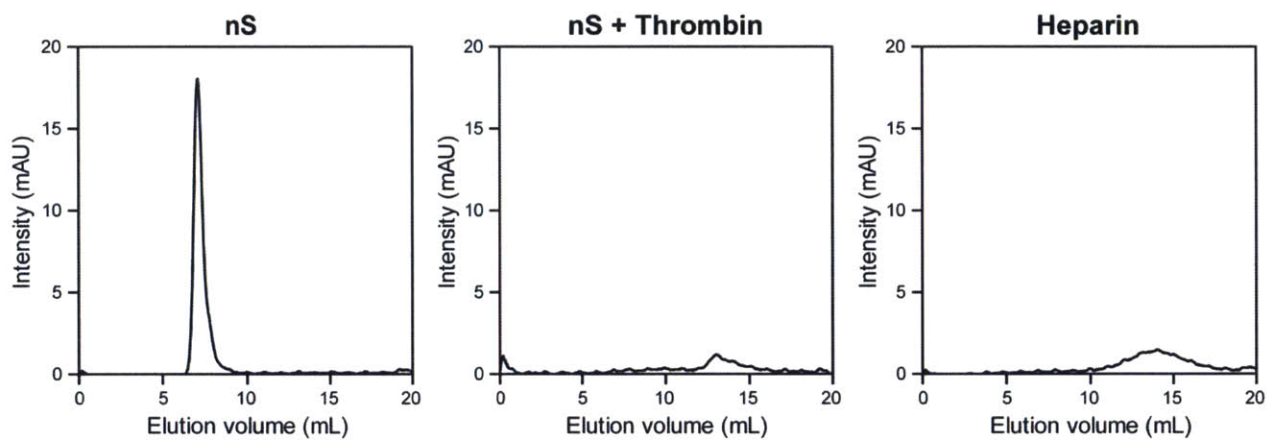


Figure 3.4. FPLC analysis of nanoSTATs. FPLC chromatograms of intact nanoSTATs (nS), nanoSTATs incubated with thrombin, and free heparin as monitored by absorbance at 488 nm.

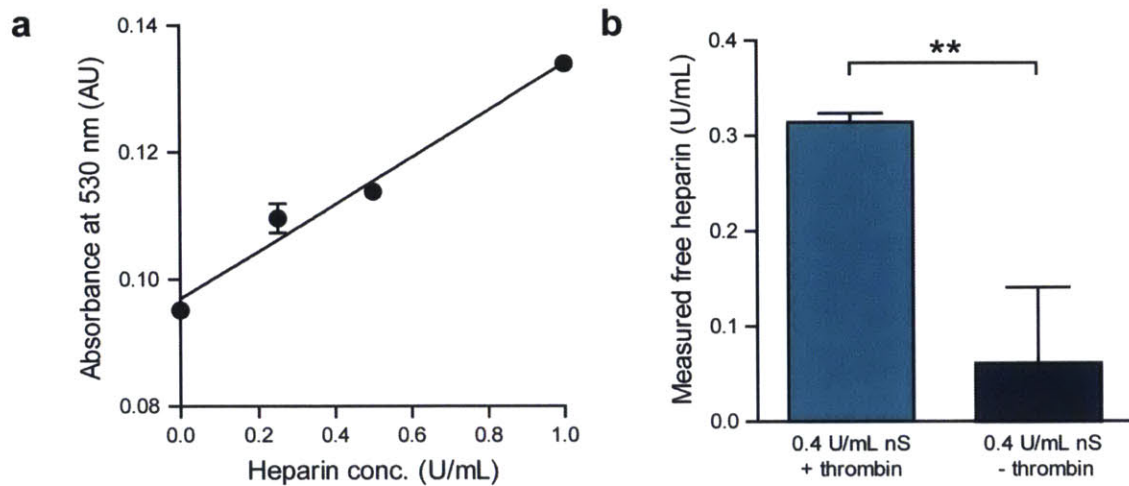


Figure 3.5. Azure II assay for heparin quantification. (A) Standard curve of free heparin mixed with Azure II (slope = 0.037, y-intercept = 0.097, $r^2 = 0.98$; $n = 3$ per condition, s.d.). (B) Free heparin from nanoSTATs quantified before and after incubation with thrombin by Azure II assay. Absorbance was compared to the standard curve of free heparin from (A) to determine the amount of free heparin ($n = 3$ per condition, s.d.).

nanoSTATs. This assay measures heparin activity based on its capacity to inhibit the enzymatic activity of FXa, one of several serine protease targets of heparin, using a chromogenic substrate. Intact heparin-containing nanoSTATs reduced heparin activity by ~80% relative to free heparin, while heparin activity was fully restored when nanoSTATs were incubated with thrombin (**Figure 3.6A**). Heparin activity did not differ between pre-formed complexes incubated with thrombin and free heparin mixed with peptides that had been previously cleaved by thrombin, confirming that peptide cleavage sites remain accessible while embedded in nanoSTATs, and that cleaved LVPR.RK4 fragments are unable to inhibit anticoagulant activity. Furthermore, incubation of nanoSTATs formed with D-stereoisomers of LVPR.RK4 (which confers resistance against protease cleavage) with thrombin led to minimal unveiling of heparin activity, supporting the interpretation that thrombin cleavage of LVPRG sites is responsible for the functional unveiling of heparin. These experiments show that our peptide-heparin nanoSTATs veil heparin activity when intact but release fully functional heparin in response to thrombin cleavage.

Coagulation is a dynamic process where as little as ~10–30 nM of activated thrombin is needed to form a fibrin clot and up to 300–1000 nM of total thrombin can be generated within minutes.¹² To investigate the kinetics of heparin release under physiologically relevant conditions, we incubated nanoSTATs with different concentrations of thrombin (1–1000 nM) and monitored heparin release following defined periods (2, 5, and 10 min) by the anti-FXa assay. As anticipated, the observed elevation in heparin release followed the track of increasing thrombin concentration, reaching a plateau of nearly complete release (>95%) in response to 180 nM thrombin for all incubation times tested (**Figure 3.6B**). Similarly, heparin release increased over time in response to thrombin exposure across the range of concentrations tested. These data indicate that heparin release is a function of thrombin activity and time at physiologically

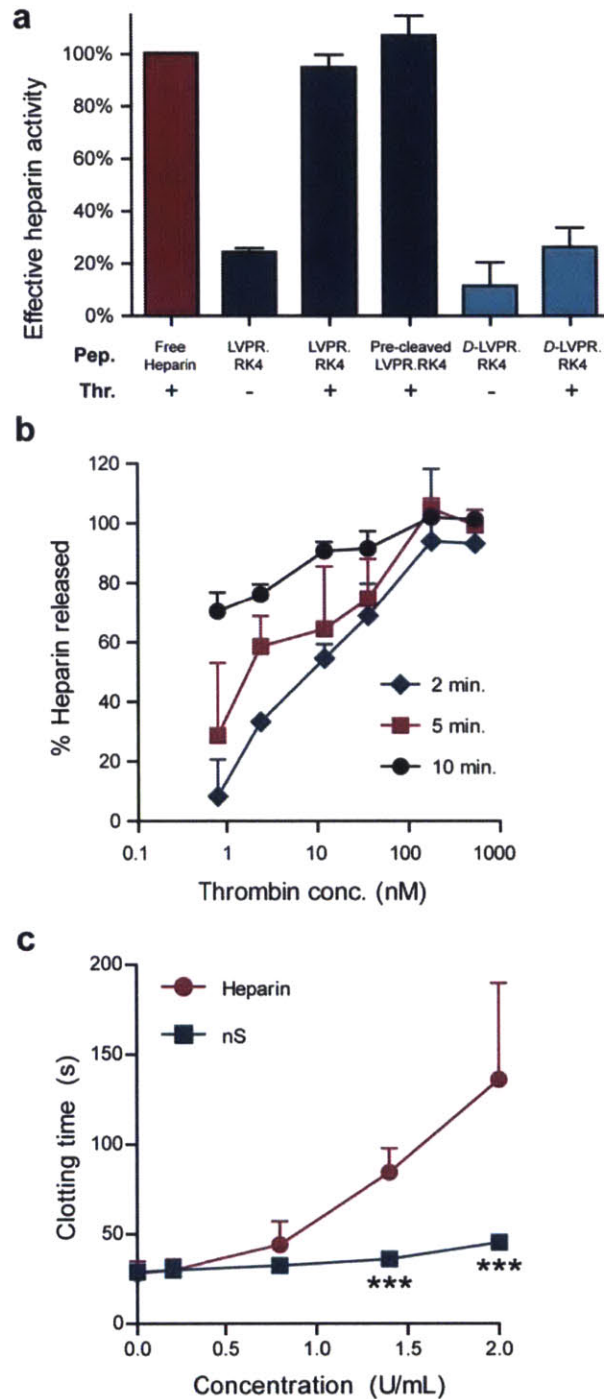


Figure 3.6. *In vitro* nanoSTAT drug release and function. (A) Heparin activity when complexed with peptides and incubated with thrombin, as determined by anti-FXa assay ($n = 3$ per condition, s.d.). Pep, peptide; *D*, D-isomer; Thr, thrombin. (B) Release profile of heparin from nanoSTATs as a function of thrombin concentration and incubation time. Amount of heparin released was determined by anti-FXa assay ($n = 3$ per condition, s.d.). (C) Activated partial thromboplastin time of normal human control plasma spiked with free heparin or nanoSTATs (nS) ($P < 0.001$ by Student's *t*-test; $n = 3$ per condition, s.d.).

relevant concentrations and timescales, behavior which reflects the self-titrating properties of nanoSTATs.

nanoSTATs do not prolong clotting time in vitro. To test the effect of nanoSTATs on plasma, we performed an activated partial thromboplastin time (aPTT) clotting assay, which is used clinically to monitor heparin levels in patients by measuring the time it takes a plasma sample to clot when coagulation is triggered by an activator such as silica or ellagic acid. Current clinical guidelines for heparin treatment recommend dose ranges that yield aPTTs ~1.5–2.3 fold above the control bleeding time, which yields a relatively narrow therapeutic window that is further complicated by the need for each laboratory to internally standardize and validate their own reference ranges.^{274, 287} In human plasma samples spiked with free heparin, the clotting time increased dramatically in a dose-dependent manner from ~29 s in the absence of heparin (0 U/mL) up to ~44s (~1.5 fold over control) with exposure to only 0.4 U/mL, and as long as ~136 s (~5 fold over control) for 2.0 U/mL (**Figure 3.6C**). In contrast, plasma samples spiked with identical doses of heparin nanoSTATs exhibited significantly shorter increases in clotting time, reaching 46 s (~1.5 fold over control) only at a dose of 2 U/mL ($P < 0.001$ by Student's *t*-test, $n = 3-4$ per condition). Our results indicate that relative to the free form, an equivalent dose of heparin sequestered within nanoSTATs does not significantly prolong the aPTT, a marker that is clinically associated with higher risk of bleeding,^{288, 289} and suggests that nanoSTATs may offer a wider therapeutic window with reduced risk of bleeding than with traditional UFH treatment.

nanoSTATs remain veiled in the absence of thrombosis and do not increase bleeding. In the bloodstream, nanoSTATs must navigate a complex milieu of proteins and plasma components without experiencing premature release of their cargo until exposed to sites of thrombus formation. To validate whether anticoagulant activity of nanoSTATs remains

suppressed *in vivo* under healthy conditions, we performed two sets of circulation time experiments. First, using fluorescently-labeled heparin, we sampled the blood of mice injected with either nanoSTATs or free heparin (100 U/kg, n = 3 mice) and measured the plasma fluorescence over time (**Figure 3.7A**). These results indicated that nanoSTATs exhibited a rapid initial clearance half-life within minutes, while a secondary half-life persisted for greater than an hour, which was consistent with the clearance behavior of other heparin-functionalized nanoparticles.²⁹⁰ Next, we injected mice with either nanoSTATs or free heparin and tested the plasma for heparin activity using the anti-FXa assay (**Figure 3.7B**). This experiment showed that unlike the functional activity of free heparin which matched its fluorescence signal, nanoSTATs exhibited little to no heparin activity at any of the measured time points. Together, these studies showed that nanoSTATs veil heparin function while in circulation, leading to reduced levels of heparin activity in the blood pool relative to free heparin.

The primary side effect of clinical anticoagulants, including heparin, is moderate to potentially fatal bleeding.^{272, 273} To assess whether nanoSTATs reduce bleeding side effects, we performed tail transections on mice after they were treated intravenously with nanoSTATs (200 U/kg), free heparin (200 U/kg), or PBS (control), and measured the time elapsed until bleeding ceased (**Figure 3.7C**). Free heparin increased the mean bleeding time of mice (~9.2 min.) by greater than 280% over that of control PBS-treated mice (~3.3 min.). By contrast, the mean bleeding time of nanoSTAT-treated mice (~4.3 min.) was significantly shorter than that of the heparin-treated group and only 30% longer than the control bleeding time ($P < 0.01$ by one-way ANOVA with Tukey post test, n = 5–7 mice). The reduction in the bleeding time of mice administered with nanoSTATs versus free heparin suggests that the level of thrombin activity in response to injury did not unveil sufficient heparin to significantly impact bleeding cessation.

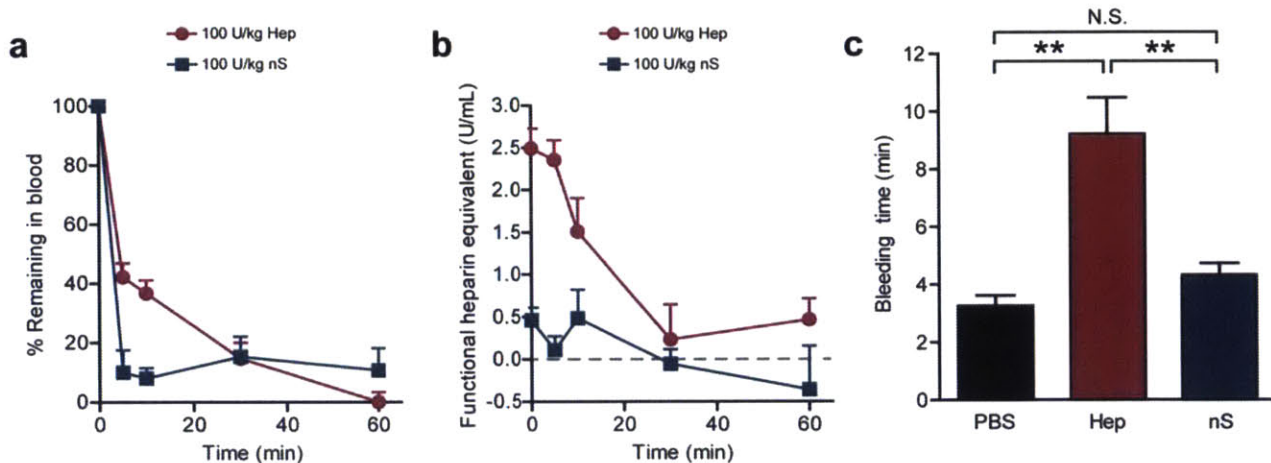


Figure 3.7. *In vivo* bleeding time of nanoSTATs. (A) Circulation time of nanoSTATs (nS) and free heparin as determined by fluorescence using FITC-heparin ($n = 3$ mice, s.e.). (B) Circulation time of nanoSTATs (nS) and free heparin (Hep) as determined by anti-FXa assay on mouse plasma samples withdrawn over time ($n = 3$ mice, s.e.). (C) Tail bleeding time of mice administered 200 U/kg of free heparin or nanoSTATs (** $P < 0.01$ by one-way ANOVA with Tukey post test; $n = 5-7$ mice, s.e.).

This finding may be due to the fact that sealing major wounds is largely dependent on platelet activation and plug formation, a process that requires considerably lower levels of activated thrombin than during thrombus formation.^{291, 292} Taken together, these data showed that nanoSTATs circulate in an inactive form, veiling heparin activity and decreasing the risk of bleeding.

nanoSTATs prevent thrombosis in vivo. To evaluate the ability of nanoSTATs to prevent thrombosis *in vivo*, we utilized a thromboplastin-induced model of pulmonary thromboembolism, which we and others have shown leads to deposition of microembolisms primarily in the lungs (**Figure 3.8**).^{241, 293} Mice were administered fibrinogen labeled with near-infrared dyes to monitor the formation of fibrin clots in the lungs by fluorescent imaging after thromboplastin challenge (2 μ L/g b.w.). The lungs of mice treated with nanoSTATs (200 U/kg) showed a ~75% reduction ($P < 0.01$, one-way ANOVA with Tukey post-test, $n = 5$ mice) in the burden of clots compared to the lungs of control-treated mice (**Figure 3.9A & B**). This reduction in the formation of clots caused by nanoSTATs was statistically equivalent to the therapeutic efficacy achieved by the corresponding dosage of free heparin (200 U/kg, **Figure 3.10**). Moreover, histological analysis showed that microvessels in the lungs of control-treated animals contain thrombi (arrows in **Figure 3.9C**, top right panel), whereas such vessels in animals treated with either free heparin or nanoSTATs were largely patent, as evidenced by the presence of red blood cells (arrow heads in **Figure 3.9C**). Combined with the data from the tail bleeding assay, these observations suggest that nanoSTATs prevent thrombosis as effectively as free heparin but with a significantly reduced risk of bleeding.

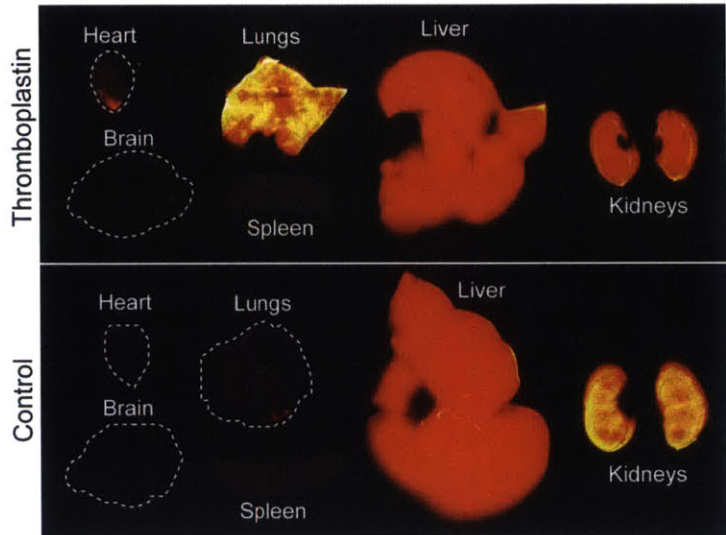


Figure 3.8. Deposition of VT750-fibrin in thromboplastin-induced model of thrombosis. Near-infrared fluorescent scans of excised organs to assess VT750-NW distribution following intravenous injection of thromboplastin (2 μ L/g b.w.) or PBS.

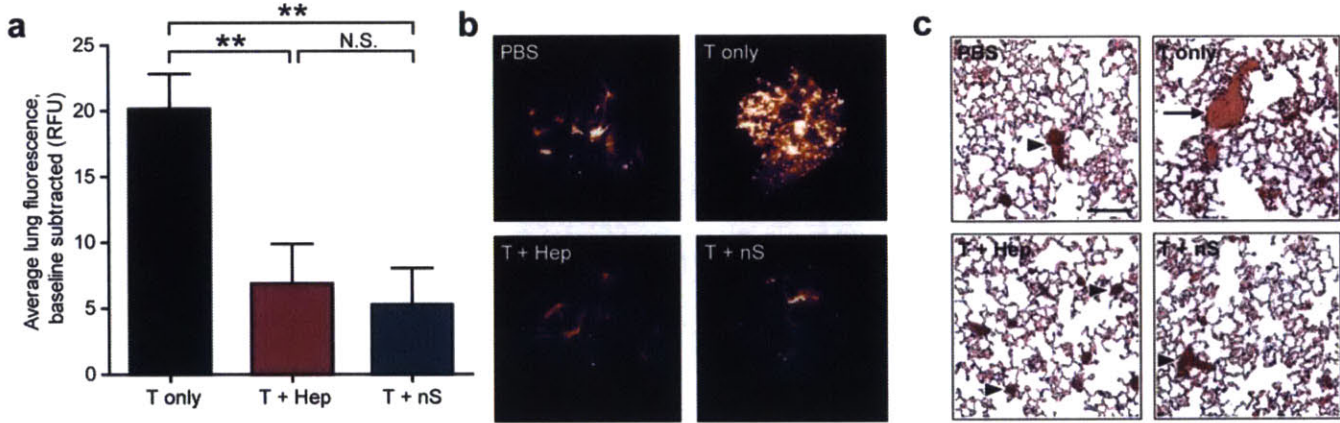


Figure 3.9. *In vivo* therapeutic efficacy of nanoSTATs. (A) Quantification of fibrin deposited in the lungs of mice dosed with thromboplastin (T, 2 μ L/g body weight) and nanoSTATs (nS, 200 U/kg) or free heparin (Hep, 200 U/kg) (** P < 0.01 by one-way ANOVA with Tukey post test; n = 5 mice, s.e.). (B) Near-infrared fluorescent scans of excised lungs to assess VT750-labeled fibrinogen following intravenous injection of PBS, T only, T + nS, and T + Hep. (C) H&E staining of lungs in mice under the same conditions as in (B). Arrow denotes fibrin clots; arrowheads denote patent vessels (scale bar = 100 μ m).

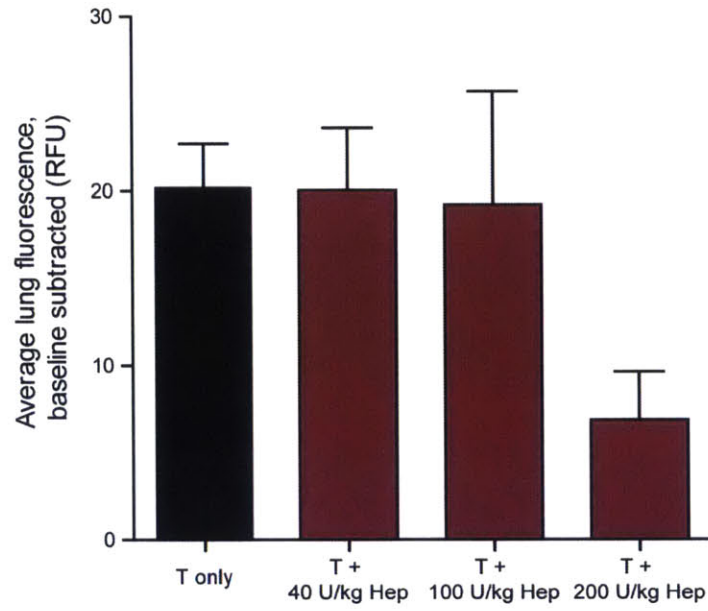


Figure 3.10. Heparin dose response in thromboplastin-induced thrombosis model. Quantification of fibrin deposited in the lungs in response to escalating doses of heparin (Hep) (n = 3–5 mice, s.e.).

3.4 Discussion

Anticoagulation is vital for the prophylaxis and treatment of life-threatening thrombosis, yet inhibiting the body's natural ability to form blood clots predisposes patients to severe bleeding complications; the ideal anticoagulant is a drug that prevents coagulation without promoting bleeding.^{9, 273} Here, we engineered a nanocomplex that autonomously titrates the release of anticoagulant in response to endogenous levels of activated thrombin in thrombosis, creating a negative feedback circuit that regulates the coagulation cascade with negligible increases to the risk of bleeding. While Maitz et. al. also recently assessed the function of a self-regulating anticoagulant material through *ex vivo* simulations, we tested our nanoSTATs *in vivo* and demonstrated therapeutic and safety characteristics that can only be investigated in animal models. Furthermore, our nanoformulation is designed for systemic thrombosis prevention in contrast to their hydrogel platform that is better suited for highly localized anticoagulation applications (e.g. surface coating of blood contacting medical devices).²⁷¹ Engineering approaches have also been used to design bioresponsive thrombolytics – antithrombotic therapy designed to dissolve existing clots rather than prevent their formation – including recombinant proteins^{292, 294} or polymeric microparticles⁹¹ activated by proteolytic or biophysical triggers associated with thrombosis that decrease bleeding and expand therapeutic windows. Looking forward, several clinical applications warrant further investigation with our nanoSTATs. Since the model used here mimics the development of emboli in the microvasculature, future testing will assess nanoSTATs' ability to treat thrombosis in larger vessels, which are representative of clinical situations such as myocardial infarction or thrombotic stroke.^{295, 296} Further studies are also needed to understand the impact of the nanoSTAT formulation on other side effects

associated with UFH, such as heparin-induced thrombocytopenia and platelet dysfunction.^{41, 297,}

298

Numerous recent nanoscale drug delivery systems utilize responsiveness to biological stimuli to control drug biodistribution *in vivo*.^{6, 8} A majority of these systems operate without the ability to self-regulate; such nanoparticles are adequate for site-directed delivery, but impractical for applications requiring adjustable functionality under varying biological conditions. Only a small number of self-regulating nanocarriers have been developed, with glucose-responsive insulin delivery being the most well-known example.^{299, 300} In contrast to the glucose-insulin feedback loop which functions over several hours through the body's downstream response to insulin to indirectly affect the initial glucose trigger,³⁰¹ we have designed a direct negative feedback loop that immediately modulates its proteolytic trigger in conjunction with a single readily available effector, an approach that is well-suited for regulating enzymatic cascades that operate on rapid timescales. Our strategy was achieved through facile non-covalent modification of the clinically approved anticoagulant, UFH, using biocompatible materials, which may mitigate the translational risk of this nanotherapeutic. A more detailed examination of the nanoSTATs' impact on hemodynamic parameters and immunological markers would help to verify the *in vivo* safety of the system.²⁸² The clearance kinetics of nanoSTATs suggest they may be well-suited for administration by continuous infusion in an in-patient setting where rapid cessation of anticoagulation is often required in order to undertake further medical procedures. Potential improvements to our system include the use of alternative peptide substrates that are sensitive to upstream coagulation factors like FXa,³⁰² further functionalizing nanoSTATs with fibrin-targeted ligands to concentrate drugs in areas of clotting,^{27, 37, 172} and delivering direct coagulation inhibitors instead of UFH.³⁰³ Furthermore, this paradigm is readily extensible to the

regulation of additional disease-associated proteases *via* the modular protease-sensitive and therapeutic-binding domains, enabling the design of next generation self-titrating medicines.

3.5 Conclusion

In conclusion, this work represents, to the best of our knowledge, the first self-titrating anticoagulant nanoformulation that decreases the risk of bleeding while maintaining antithrombotic efficacy. By incorporating negative feedback control, nanoSTATs further expand the repertoire of nanomedicines available for the treatment of thrombosis and may lead to the development of safer antithrombotics.

3.6 Materials and Methods

Peptide synthesis and functionalization. Peptides (LVPR.RK4 = rkrkLVPRGrkrkLVPRGrkrkLVPRGrkrk, lower case = D-isomer) were synthesized by standard Fmoc solid-phase peptide synthesis (Koch Institute Biopolymers Core or Tufts University Core Facility), lyophilized, and resuspended at 5 mg/mL in ddH₂O. Peptides were PEGylated through incubation of 5 mg/mL stock peptide solution with amine-reactive 5,000 Da poly(ethylene glycol)-succinimidyl valerate (PEG-SVA, Laysan Bio Inc.) for 1 hour at room temperature.

Physical characterization of nanoSTATs. NanoSTATs were generated with peptide and PEG molar ratios as reported, with a fixed heparin (sodium salt from porcine mucosa, Sigma, ~18,000 Da) concentration of 20 U/mL (~0.1 mg/mL) unless reported otherwise. For measurements in ionic solutions, 10x PBS stock was added to pre-formed nanoSTAT solutions for a final concentration of 1x PBS. For measurements in serum, bovine serum (Gibco) was added to a concentration of 10% (v/v). Mean hydrodynamic diameter was determined via dynamic light scattering of a 50 µL sample at 20 U/mL heparin (ZetaSizer Nano Series, Malvern). Zeta potential was measured *via* electrophoretic light scattering on a 900 µL particle sample at 20 U/mL (ZetaSizer Nano Series). The morphology of nanoSTATs were visualized *via* transmission electron microscopy using a JEOL 2100FEG.

Veiling and unveiling of function in vitro. The heparin activity of intact nanoSTATs was determined using the anti-FXa assay (Sekisui Diagnostics) according to manufacturer instructions. The release of heparin was determined by incubating nanoSTATs with various concentrations of human thrombin (Haematologic Technologies) at 37°C for the reported

amounts of time. The activity of the released heparin was then determined using the anti-FXa assay.

Cytotoxicity assays. Human umbilical vein endothelial cells (HUVEC, Passage 9) were cultured in EGM-2 media (Lonza) on a 96-well plate. When cells reached 70% confluency, nanoSTATs, PEG-LVPR.RK4, free LVPR.RK4, or free heparin were added as 9x stocks in PBS, diluted in EGM-2. After 24 hours elapsed, cells viability was quantified by MTS Assay (CellTiter AQueous One, Promega) based on OD490 after 1 hour incubation.

FPLC analysis. NanoSTATs were formulated as described above using fluorescently-labeled (FITC) heparin (Polysciences). A sample of nanoSTATs was incubated with thrombin (500 nM) at 37°C for 30 minutes. Analytical samples of nanoSTATs, nanoSTATs incubated with thrombin, and free heparin were applied to a Superdex 200 column pre-equilibrated with PBS. Absorbance of the column effluent was monitored at a wavelength of 488 nm by a UV flow-through detector.

Azure II assay. A sample of nanoSTATs was incubated with thrombin at 37°C for 30 minutes. NanoSTATs, nanoSTATs incubated with thrombin (500 nM), and free heparin were then mixed with 0.1 mg/mL Azure II solution at a 1:10 volumetric ratio and the absorbance was read at 530nm with a SpectraMAX Plus spectrophotometer (Molecular Devices).

APTT assay. Varying concentrations of nanocSTATs or free heparin were added to 50 uL of control normal human plasma (Thermo Scientific) and incubated with 50uL of APTT reagent

(Thermo Scientific) at 37°C for 3 minutes. Then 50uL of 25mM CaCl₂ (Sigma) pre-incubated at 37°C were added to samples and clotting was monitored via absorbance at 605nm with a SpectraMAX Plus spectrophotometer (Molecular Devices).

Circulation times. Healthy female Swiss Webster mice (3-4 months, n = 3 mice per condition) were injected via tail vein with either nanoSTATs or free heparin at 100 U/kg, formulated with 1x PBS. For measurement of heparin fluorescence, blood samples collected through retro-orbital blood draw and centrifuged at 2900g for 5 minutes to isolate plasma, which was then analyzed by fluorimetry using the Spectramax Gemini EM Fluorescence Microplate Reader (Molecular Devices) at excitation/emission wavelengths of 485/538 nm. For measurement of anti-FXa activity, blood samples were collected in tubes containing 3.2% sodium citrate (Sigma) for a final volume ratio of 9:1 (blood:citrate) through retro-orbital blood draws and centrifuged at 2900g for 5 minutes to isolate the plasma. Heparin activity in the plasma was then determined using the anti-FXa assay.

Tail-bleeding time assay. Mice (n = 5–7 per condition) were anesthetized with isoflurane gas and administered nanoSTATs (200 U/kg), free heparin (200 U/kg), or PBS control. After 5 minutes, 2 mm of distal mouse tail was removed by scalpel. Bleeding time was determined by lightly dabbing the tail with kimwipe tissues (Kimtech) until bleeding fully ceased for at least 1 minute.

Pulmonary embolism assay. Bovine fibrinogen (Sigma) was reacted with near-infrared fluorochromes (Vivotag-750-NHS, Perkin-Elmer) at a 2:1 fluorophore:protein molar ratio in PBS for 1 hr and purified by column centrifugation (100kDa cutoff, Millipore) to remove

unreacted fluorophores. Ampules of thromboplastin from rabbit brain (Sigma, #44213) were reconstituted with 2 mL of PBS each. Mice (n = 5 per condition) were anesthetized with isoflurane gas and co-administered nanoSTATs (200 U/kg), free heparin (200 U/kg), or PBS control and 1nmol of VT750-fibrinogen via tail vein injection. After 5 minutes, mice were injected with thromboplastin (2 uL/g b.w.). After 30 minutes, mice were euthanized with CO₂ and the lungs were harvested and imaged on the LI-COR Odyssey Infrared Imaging System. Fibrin deposition was then quantified using ImageJ software. For histologic analysis, paraffin-embedded sections of lungs were prepared (Koch Institute Histology Core). Lungs were first fixed by incubating in 4% paraformaldehyde overnight. Hematoxylin and eosin immunochemical staining of lung sections was used to visualize clots in the lungs.

Statistical analyses. Student's *t*-test and ANOVA analyses were calculated with GraphPad 5.0 (Prism).

All experimental protocols involving animals were approved by the MIT Committee on Animal Care (protocol #0411-036-14).

3.7 Acknowledgements

Nikita Consul, Justin Lo, and Dr. Gabriel Kwong were co-authors on this work. We thank the Koch Institute Swanson Biotechnology Center (MIT) for assistance with tissue sectioning, specifically Michael Brown and Kathleen Cormier from the Histology core. We thank Dr. Heather Fleming (MIT) for critical readings of the manuscript. This work was supported by the NIH (BRP: R01CA124427-01), NIH/NCI (U54CA119349, U54CA119335, and the Alliance

Challenge Project/MIT-Harvard Center of Cancer Nanotechnology Excellence: U54CA151884), Packard Fellowship (1999-1453), and Marie-D. & Pierre Casimir-Lambert Fund. This work was supported in part by the Koch Institute Support (core) Grant P30-CA14051 from the National Cancer Institute. K.Y.L. acknowledges support from CCNE (5 U54 CA151884-03). J.H.L. acknowledges support from NIH MSTP program (T32GM007753). Dr. G.A.K. acknowledges support from the Ruth L. Kirschstein National Research Service Award (F32CA159496-02) and holds a Career Award at the Scientific Interface from the Burroughs Wellcome Fund. Dr. S.N.B. is an HHMI Investigator. The authors wish to dedicate this paper to the memory of Officer Sean Collier, for his caring service to the MIT community and for his sacrifice.

Chapter 4: Drug-Induced Amplification of Nanoparticle Targeting to Tumors

4.1 Abstract

Nanomedicines have the potential to significantly impact cancer therapy by improving drug efficacy and decreasing off-target effects, yet our ability to efficiently home nanoparticles to disease sites remains limited. By exploiting tumor-specific responses to drugs, we construct a cooperative targeting system where a small molecule therapeutic modulates the disease microenvironment to amplify nanoparticle recruitment *in vivo*. We first administer a vascular disrupting agent, ombrabulin, which selectively affects tumors and leads to locally elevated presentation of the stress-related protein, p32. This increase in p32 levels provides more binding sites for circulating p32-targeted nanoparticles, enhancing their delivery of diagnostic or therapeutic cargos to tumors. We show that this cooperative targeting system recruits over five times higher doses of nanoparticles to tumors and decreases tumor burden when compared with non-cooperative controls. These results suggest that using nanomedicine in conjunction with drugs that enhance the presentation of target antigens in the tumor environment may be an effective strategy for improving the diagnosis and treatment of cancer.

4.2 Introduction

Nanotechnology has enabled numerous novel and improved approaches for cancer diagnosis and therapy. In particular, active targeting of nanoparticles, or the attachment of affinity ligands to the surface of particles to recognize and bind pathological markers, has arisen as an attractive strategy for precisely delivering cargos to disease sites while simultaneously reducing side effects.¹ Efforts to improve the targeting of nanomaterials have largely focused on

engineering the properties of individual nanoparticles, including geometry, surface chemistry, ligand type, and ligand density.^{4, 177, 284} However, one major factor that limits the effectiveness of active targeting is the paucity of targetable antigens available for nanoparticle binding within a tumor.¹⁸⁰ A promising approach for overcoming this limitation is to leverage disease responses to therapy to greatly enhance the number of existing binding sites, or induce the presentation of novel targets. Previously, localized treatments such as radiation³⁰⁴ and hyperthermia^{182, 184} have been used to induce the expression of vascular antigens that serve as binding targets to recruit nanoparticles to tumors. Unfortunately, application of these methods is confined to clinical scenarios where disease sites are known and accessible, and thus preclude the treatment of disseminated disease, which is the primary cause of mortality in cancer.³⁰⁵

Our strategy is to identify proteins that are selectively induced in the tumor microenvironment following treatment with drugs and leverage them as receptors for targeted nanoparticles. The arsenal of systemic therapies designed to treat metastatic cancer includes traditional cytotoxic drugs,⁹⁸ molecularly targeted agents,^{306, 307} immunotherapy,^{100, 308} and vascular disrupting agents (VDAs),^{187, 309} which operate through distinct modes of action. These drugs are attractive inducing agents because many are clinically-approved or in trial stages and are frequently administered in combination with other therapeutics.^{306, 307, 310} Drug-induced antigens have been utilized as biomarkers of therapeutic responses or as antibody targets,³¹¹⁻³¹³ but to our knowledge, these changes have never been used to target nanoparticles to tumors. Here, we investigate the ability of systemically administered drugs to increase the prevalence of tumor-specific antigens to amplify nanoparticle targeting to tumors. In this report, we demonstrate that the small molecule VDA, ombrabulin, enhances the presentation of a stress protein called p32 in human tumor xenografts implanted in mice (**Figure 4.1**). p32 is specifically

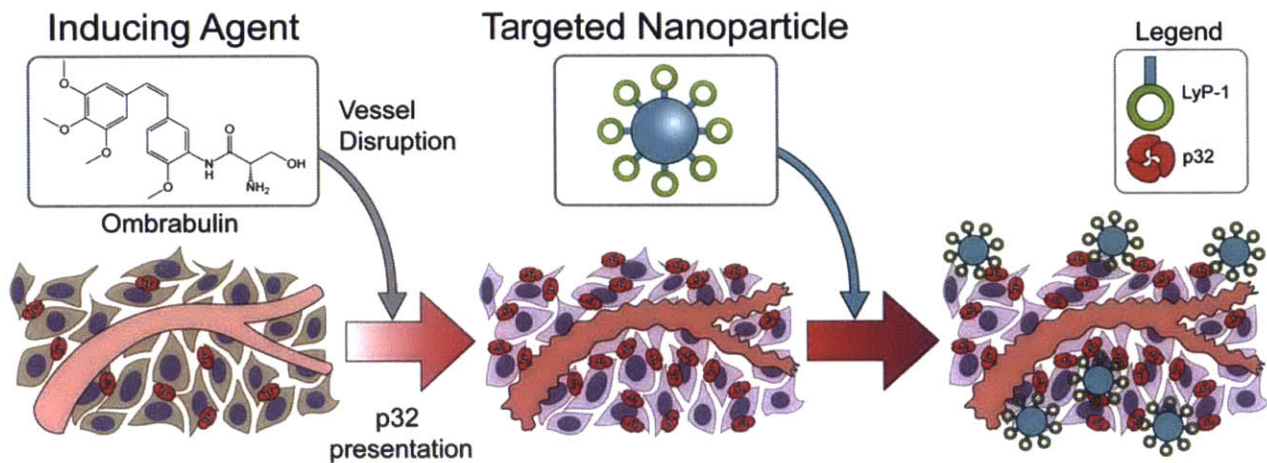


Figure 4.1. Schematic of cooperative targeting approach. Inducing agent, ombrabulin, disrupts the tumor vasculature, which initiates a cascade of intratumoral effects that leads to upregulated presentation of the p32 protein. LyP-1 coated nanoparticles that target the p32 protein then home to the tumor.

expressed in tumors and serves as the target receptor of the cyclic nonapeptide, LyP1, which was discovered through *in vivo* phage display.^{183, 185} We then use ombrabulin to induce greater levels of p32 in tumors and deliver two different LyP1-decorated nanoparticles to tumors: a prototypical imaging agent (magnetofluorescent iron oxide nanoworms) and a prototypical therapeutic agent (doxorubicin-loaded liposomes). We show that this cooperative targeting system amplifies the recruitment of targeted nanoparticles to tumors by three- to five-fold over non-cooperative controls, and improves the tumor burden and survival of mice in a preclinical therapeutic study.

4.3 Results

Characterization of ombrabulin-induced p32 presentation. Ombrabulin is a microtubule-binding agent that impacts tumor vasculature by effecting a rapid sequence of events shortly after administration, including morphological and functional changes in endothelial cells that increase vascular permeability, and culminate in extensive hemorrhagic necrosis within the tumor (**Figure 4.2A-C**).^{187, 314, 315} The selective vulnerability of tumor vessels to tubulin-binding compounds has been attributed their immature development and defective pericyte coverage relative to normal vessels.^{187, 309} We hypothesized that the antitumor activity of ombrabulin might increase tumor presentation of p32 [p33/gC1q receptor/hyaluronan binding protein 1 (HABP1)], a mitochondrial protein that is found at elevated levels on the surface of stressed tumor and tumor-associated cells in a wide range of tumor types, particularly in hypoxic or nutrient-deprived regions.¹⁸³ To investigate the ability of ombrabulin to increase p32 presentation within tumors, we intravenously injected different doses of the drug (0, 30, 60 mg/kg) into nude mice (n = 3 mice per condition) bearing bilateral human MDA-MB-435 tumors. At 4 and 24 hrs, mice were euthanized and p32 presentation was assessed *via* immunofluorescent staining of tumor sections

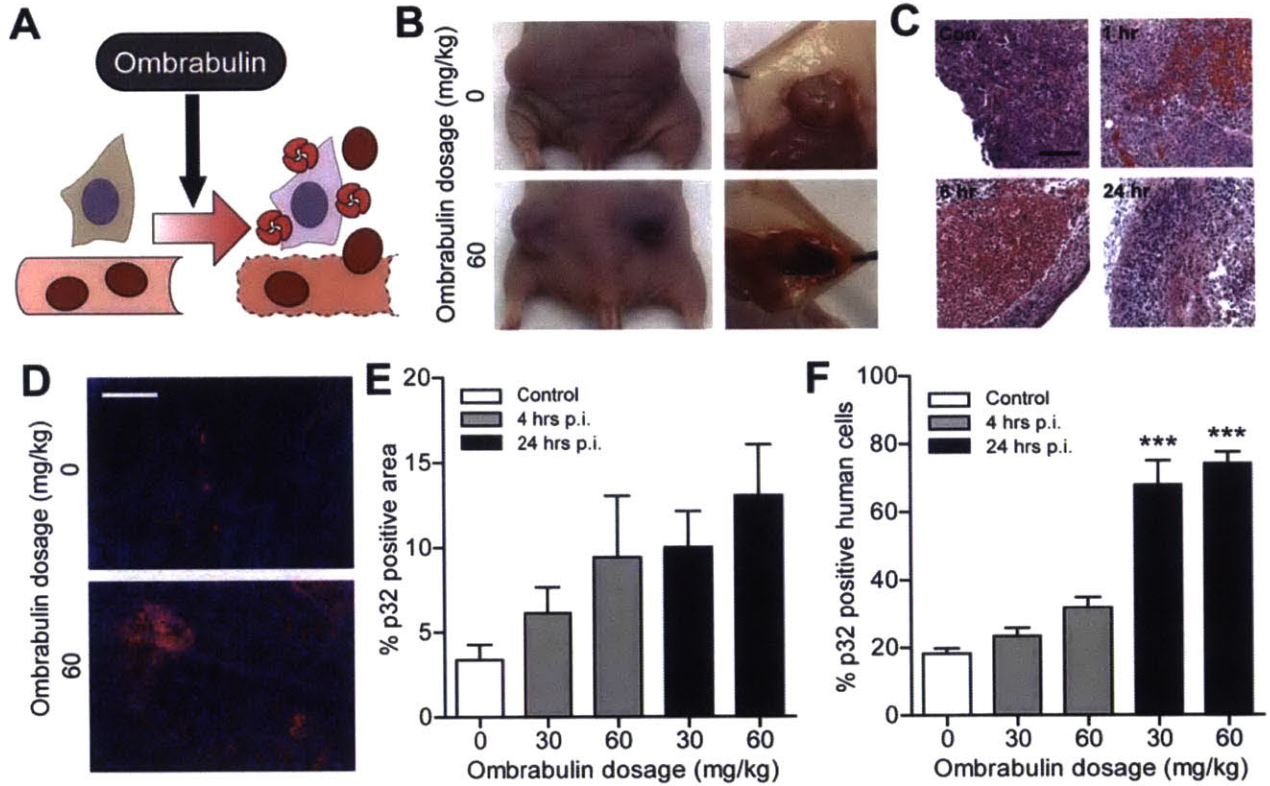


Figure 4.2. Characterization of omrabulin effect on tumor microenvironment. (A) Schematic of omrabulin-induced enhancement in p32 presentation. (B) Intraoperative images at 24 hr post injection (p.i.) revealing omrabulin mediated hemorrhaging. (C) Hematoxylin and eosin staining of tumors harvested from mice injected with omrabulin at different timepoints p.i. (Con., control (0 mg/kg); scale bar = 100 μ m). (D) Immunofluorescent staining of tumors without (0 mg/kg) and with (60 mg/kg) omrabulin (red = p32 staining, blue = nuclear stain; scale bar = 1 mm). (E) Quantification of percentage p32 positive area of immunofluorescent staining of tumors receiving different dosages of omrabulin at different timepoints p.i. (n = 3 mice, s.e.). (F) Quantification of percentage p32 positive human cells from tumors receiving different dosages of omrabulin at different timepoints as determined by flow cytometry (***) $P < 0.005$, one-way ANOVA with Tukey post test; n = 3 mice, s.e.).

(**Figure 4.2D**). We observed that the percentage of p32-positive staining within the tumor trended upward with both time and ombrabulin dose, showing nearly a four-fold increase in p32-positive area at 24 hrs after a 60 mg/kg dose (**Figure 4.2E**). To assay for increased p32 presentation at the surface of surviving cancer cells, tumors were dissociated into single cell suspensions for quantification of p32 surface expression by live-cell staining and flow cytometry (**Figure 4.3**). Consistent with the trend observed in tumor sections, flow-based examination of the tumor population revealed that the percentage of cancer cells positive for surface p32 increased significantly by up to four-fold at 24 hrs after ombrabulin treatment ($*** P < 0.005$ by one-way ANOVA with Tukey post test; **Figure 4.2F**). Together, these data show that exposure to ombrabulin modulates the tumor environment to amplify p32 presentation within the tumor, particularly on the surface of surviving cancer cells.

Ombrabulin-induced amplification of tumor targeting. We next investigated the ability of magnetofluorescent iron oxide nanoworm (NW) imaging agents, a nanoparticle previously developed by our collaborators,^{233, 234} to target tumors following ombrabulin treatment (**Figure 4.4A**). The NWs were first derivatized with a near-infrared fluorophore (VT750) to enable detection of their distribution by fluorescence imaging. Then, the NWs were further modified by the addition of either the cyclic nonapeptide LyP-1 (CGNKRTRGC), which binds p32 and facilitates tissue penetration, or ARAL (ARALPSQRSR), an untargeted peptide that has the same net charge as LyP-1, via PEG linkers.^{183, 184, 316, 317} The LyP-1 (NW-LyP1) and ARAL (NW-ARAL) conjugated NWs shared matching size distributions (hydrodynamic diameter ~50 nm by dynamic light scattering), peptide valencies (~40 peptides per NW by absorbance spectroscopy), and *in vivo* circulation times (half-lives ~ 2.5 hrs; **Figure 4.5**). Additionally, as expected, the NW-LyP1 showed significantly greater binding to recombinant p32 *in vitro*

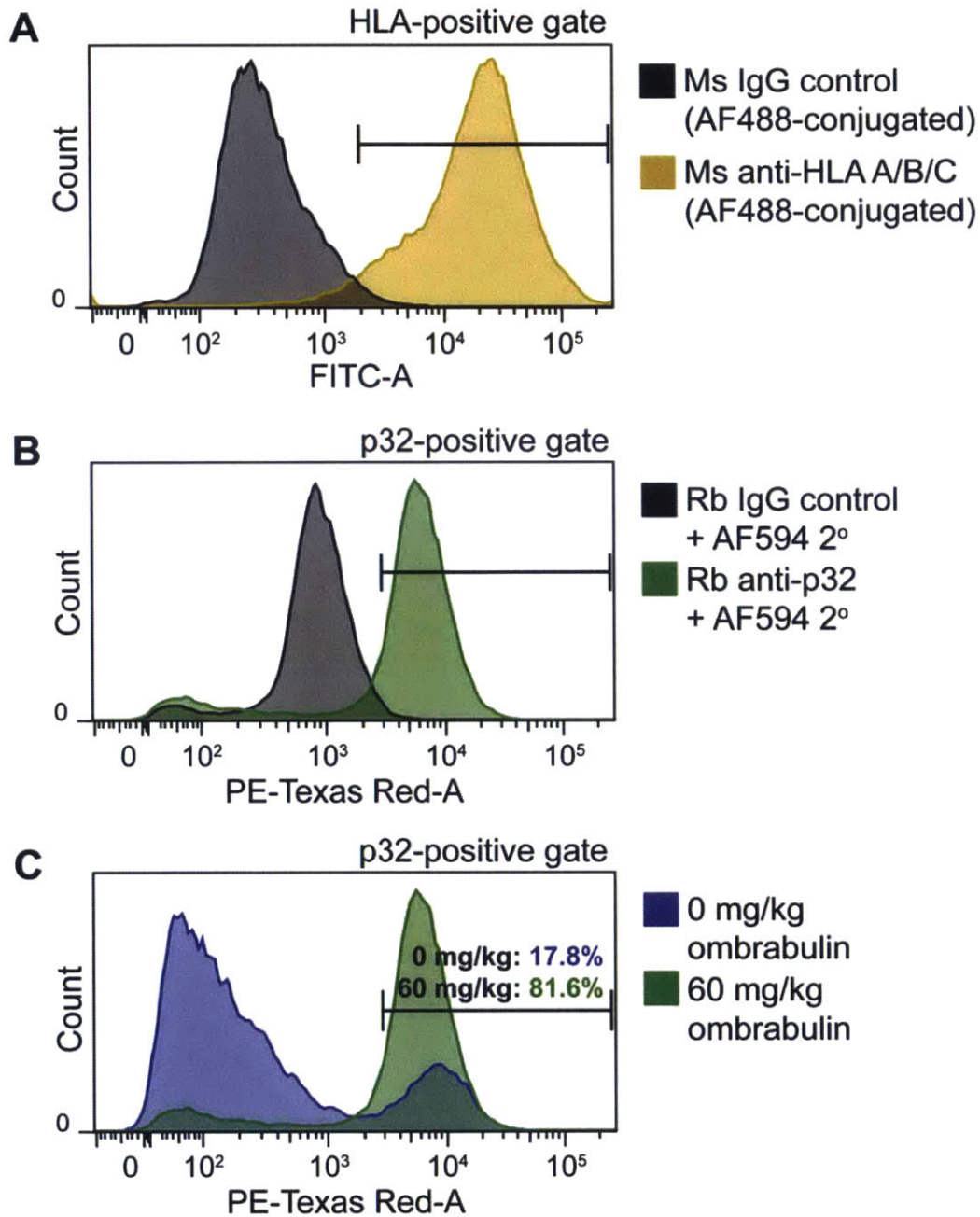


Figure 4.3. Flow cytometry analysis of p32 expression on cells *ex vivo*. (A) Representative histograms of untreated MDA-MB-435 xenograft cells stained with AF488-conjugated mouse IgG control or AF488-conjugated mouse anti-HLA A/B/C, used to exclude non-xenograft cells from final analysis. (B) Representative histograms of *ex vivo* MDA-MB-435 cells 24-hours post treatment with ombrabulin (60 mg/kg), stained with either rabbit IgG control or rabbit anti-p32 antibody to establish the threshold for positive p32 staining. (C) Flow cytometry histogram of *ex vivo* MDA-MB-435 cells stained for p32 following treatment without (0 mg/kg) or with ombrabulin (60 mg/kg).

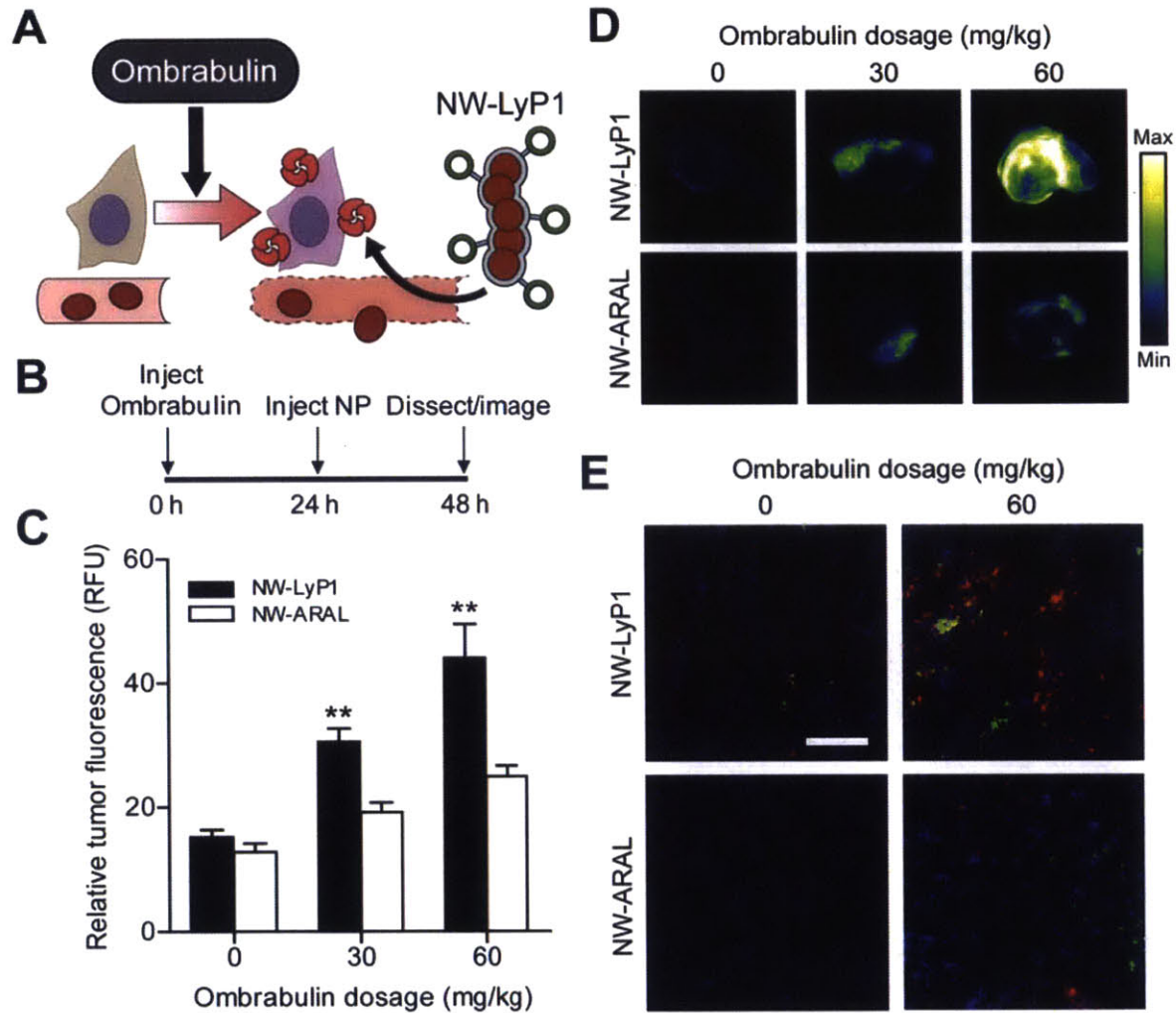


Figure 4.4. Ombrabulin mediated amplification of NW delivery. (A) Schematic of ombrabulin signaling to NWs. (B) Experimental timeline for testing the signaling system. (C) Quantification of NW homing to tumors as a function of ombrabulin dosage (** $P < 0.01$, Student's t -test; $n = 3-4$ mice, s.e.). (D) Representative near-infrared fluorescent scans of NW homing to tumors in response to increasing doses of ombrabulin. Tumors were excised and imaged at 24 hrs post-NW injection. (E) Immunofluorescent staining of NWs in tumors without (0 mg/kg) and with (60 mg/kg) ombrabulin (green = NW, red = p32 staining, blue = nuclear stain; scale bar = 100 μ m).

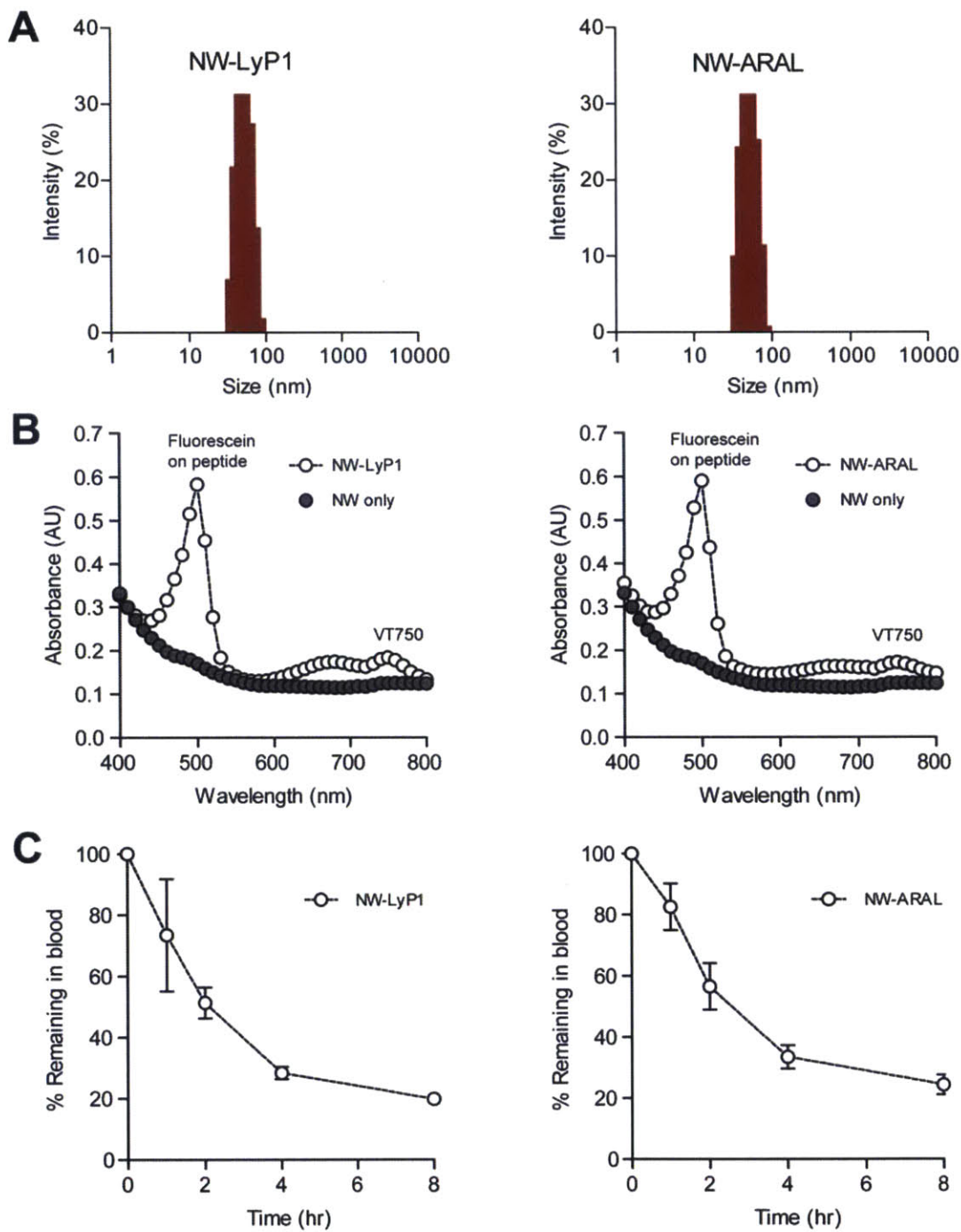


Figure 4.5. *In vitro* characterization of NWs. (A) Size distribution of iron oxide NWs as determined by dynamic light scattering. (B) Absorbance spectra of NWs conjugated with fluorescein-labeled peptides (~500 nm) and VT750 (~750 nm) and free NWs (grey). (C) Circulation time of NWs as determined by near-infrared fluorescence in the blood (n = 3 mice, s.d.).

relative to NW-ARAL, which validated the selection of ARAL as a non-targeted control sequence (**Figure 4.6A**).

To test for amplification of NW targeting to tumors, different doses of ombrabulin (0, 30, 60 mg/kg) were intravenously injected into mice (n = 3–4 mice per condition) bearing bilateral MDA-MB-435 tumors, followed by either NW-LyP1 or NW-ARAL administration after 24 hrs (**Figure 4.4B**). At 24 hrs post-NW injection, *ex vivo* fluorescent imaging of tumors revealed a dose-dependent increase in NW-LyP1 accumulation of up to three-fold relative to no drug controls and without altering the organ distribution of the nanoparticles (**Figure 4.4C-D**, **Figure 4.7**). The non-targeted NW-ARAL also exhibited a marginal dose-dependent increase in accumulation, which is consistent with previous reports demonstrating the enhanced extravasation of macromolecules following vascular disruption by small molecule therapeutics.¹⁹¹ Notably, the NW-LyP1 exhibited a significantly greater increase in accumulation of ~1.5-2 fold compared to the NW-ARAL when following ombrabulin treatment (** $P < 0.01$ by Student's *t*-test), which suggested that induction of p32 presentation by ombrabulin leads to amplified targeting of NWs to tumors. Histological examination of tumor sections revealed that the presence of both NW-LyP1 (green) and p32 (red) increased, and localized within ombrabulin-treated tumors (60 mg/kg) versus untreated tumors, while NW-ARAL (green) staining was less intense and did not colocalize with p32 (red) in either scenario (**Figure 4.4E**). We also explored an alternative dosing sequence in which ombrabulin and NWs were injected simultaneously and found that co-administration did not lead to a pronounced difference in accumulation between NW-LyP1 and NW-ARAL (**Figure 4.8**). This result is consistent with the previous finding that enhancement of p32 presentation takes up to 24 hrs post-ombrabulin treatment, and supports the hypothesis that p32 binding is necessary for the enhanced targeting

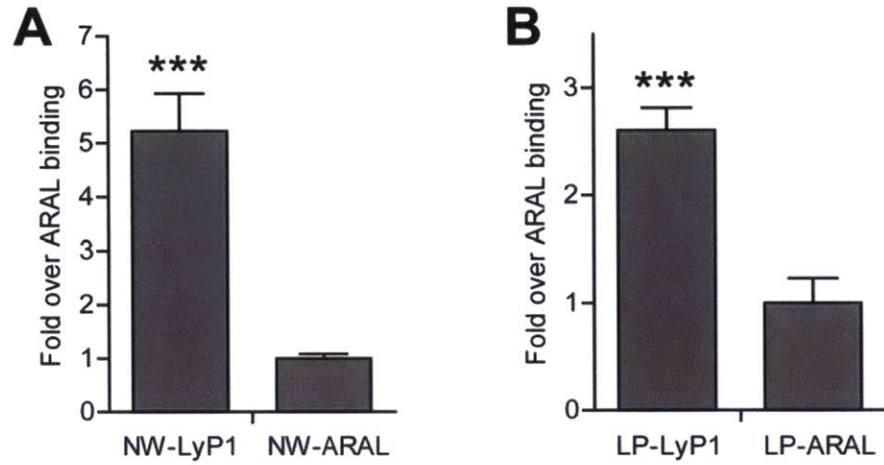


Figure 4.6. *In vitro* binding of NWs and LPs to recombinant p32. (A) Quantification of NW binding to p32 (***) $P < 0.005$, Student's *t*-test; $n = 3$, s.d.). (B) Quantification of LP binding to p32 (***) $P < 0.005$, Student's *t*-test; $n = 3$, s.d.).

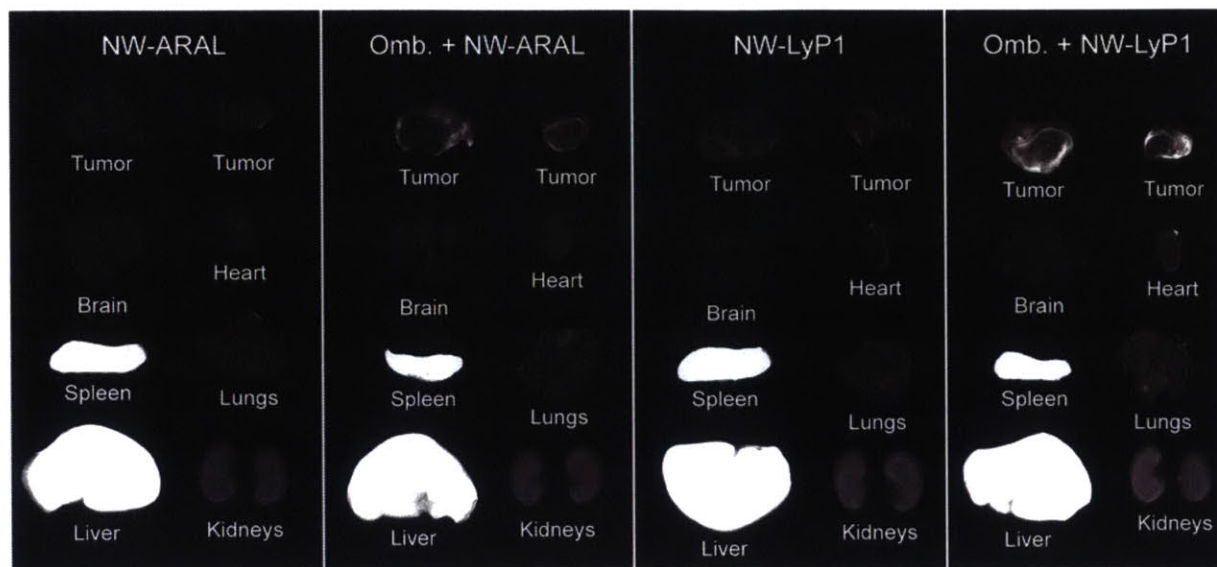


Figure 4.7. *In vivo* biodistribution of NWs. Near-infrared fluorescent scans of NW distribution in organs without (0 mg/kg) or with (60 mg/kg) ombrabulin (Omb.). Organs were excised and imaged at 24 hrs post-NW injection.

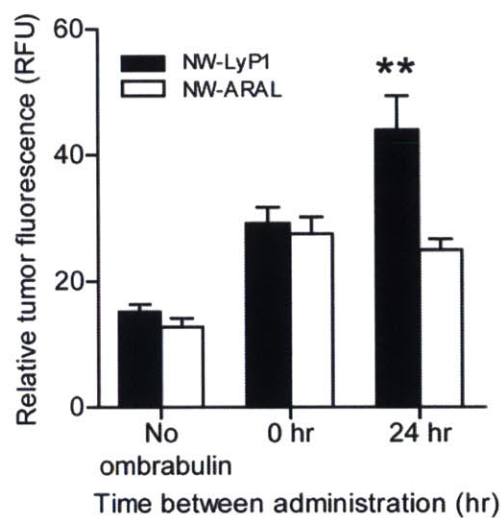


Figure 4.8. Effect of administration schedule on NW homing. Quantification of NW homing to tumors as a function of different times between ombrabulin (60 mg/kg) and NW administration (** $P < 0.01$, Student's t -test; $n = 3-4$ mice, s.e.).

of NW-LyP1. Collectively, these data show that pre-exposure to ombrabulin mediates the amplification of NW homing to tumors by increasing the amount of the target p32 protein available for binding.

Ombrabulin-induced amplification of therapeutic delivery. We next constructed model therapeutic nanoparticles, doxorubicin-loaded liposomes (LP), to test for amplified drug delivery to regions of ombrabulin-induced p32 presentation in tumors (**Figure 4.9A**). LPs were synthesized with either the targeting peptide LyP1 (LP-LyP1) or the control peptide ARAL (LP-ARAL) on the surface of particles and both populations were confirmed to exhibit a similar size range (hydrodynamic diameter ~160 nm) and equivalent circulation times (half-lives ~ 1.5 hrs; **Figure 4.10**).¹⁸⁴ To test for amplification of LP targeting to tumors, mice (n = 3 mice per condition) bearing bilateral MDA-MB-435 tumors were intravenously injected with either saline or ombrabulin (60 mg/kg), followed by LP-LyP1 or LP-ARAL (1 mg/kg by dox) after 24 hrs. At 24 hrs post-LP injection, we found that ombrabulin treatment amplified the delivery of LP-LyP1 and accumulation of doxorubicin in tumors by ~four-fold versus non-targeted LP-ARAL, ~2.5 fold relative to LP-LyP1 alone, and ~five-fold relative to non-cooperative and non-targeted LP-ARAL (***P* < 0.005 by Student's *t*-test; **Figure 4.9B**). Notably, without ombrabulin, LP-LyP1 also demonstrated higher accumulation of doxorubicin in tumors than LP-ARAL, which was consistent with previous studies using nanoparticles targeted by LyP1.³¹⁸⁻³²⁰ Similar to the NWs, histological examination of tumor sections again showed increased, localized staining of both LP-LyP1 (green) and p32 (red) in ombrabulin-treated tumors versus untreated tumors, while LP-ARAL (green) staining was sparsely distributed and did not localize to areas with p32 (red) in either scenario (**Figure 4.9C**). We also investigated the organ distribution of doxorubicin following cooperative targeting and found that administration of both ombrabulin and LP-LyP1

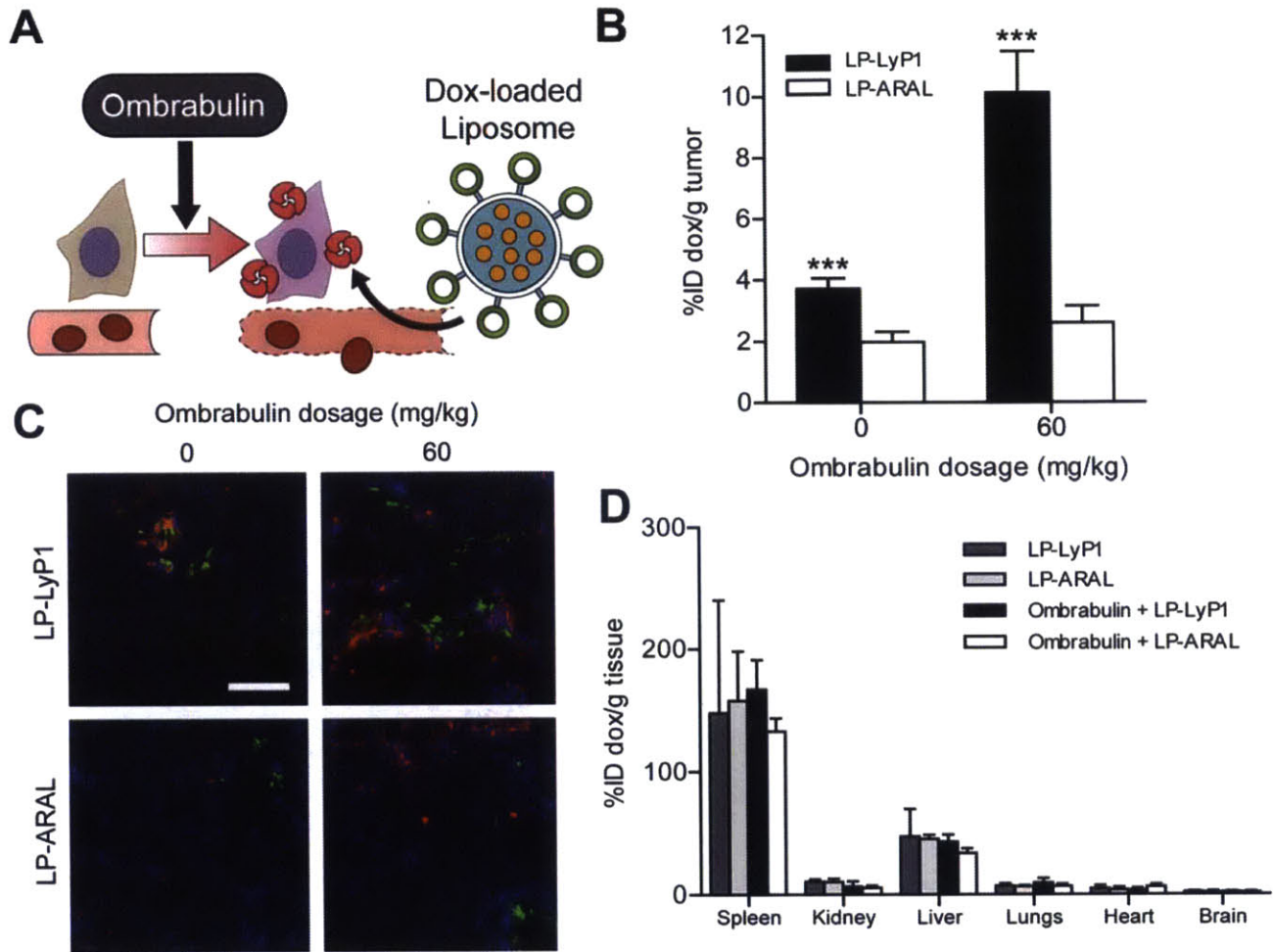


Figure 4.9. Ombrabulin mediated amplification of LP delivery. (A) Schematic of ombrabulin signaling to LPs. (B) Quantification of doxorubicin-loaded LP homing to tumors as a function of ombrabulin dosage (***) $P < 0.005$, Student's t-test; $n = 3$ mice, s.e.). (C) Immunofluorescent staining of LPs in tumors without (0 mg/kg) and with (60 mg/kg) ombrabulin (green = LP, red = p32 staining, blue = nuclear stain; scale bar = 100 μm). (D) Quantification of doxorubicin-loaded LP biodistribution in organs without (0 mg/kg) and with (60 mg/kg) ombrabulin (No significance, one-way ANOVA with Tukey post test; $n = 3-6$ mice, s.d.).

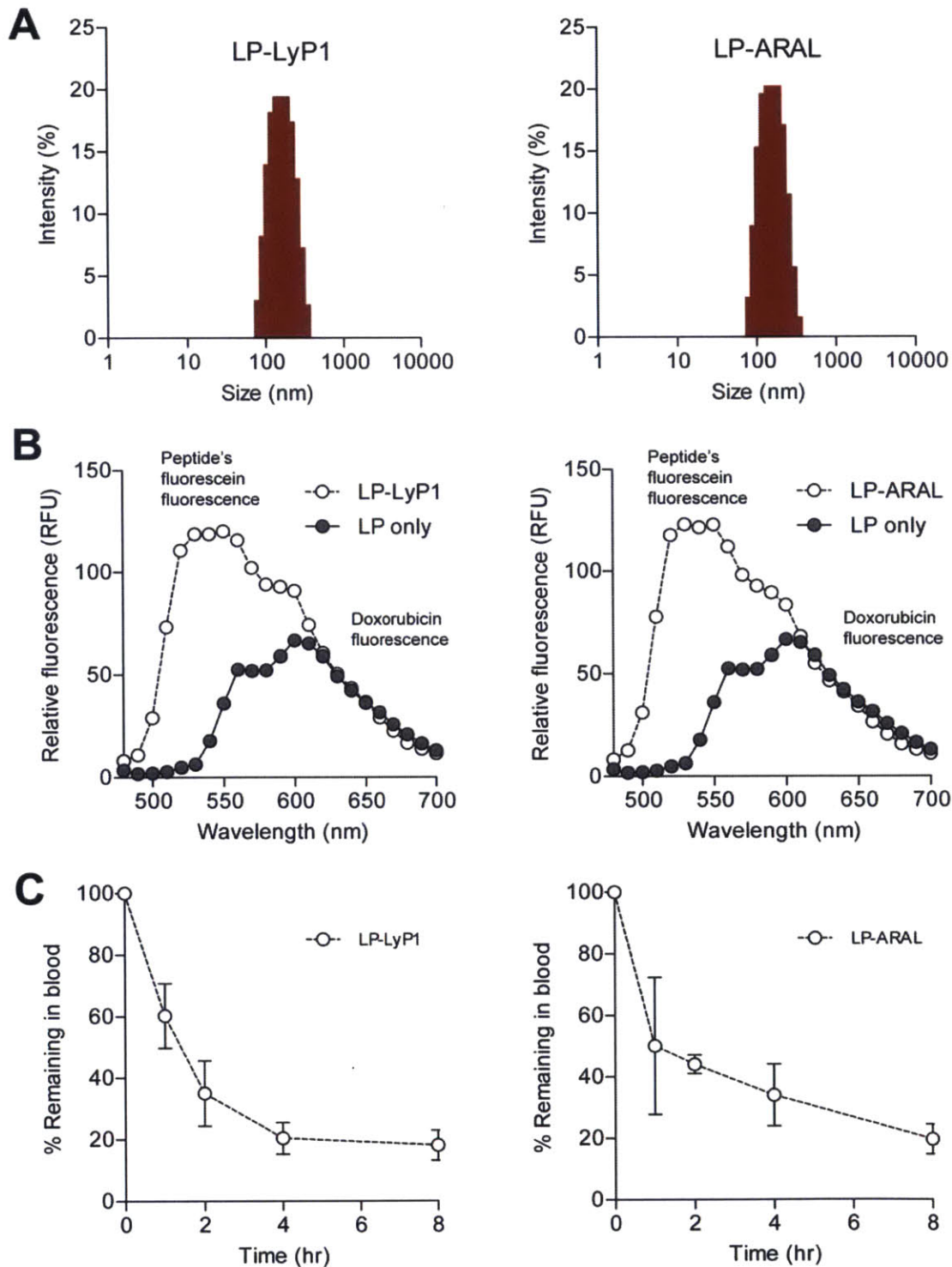


Figure 4.10. *In vitro* characterization of LPs. (A) Size distribution of doxorubicin-loaded LPs as determined by dynamic light scattering. (B) Fluorescence spectra of LPs conjugated with fluorescein-labeled peptides (excitation: 444 nm, emission: 480–700 nm, cutoff: 475 nm) and untargeted LPs (grey). (C) Circulation time of LPs as determined by doxorubicin fluorescence in the blood (n = 3 mice, s.d.).

or LP-ARAL did not change the biodistribution of doxorubicin, with a majority of the drug accumulating in the spleen and liver (**Figure 4.9D**). This result indicated that despite being administered systemically, ombrabulin does not lead to the increased accumulation of LPs in off-target sites and that the majority of particles are still cleared by the organs associated with the reticuloendothelial system, which is typical of systemically administered nanomaterials.²⁸⁴ Altogether, these experiments showed that pre-treatment with ombrabulin amplified the delivery of therapeutic nanoparticles that target the p32 protein.

Amplified tumor therapy with cooperative therapeutics. Finally, we evaluated the therapeutic efficacy of cooperative targeting in mice ($n = 7$ mice per condition) bearing single MDA-MB-435 human carcinoma tumors. Ombrabulin (60 mg/kg) or saline were injected into mice and 24 hrs later, an intravenous dose of LP-LyP1, LP-ARAL (2 mg/kg by dox), or saline was given. When this treatment regimen was administered every 4–5 days, we found that ombrabulin + LP-LyP1 was significantly more effective at slowing tumor growth ($*P < 0.05$ by two-way ANOVA with Bonferroni post test) than the treatments in isolation (ombrabulin, LP-LyP1, LP-ARAL) and non-cooperative controls (ombrabulin + LP-ARAL; **Figure 4.11A**, **Figure 4.12**) without any significant changes in animal weight following the last cycle of treatment (**Figure 4.11B**). In comparing the long term survival of mice in the various treatment groups, we found that ombrabulin + LP-LyP1 significantly prolonged the survival time of mice relative to all other treatments ($**P < 0.01$ by log rank test, $n = 7$ mice; **Figure 4.11C**). Collectively, these therapeutic studies demonstrated that the cooperativity of ombrabulin and targeted LPs led to decreased tumor growth and prolonged survival of mice.

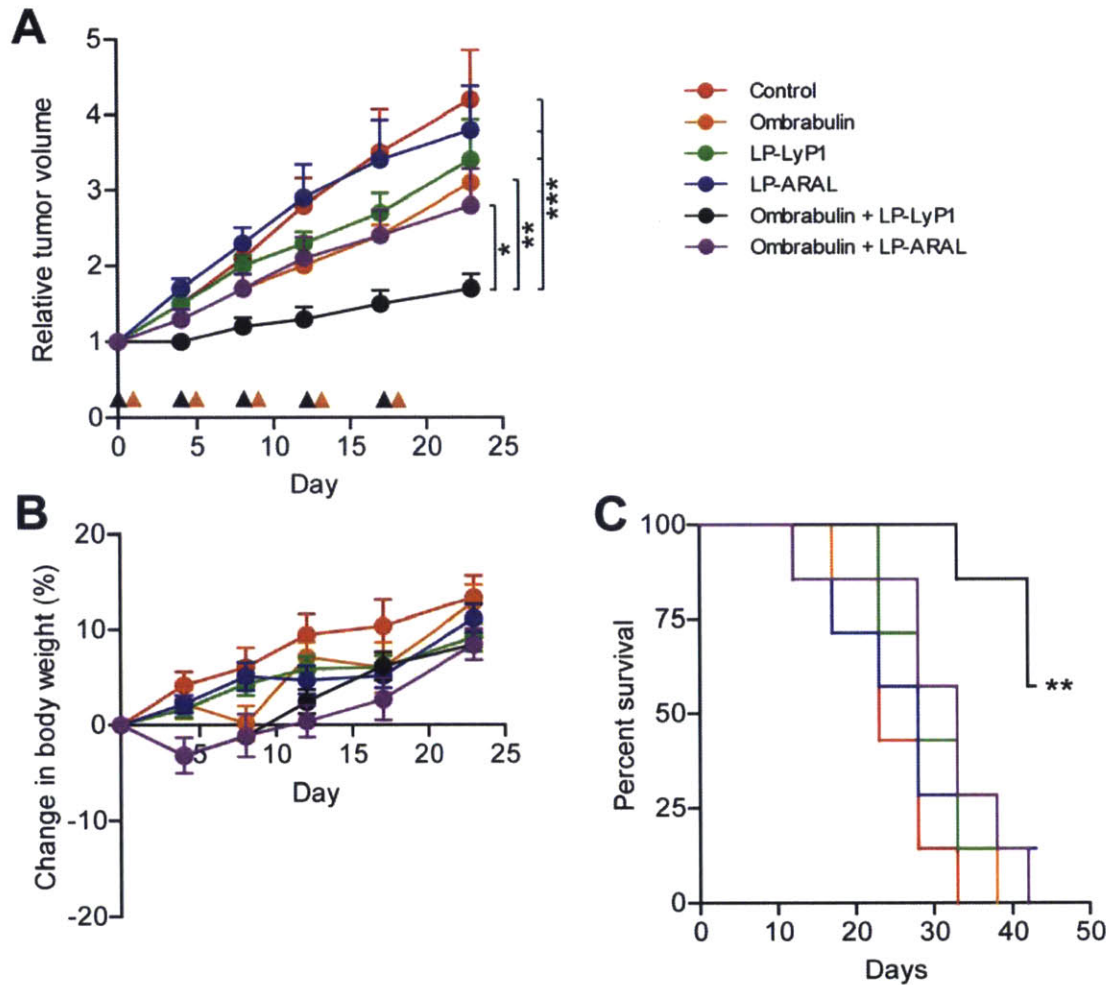


Figure 4.11. Therapeutic efficacy of cooperative targeting system. (A) Tumor volumes of different groups following three weeks of treatment. Black arrow head denotes time of ombrabulin (60 mg/kg) administration; orange arrow head denotes time of LP (1 mg/kg by dox) administration (* $P < 0.05$, ** $P < 0.01$, *** $P < 0.005$, two-way ANOVA with Bonferroni post test, $n = 7$ mice, s.e.). (B) Change in body weight of different groups following three weeks of treatment ($n = 7$ mice, s.e.). (C) Survival rate of different groups in the therapeutic efficacy study (** $P < 0.01$, log rank test; $n = 7$ mice).

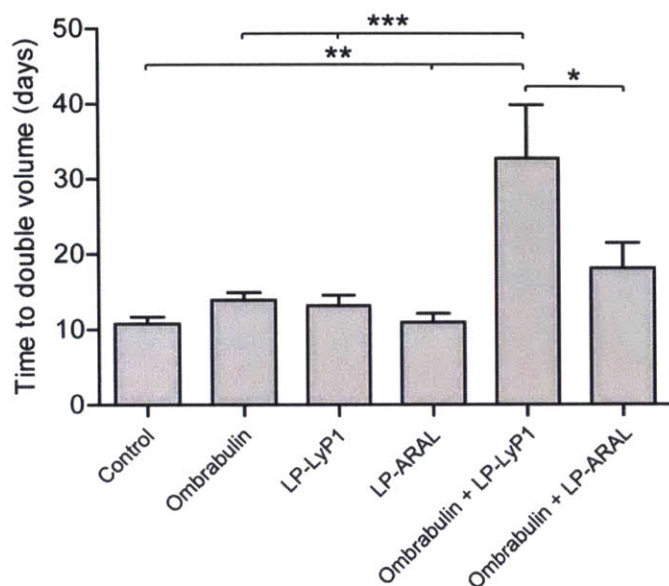


Table 1. Coefficient of determination

Treatment	Average R^2
Control	0.89
Ombrabulin	0.92
LP-LyP1	0.87
LP-ARAL	0.84
Ombrabulin + LP-LyP1	0.89
Ombrabulin + LP-ARAL	0.90

Figure 4.12. Tumor doubling time during therapeutic efficacy study. Calculated time to the doubling of tumor volume during the course of the therapeutic study (* $P < 0.05$, ** $P < 0.01$, *** $P < 0.005$, one-way ANOVA with Tukey post test; $n = 7$ mice, s.e.). Doubling time calculated by fitting tumor volumes to exponential growth curves. Table 1 shows the average coefficient of determination (R^2) of the curve fittings for each treatment group.

4.4 Discussion

In this study, we design a cooperative targeting system that harnesses the ombrabulin-induced increase in presentation of p32 to amplify the recruitment of targeted nanoparticles to tumors. Using small molecules or proteins to modulate the disease environment is advantageous because they do not face the same extravasation barrier as larger vehicles,³²¹ and may therefore effectively prime the tumor microenvironment for subsequent nanoparticle delivery. Numerous related strategies have aimed to enhance nanoparticle accumulation by increasing vascular permeability through the administration of vasoactive agents such as vascular endothelial growth factor, bradykinin, and tumor necrosis factor alpha.³²² However, a general concern with these approaches is that they may affect both healthy and diseased vasculature, thus escalating the risk of off-target effects. In contrast, our method leverages the specificity of ombrabulin for tumor vasculature, which is derived from the increased susceptibility of immature vessels to tubulin-binding agents,^{187, 309} and the tumor-specific expression of cell-surface p32 to bolster nanoparticle accumulation while simultaneously minimizing off-target delivery.¹⁸³ Compared to an earlier study using gold nanorod-mediated hyperthermia, administration of ombrabulin produced a larger increase in the magnitude of tumor p32 expression and a similar fold enhancement in nanoparticle homing to tumors.¹⁸⁴ However, unlike previous systems that utilize localized and guided treatment modalities such as hyperthermia^{182, 184} and radiation therapy³⁰⁴ to induce the presentation of novel binding sites, our strategy is fully autonomous with the potential to survey the entire body for disseminated disease without any *a priori* knowledge of tumor locations.

Vascular disrupting agents like ombrabulin are attractive inducing agents to use in this cooperative targeting system not only because of their antivasular activity against a broad range

of tumor types,^{314, 323} but because preclinical and clinical studies suggest that VDAs have the greatest impact when coupled with other treatments; as single agents, VDAs leave a viable tumor rim that can obtain nutrients and oxygen from neighboring healthy tissues and rapidly re-grow.^{187, 309, 315} Here, we demonstrated that pre-treatment of tumors with ombrabulin amplified the delivery of both prototypical diagnostic and therapeutic nanoparticles, highlighting the modularity of this stigmergic targeting approach. This data suggests that this system may be applicable to any number of cargos that are deliverable by nanoparticles, including other chemotherapies, siRNA, or diagnostic markers.^{1, 4, 324} Vascular disrupting agents and traditional chemotherapy have previously been coupled together in a single nanoparticle formulation and shown to be therapeutically effective, but these efforts did not incorporate any form of active targeting.¹⁴⁵ Our therapeutic study showed that cooperative targeting was not only more effective than either agent alone, but also was advantageous compared to the combination of ombrabulin and non-targeted doxorubicin LPs. These results also suggest that the staggered administration of a cooperative combination of drug and targeted nanoparticle may generate positive therapeutic indices by enhancing the delivery of cargos; previous studies have shown that up to 8 mg/kg of free doxorubicin are needed to demonstrate a therapeutic effect in the same human xenograft cancer model, however we observed a significant difference at just 2 mg/kg.³²⁵ Furthermore, recent studies have highlighted the importance of optimizing the dosing schedule for combination therapies involving VDAs given their range of temporal effects, with most recent results supporting the pretreatment of tumors with VDA prior to chemotherapy.^{206, 207} The protocol and results of our cooperative strategy were consistent with these findings, showing a greater enhancement in nanoparticle accumulation when they were administered 24 hrs after ombrabulin versus when they were co-administered.

4.5 Conclusion

Looking forward, several experimental avenues warrant further investigation in order to expand the applicability of cooperative nanoparticle targeting. In this study, we used a VDA to increase the number of nanoparticle binding sites within tumors, however the current arsenal of cancer treatments includes numerous other candidates with the potential to serve as inducing agents for cooperative targeting approaches. In addition to the aforementioned treatment modalities, traditional chemotherapies and next-generation targeted therapies have also been used to induce tumor antigens, which were identified by either gene expression profiling^{313, 326} or *in vivo* phage display.^{311, 312} Future studies may focus on developing systematic screening approaches to identify novel induced antigens in response to panels of drugs spanning multiple classes. These antigens could then be cross-referenced to known libraries of targeting ligands from the literature or used to develop new ligands in order to create more potential pairings of cooperative drugs and ligand-decorated nanoparticles. In summary, this work introduces a new approach for designing nanoparticle targeting systems that leverages drug-induced modulation of the disease environment to improve the detection and treatment of cancer.

4.6 Materials and Methods

Generation of MDA-MB-435 xenografts. MDA-MB-435 cancer cell lines (American Type Culture Collection) were cultured in Dulbecco's Modified Eagle Medium (DMEM) with 10% fetal bovine serum, penicillin, and streptomycin. To generate subcutaneous xenograft models, 4-6 week old female NCr nude mice (Taconic) were injected either laterally or bilaterally in the hind flanks, according to the experimental design, with $\sim 2 \times 10^6$ MDA-MB-435 cells suspended in 200 μ L DMEM.

Histological analysis. Ombrabulin was kindly provided by Sanofi Aventis. Mice bearing bilateral flank MDA-MB-435 xenografts ($n = 3$ mice) were intravenously administered different dosages of ombrabulin (0, 30, 60 mg/kg) in 0.9% NaCl without anesthesia. At different time points (4, 24 hrs p.i.) the mice were euthanized and their tumors were excised. For hematoxylin and eosin staining, tumors were fixed in 4% paraformaldehyde for 1-2 hours at RT and stored in 70% ethanol until paraffin-embedding, sectioning, and staining (Koch Institute Histology Core). For immunofluorescent staining, representative frozen tumor sections were stained for p32 (Millipore) and Hoechst (Invitrogen) before analysis by fluorescence microscopy (Nikon Eclipse Ti). The percentage of p32 positive staining in the tumor was quantified using MATLAB (MathWorks).

Flow cytometry. Ombrabulin (0, 30, or 60 mg/kg) was administered intravenously to mice bearing bilateral flank MDA-MB-435 xenografts. At different time points (4 or 24 hrs post-injection), the mice were euthanized and their tumors were excised in their entirety. The tumors were gently dissociated into single cell suspensions using a MACS human Tumor Dissociation

Kit (Miltenyi Biotec) according to manufacturer instructions. 2.5×10^6 cells per condition were incubated for 1 hr on ice with both Alexa Fluor-488-conjugated mouse anti-human HLA-AB (BD Pharmingen) and either rabbit polyclonal anti-p32 (Millipore) or rabbit IgG isotype control (R&D Systems). Cells were then washed twice with cold PBS supplemented with 2% fetal bovine serum (FBS), followed by incubation for 1 hr on ice with Alexa Fluor-594 goat anti-rabbit secondary antibody (Invitrogen). Cells were washed and then resuspended in PBS plus 2% FBS for analysis. For quantification of surface p32 levels, human tumor cells were isolated by gating out all HLA-ABC-negative cells.

Peptide nanoworm synthesis. Aminated iron oxide NWs were synthesized according to previously published protocols.²³⁴ Peptides (LyP1 = C-(K-Flsc)-C6-CGDKRTRGC, Cys2 & Cys3 bridge; ARAL = C-(K-Flsc)-C6-ARALPSQRSR; Flsc = fluorescein, C6 = 6-aminohexanoic acid linker) were synthesized by CPC Scientific and the Tufts University Core Facility peptide synthesis service. To conjugate peptides to NWs, NWs were first reacted with NHS-VivoTag 750 (VT750, PerkinElmer) and MAL-PEG(5k)-SVA (Laysan Bio.) to introduce sulfhydryl-reactive handles. Cysteine terminated peptides were then mixed with NWs (95:1 molar ratio) for one hour at room temperature (RT) and purified using a Sephadex G-25 gel filtration column (GE Healthcare). Stock solutions were stored in PBS at 4°C. The number of fluorescein-labeled peptides per NWs was determined by absorbance spectroscopy using the absorbance of fluorescein (490 nm) and its extinction coefficient ($78,000 \text{ cm}^{-1}\text{M}^{-1}$). The particle size was measured by dynamic light scattering (Malverin Zetasizer Nano Series).

Doxorubicin-loaded liposome synthesis. Hydrogenated soy sn-glycero-3-phosphocholine (HSPC), cholesterol, and 1,2-distearoyl-snglycero-3-phosphoethanolamine-N-polyethylene glycol 2000 [DSPE-PEG(2k)] were purchased from Avanti Polar Lipids. DSPE-[Maleimide(Polyethylene Glycol 5000)] [DSPE-PEG(5K)-MAL was purchase from Nanocs, Inc. Doxorubicin was purchased from Sigma Chemical Co. For peptide conjugation, DSPE-PEG(5K)-MAL was reacted with Cysteine-terminated peptides (LyP1 or ARAL) in 50 mM triethylamine, DMF for 24 hours and exchanged into water using gel filtration. Liposomes were prepared from HSPC, cholesterol, and either DSPE-PEG(5K)-LyP1 or DSPE-PEG(5K)-ARAL in the molar ratio of 75:50:3 by lipid film hydration and membrane (100 nm) extrusion method.³²⁷ Encapsulation of doxorubicin (dox) into the liposomes was then carried out using the pH gradient-driven loading protocol.³²⁸ Free doxorubicin was removed by gel filtration on Sephadex G-25. The peptide-conjugated doxorubicin liposomes were stored in PBS at 4 °C before use. The particle size was measured by dynamic light scattering (Malverin Zetasizer Nano Series) and the fluorescence intensity was measured by microplate reader (SpectroMax Gemini EM, Molecular Devices).

NW circulation times. Healthy female Swiss Webster mice (3–4 months, n = 3 mice) were injected via tail vein with either NW-LyP1 or NW-ARAL (1 nmol by VT750) formulated with 1x PBS. For measurement of NW fluorescence, blood samples were collected through retro-orbital blood draw and scanned on the LI-COR Odyssey Infrared Imaging System. Fluorescence in each sample was quantified using ImageJ software (NIH).

LP circulation times. Healthy female Swiss Webster mice (3–4 months, n = 3 mice) were injected via tail vein with either LP-LyP1 or LP-ARAL (1 mg/kg by dox) formulated with 1x PBS. For measurement of doxorubicin fluorescence, blood samples were collected through retro-orbital blood draw and centrifuged at 2900g for 5 minutes to isolate plasma. Next, 20 μ L of plasma was mixed with 80 μ L of 70% EtOH, 0.3 N HCl, which was then analyzed by fluorimetry using a fluorescence microplate reader (SpectroMax Gemini EM, Molecular Devices) at excitation/emission wavelengths of 470/590 nm.

In vitro binding assay. The *in vitro* binding of nanoparticles to p32 was assessed using a magnetic bead assay. Briefly, NWs (40 pmol by Flsc) or LPs (1.5 pmol by Flsc) were incubated with Ni-NTA magnetic agarose beads (Qiagen) coated with His-tagged recombinant p32 protein (kindly provided by Dr. T. Teesalu) in binding and washing buffer (BWB; PBS with 300 mM NaCl, 5 mM imidazole, 0.05% NP-40, 0.1% bovine serum albumin) for 1 hr at room temperature, washed four times with BWB, and eluted with 400 mM imidazole in BWB. Samples were quantified by fluorescence microplate reader (SpectroMax Gemini EM, Molecular Devices) at excitation/emission wavelengths of 485/538 nm and compared to standard curves.

Nanoworm homing to tumors. Mice bearing bilateral flank MDA-MB-435 xenografts (n = 3–4 mice) were intravenously administered different dosages of ombrabulin (0, 30, 60 mg/kg). NW-LyP1 or NW-ARAL (1 nmol by VT750) were either co-administered or injected 24 hrs following ombrabulin administration. At 24 hrs post-NW administration, organs were removed and scanned on the LI-COR Odyssey Infrared Imaging System. Fluorescence in each organ was quantified using ImageJ software (NIH). To analyze tumors by immunostaining, representative

sections were stained for NWs (anti-Flsc primary, GeneTex), either p32 (Millipore) or CD31 (BD Pharmingen), and Hoechst (Invitrogen) before analysis by fluorescence microscopy (Nikon Eclipse Ti).

Quantification of doxorubicin in tissues. Mice bearing bilateral flank MDA-MB-435 xenografts (n = 3 mice) were intravenously administered different dosages of ombrabulin (0, 60 mg/kg), followed by either LP-LyP1 or LP-ARAL (1 mg/kg by dox) 24 hours later. At 24 hrs post-LP administration, organs were removed, weighed, incubated with 500 μ l of 70% EtOH, 0.3 N HCl, and homogenized (Tissue Tearor, Biospec Products) to release doxorubicin from tissues. Following homogenization, another 1 ml of 70% EtOH, 0.3 N HCl, was added to samples and they were centrifuged. Supernatants of samples were analyzed for doxorubicin fluorescence using a fluorescence microplate reader (SpectroMax Gemini EM, Molecular Devices) at excitation/emission wavelengths of 470/590 nm and compared to standard curves. To analyze tumors by immunostaining, representative sections were stained for LPs (anti-Flsc primary, GeneTex), p32 (Millipore), and Hoechst (Invitrogen) before analysis by fluorescence microscopy (Nikon Eclipse Ti).

Therapeutic assessment of cooperative targeting systems. Treatment of mice commenced fourteen days after subcutaneous injection of MDA-MB-435 cancer cells. Tumor dimensions were measured with calipers and the volume was calculated using the modified ellipsoid formula (volume = $1/2 \times \text{length} \times \text{width}^2$), where L and W refer to the larger and smaller perpendicular dimensions collected at each measurement.³²⁹ Mice bearing single lateral xenografts were randomized into groups of seven mice such that the mean tumor volumes were similar between

groups. Mice were first administered different dosages of ombrabulin (0, 60 mg/kg). At 24 hrs post-injection, mice were administered LP-LyP1 (2 mg/kg), LP-ARAL (2 mg/kg), or saline. This treatment regimen was repeated every 4-5 days. At regular intervals after treatment, tumors were measured and mice were weighed. For the survival curve study, mice were sacrificed when tumors exceeded 500 mm³. To compute the volumetric doubling time of tumors, each tumor volume trace was fit to an exponential growth curve in Excel (Microsoft) and the doubling time was calculated from the growth constant.³³⁰

Statistical analyses. Student's *t*-test, one- and two-way ANOVA, and survival curve analyses were calculated with GraphPad 5.0 (Prism).

All experimental protocols involving animals were approved by the MIT Committee on Animal Care (protocol #0411-036-14).

4.7 Acknowledgements

Dr. Ester Kwon and Justin Lo were co-authors on this work. We thank Joerg Adamczewski, Hichem Chakroun, Patricia Vrignaud, and Chantal Carrez from Sanofi-Aventis for generously providing us with ombrabulin and experimental guidance. We thank Dr. Tambet Teesalu for providing us with recombinant p32. We thank the Koch Institute Swanson Biotechnology Center (MIT) for assistance with tissue sectioning, specifically Michael Brown and Kathleen Cormier from the Histology core. We thank Dr. Heather Fleming (MIT) for critical readings of the manuscript. This work was supported by the NIH (BRP: R01CA124427-01), NIH/NCI (U54CA119349, U54CA119335, and the Alliance Challenge Project/MIT-Harvard

Center of Cancer Nanotechnology Excellence: U54CA151884), Packard Fellowship (1999-1453), and Marie-D. & Pierre Casimir-Lambert Fund. This work was supported in part by the Koch Institute Support (core) Grant P30-CA14051 from the National Cancer Institute. K.Y.L. acknowledges support from CCNE (5 U54 CA151884-03). J.H.L. acknowledges support from NIH MSTP program (T32GM007753). Dr. E.J.K. acknowledges support from the Ruth L. Kirschstein National Research Service Award (1F32CA177094-01). Dr. S.N.B is an HHMI Investigator.

Chapter 5: Perspectives and Future Directions

5.1 Nanoparticles that Sense Coagulation Activity *In Vivo*

In Chapter 2, we extended the synthetic urinary biomarker platform elaborated by Kwong *et al* to the detection of thrombin activity *in vivo*.^{38,293} This system exploits the anatomy of the kidney to filter and concentrate reporters in order to generate an amplified urinary signal that can be detected noninvasively. While the work focused on synthetic biomarkers composed of peptide reporters conjugated to an iron oxide nanoworm, the platform is generalizable to many nanomaterial scaffolds that exceed the renal excretion limit. Other scaffold materials may have the potential to extend circulation half-life, improve penetration into disease sites, simplify probe synthesis, and reduce cost. FDA-approved materials that are currently being investigated include albumin, dextran, and PEG.

Engineering reporters with high specificity for target proteases is critical for both research and clinical applications. The presence of a detectable urinary signal in the absence of disease processes may be attributable to basal level thrombin activity or non-specific background cleavage by other endogenous proteases. Regardless, the engineering of more specific substrates, either through rational design or screening methods, will be an important focus in the future.^{257, 331, 332} Much effort has also been directed towards engineering rapid, inexpensive detection methods that may enable new diagnostic applications, particularly in developing nations. Towards this end, a paper-based assay, similar to a home pregnancy test, for detecting urinary reporters was recently developed, which may enable low-cost diagnosis of diseases associated with thrombosis at the point of care in resource-limited settings.²⁵⁶

The ability to non-invasively monitor protease activity *in vivo* has a number of research applications in the study of coagulation. The kinetics of the coagulation cascade have been

interrogated extensively *in vitro*, however the extent to which these models predict *in vivo* processes that are affected by a multitude of additional factors (e.g. blood flow, vessel anatomy, endothelium) is unclear.^{12, 13, 333} To date, real-time monitoring of coagulation reactions *in vivo* has been limited by a lack of quantitative tools and easily measurable markers.²³¹ Our synthetic biomarker platform can be readily extended to measure the activity of all coagulation factors that are serine proteases (thrombin, FVII, FIX, FX, FXI, FXII) in a facile, multiplexed fashion. Such a technology has the potential to expand our understanding of thrombosis as it occurs *in vivo* and lead to new targets for antithrombotic therapy.

5.2 Nanoparticles that Regulate Biological Processes *In Vivo*

The work in Chapter 3 presents a self-titrating nanocomplex formulation of the clinical anticoagulant, unfractionated heparin (UFH), which prevents thrombosis without increasing bleeding. These nanoSTATs form a negative feedback loop with thrombin, the important mediator of fibrin deposition, effectively restoring homeostatic regulation of the coagulation cascade. In order to bridge the gap towards clinical translation, the current nanoSTAT formulation must be optimized in several ways. Though the short circulation half-life is attractive for patients at high risk for bleeding or undergoing invasive procedures, extended plasma presence may reduce the required dosage and the need for continuous infusion in a prophylactic setting. Potential strategies for extending the circulation time include optimization of the cationic peptide sequence, incorporating a higher density of shielding polymer, or attachment to a long-circulating drug carrier.³³⁴⁻³³⁶ In addition, alternate routes of administration, such as subcutaneous delivery, should be investigated as it would also widen the scope of clinical applicability for this technology.

One of the frequently cited limitations of heparins is their propensity to cause heparin-induced thrombocytopenia (HIT), an immune reaction that could actually lead to the formation of thrombosis.⁴¹ HIT occurs when the body forms antibodies against complexes of heparin and platelet factor 4 (PF4).²⁹⁷ UFH has also long been known to bind to and induce morphological changes in platelets, resulting in nonimmune activation.³³⁷ By sequestering UFH in a nanocomplex, nanoSTATs have the theoretical potential to limit adverse interactions with platelets (as well as other cells and proteins) and reduce the incidence of HIT. Further studies are needed to probe the effects of nanoSTATs on platelet activation.

Considering the complexity of the coordinated reaction networks, biological cross-talk, and feedback loops that govern haemostasis, it comes as little surprise that the current clinical anticoagulants, which are designed to completely shut down one or more pathways within the cascade, struggle to balance the risks of thrombosis and bleeding. A self-regulating system that titrates drug release based on feedback from the external environment would appear to be an optimal solution for the treatment and prevention of thrombosis.^{91, 271} Further investigations may seek to generalize the thrombin-sensitive mechanism or analogous approaches to other anticoagulants. The new generation of orally-available thrombin and FXa inhibitors could greatly benefit from a self-titrating delivery since they are used long-term and do not currently have clinical antidotes.

Designing self-regulating drug delivery systems is a challenging endeavor that requires a well-defined understanding of the biology underlying the pathways and processes being targeted, and a method of actuating drug release must then be engineered into a nanoscale delivery vehicle. As such, these systems have been studied in a relatively narrow set of applications, with the most prominent being glucose-sensitive insulin release for treatment of diabetes.^{6, 338}

However, there exist numerous other biological processes that are critical to life, yet lead to pathological states when their endogenous regulatory mechanisms fail, which may benefit from self-regulating pharmacological agents. Beyond the regulation of coagulation and glucose, autoimmune diseases and chronic inflammation may be interesting conditions for further exploration.

5.3 Drug-Induced Amplification of Nanoparticle Targeting *In Vivo*

In Chapter 4, we demonstrate how two synthetic entities, a small molecule vascular disrupting agent (VDA) and targeted nanoparticles, can cooperate through modulation of the tumor microenvironment to amplify delivery. Once in the bloodstream, the two components perform their programmed tasks autonomously without the need for further external inputs, which is a significant advancement over previous cooperative nanosystems.^{182, 184} These system shows how one might utilize external agents to manipulate and hijack internal biological processes to perform tasks that they were not evolutionarily programmed to perform. While this embodiment leverages VDA-induced stress to increase the presentation of a targetable receptor, the concept of drug-induced amplification is most likely extensible to many other combinations of drugs and targeted nanoparticles that cooperate through other biological pathways. Indeed, several other drug-induced antigens have been identified and utilized for monitoring of therapeutic response and targeted therapy.³¹¹⁻³¹³

Future studies may focus on determining new schemes for amplifying the delivery of targeted nanoparticles to sites of disease. High-throughput screening technologies may enable rapid analysis of cellular responses to panels of clinically-approved drugs, with a particular emphasis on identifying inducible and targetable receptors on the surface of cancer cells (**Figure 5.1**). Another approach might be to rationally design a system by harnessing other endogenous

amplification cycles other than coagulation, such as inflammation or complement activation.

These processes are well-studied with many known activators that can be programmed for use in a bio-nanosystem (e.g. tumor necrosis factor alpha for inflammation, bacterial polysaccharides for complement).^{339, 340} Much like coagulation, activation of both these biological responses must be tightly-regulated *in vivo*, as loss of control has the potential to cause catastrophic damage to host tissues. The ability of nanomaterials to impact inflammation and complement activation is already being studied for a number of clinical applications.³⁴¹⁻³⁴³

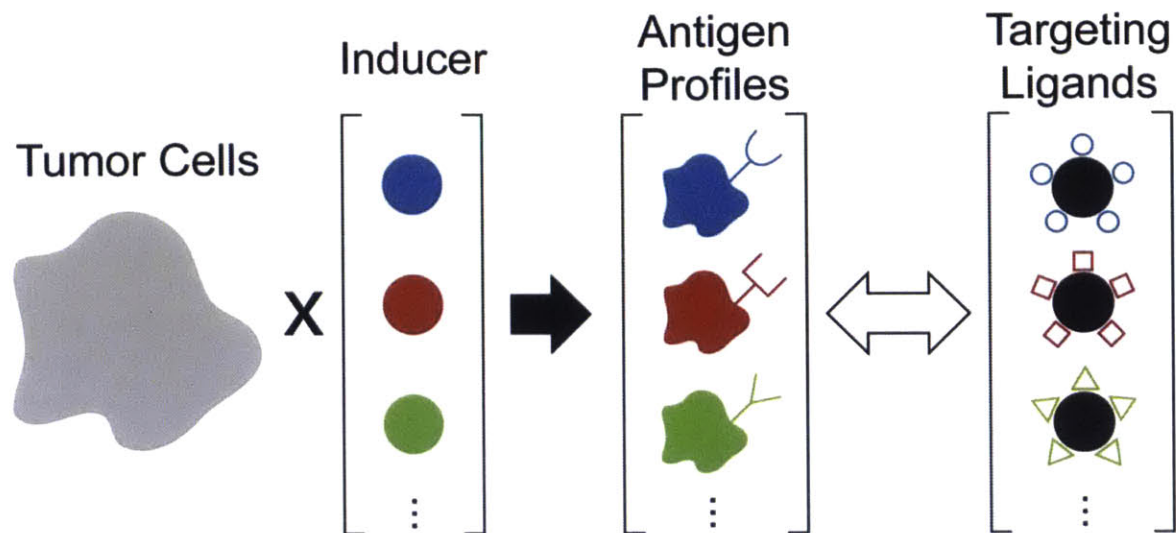


Figure 5.1. Schematic of a screening approach for identifying drug-induced cell surface antigens and matching targeting ligands.

References

1. Ferrari, M. Cancer Nanotechnology: Opportunities and Challenges. *Nat. Rev. Cancer* **2005**, *5*, 161-171.
2. Peer, D.; Karp, J. M.; Hong, S.; Farokhzad, O. C.; Margalit, R.; Langer, R. Nanocarriers as an Emerging Platform for Cancer Therapy. *Nat. Nanotechnol.* **2007**, *2*, 751-760.
3. Davis, M. E.; Chen, Z.; Shin, D. M. Nanoparticle Therapeutics: An Emerging Treatment Modality for Cancer. *Nat. Rev. Drug Discov.* **2008**, *7*, 771-782.
4. Petros, R. A.; DeSimone, J. M. Strategies in the Design of Nanoparticles for Therapeutic Applications. *Nat. Rev. Drug Discov.* **2010**, *9*, 615-627.
5. Kim, B. Y. S.; Rutka, J. T.; Chan, W. C. W. Nanomedicine. *N. Engl. J. Med.* **2010**, *363*, 2434-2443.
6. Mura, S.; Nicolas, J.; Couvreur, P. Stimuli-Responsive Nanocarriers for Drug Delivery. *Nat. Mater.* **2013**, *12*, 991-1003.
7. Ganta, S.; Devalapally, H.; Shahiwala, A.; Amiji, M. A Review of Stimuli-Responsive Nanocarriers for Drug and Gene Delivery. *J. Control. Release* **2008**, *126*, 187-204.
8. LaVan, D. A.; McGuire, T.; Langer, R. Small-Scale Systems for in Vivo Drug Delivery. *Nat. Biotechnol.* **2003**, *21*, 1184-1191.
9. Mackman, N. Triggers, Targets and Treatments for Thrombosis. *Nature* **2008**, *451*, 914-918.
10. Furie, B.; Furie, B. C. Mechanisms of Thrombus Formation. *N. Engl. J. Med.* **2008**, *359*, 938-949.
11. Engelmann, B.; Massberg, S. Thrombosis as an Intravascular Effector of Innate Immunity. *Nat. Rev. Immunol.* **2013**, *13*, 34-45.
12. Mann, K. G.; Butenas, S.; Brummel, K. The Dynamics of Thrombin Formation. *Arterioscler. Thromb. Vasc. Biol.* **2003**, *23*, 17-25.
13. Mann, K. G. Thrombin Formation. *Chest* **2003**, *124*, 4S-10S.
14. Jackson, S. P. Arterial Thrombosis--Insidious, Unpredictable and Deadly. *Nat. Med.* **2011**, *17*, 1423-36.
15. Mackman, N. New Insights into the Mechanisms of Venous Thrombosis. *J. Clin. Invest.* **2012**, *122*, 2331-2336.
16. Hirsh, J.; Lee, A. Y. Y. How We Diagnose and Treat Deep Vein Thrombosis. *Blood* **2002**, *99*, 3102-3110.
17. Grant, B. J. Diagnosis of Suspected Deep Vein Thrombosis of the Lower Extremity. (accessed March 18).
18. Piazza, G.; Goldhaber, S. Z. Acute Pulmonary Embolism: Part I: Epidemiology and Diagnosis. *Circulation* **2006**, *114*, e28-e32.
19. Thompson, T. B.; Hales, C. A. Diagnosis of Acute Pulmonary Embolism. (accessed March 18).
20. Investigators, P. Value of the Ventilation/Perfusion Scan in Acute Pulmonary Embolism. Results of the Prospective Investigation of Pulmonary Embolism Diagnosis (Pioped). *JAMA* **1990**, *263*, 2753-9.
21. Jaffer, F. A.; Libby, P.; Weissleder, R. Molecular Imaging of Cardiovascular Disease. *Circulation* **2007**, *116*, 1052-1061.

22. Jaffer, F. A.; Tung, C.-H.; Gerszten, R. E.; Weissleder, R. In Vivo Imaging of Thrombin Activity in Experimental Thrombi with Thrombin-Sensitive near-Infrared Molecular Probe. *Arterioscler. Thromb. Vasc. Biol.* **2002**, *22*, 1929-1935.
23. Tung, C.-H.; Gerszten, R. E.; Jaffer, F. A.; Weissleder, R. A Novel near-Infrared Fluorescence Sensor for Detection of Thrombin Activation in Blood. *Chembiochem* **2002**, *3*, 207-211.
24. Robinson, B. R.; Houg, A. K.; Reed, G. L. Catalytic Life of Activated Factor Xiii in Thrombi: Implications for Fibrinolytic Resistance and Thrombus Aging. *Circulation* **2000**, *102*, 1151-1157.
25. Luker, G. D.; Luker, K. E. Optical Imaging: Current Applications and Future Directions. *J. Nucl. Med.* **2008**, *49*, 1-4.
26. Botnar, R. M.; Buecker, A.; Wiethoff, A. J.; Parsons, E. C.; Katoh, M.; Katsimaglis, G.; Weisskoff, R. M.; Lauffer, R. B.; Graham, P. B.; Gunther, R. W.; et al. In Vivo Magnetic Resonance Imaging of Coronary Thrombosis Using a Fibrin-Binding Molecular Magnetic Resonance Contrast Agent. *Circulation* **2004**, *110*, 1463-1466.
27. Botnar, R. M.; Perez, A. S.; Witte, S.; Wiethoff, A. J.; Laredo, J.; Hamilton, J.; Quist, W.; Parsons, E. C.; Vaidya, A.; Kolodziej, A.; et al. In Vivo Molecular Imaging of Acute and Subacute Thrombosis Using a Fibrin-Binding Magnetic Resonance Imaging Contrast Agent. *Circulation* **2004**, *109*, 2023-2029.
28. Spuentrup, E.; Buecker, A.; Katoh, M.; Wiethoff, A. J.; Parsons, E. C.; Botnar, R. M.; Weisskoff, R. M.; Graham, P. B.; Manning, W. J.; Günther, R. W. Molecular Magnetic Resonance Imaging of Coronary Thrombosis and Pulmonary Emboli with a Novel Fibrin-Targeted Contrast Agent. *Circulation* **2005**, *111*, 1377-1382.
29. Spuentrup, E.; Fausten, B.; Kinzel, S.; Wiethoff, A. J.; Botnar, R. M.; Graham, P. B.; Haller, S.; Katoh, M.; Parsons, E. C.; Manning, W. J.; et al. Molecular Magnetic Resonance Imaging of Atrial Clots in a Swine Model. *Circulation* **2005**, *112*, 396-399.
30. Overoye-Chan, K.; Koerner, S.; Looby, R. J.; Kolodziej, A. F.; Zech, S. G.; Deng, Q.; Chasse, J. M.; McMurry, T. J.; Caravan, P. Ep-2104r: A Fibrin-Specific Gadolinium-Based Mri Contrast Agent for Detection of Thrombus. *J. Am. Chem. Soc.* **2008**, *130*, 6025-6039.
31. Yu, X.; Song, S.-K.; Chen, J.; Scott, M. J.; Fuhrhop, R. J.; Hall, C. S.; Gaffney, P. J.; Wickline, S. A.; Lanza, G. M. High-Resolution Mri Characterization of Human Thrombus Using a Novel Fibrin-Targeted Paramagnetic Nanoparticle Contrast Agent. *Magn. Reson. Med.* **2000**, *44*, 867-872.
32. Winter, P. M.; Caruthers, S. D.; Yu, X.; Song, S.-K.; Chen, J.; Miller, B.; Bulte, J. W. M.; Robertson, J. D.; Gaffney, P. J.; Wickline, S. A.; et al. Improved Molecular Imaging Contrast Agent for Detection of Human Thrombus. *Magn. Reson. Med.* **2003**, *50*, 411-416.
33. Winter, P. M.; Shukla, H. P.; Caruthers, S. D.; Scott, M. J.; Fuhrhop, R. W.; Robertson, J. D.; Gaffney, P. J.; Wickline, S. A.; Lanza, G. M. Molecular Imaging of Human Thrombus with Computed Tomography. *Acad. Radiol.* **2005**, *12*, S9-S13.
34. Hamilton, A.; Huang, S.-L.; Warnick, D.; Stein, A.; Rabbat, M.; Madhav, T.; Kane, B.; Nagaraj, A.; Klegerman, M.; MacDonald, R.; et al. Left Ventricular Thrombus Enhancement after Intravenous Injection of Echogenic Immunoliposomes: Studies in a New Experimental Model. *Circulation* **2002**, *105*, 2772-2778.
35. Tung, C.-H.; Ho, N.-H.; Zeng, Q.; Tang, Y.; Jaffer, F. A.; Reed, G. L.; Weissleder, R. Novel Factor Xiii Probes for Blood Coagulation Imaging. *Chembiochem* **2003**, *4*, 897-899.

36. McCarthy, J. R.; Patel, P.; Botnaru, I.; Haghayeghi, P.; Weissleder, R.; Jaffer, F. A. Multimodal Nanoagents for the Detection of Intravascular Thrombi. *Bioconjug. Chem.* **2009**, *20*, 1251-1255.
37. Hara, T.; Bhayana, B.; Thompson, B.; Kessinger, C. W.; Khatri, A.; McCarthy, J. R.; Weissleder, R.; Lin, C. P.; Tearney, G. J.; Jaffer, F. A. Molecular Imaging of Fibrin Deposition in Deep Vein Thrombosis Using Fibrin-Targeted near-Infrared Fluorescence. *JACC Cardiovasc. Imaging* **2012**, *5*, 607-15.
38. Kwong, G. A.; von Maltzahn, G.; Murugappan, G.; Abudayyeh, O.; Mo, S.; Papayannopoulos, I. A.; Sverdllov, D. Y.; Liu, S. B.; Warren, A. D.; Popov, Y.; et al. Mass-Encoded Synthetic Biomarkers for Multiplexed Urinary Monitoring of Disease. *Nat. Biotechnol.* **2013**, *31*, 63-70.
39. McLean, J. The Thromboplastic Action of Cephalin. *Am. J. Physiol.* **1916**, *41*, 250-257.
40. Crowther, M. A.; Warkentin, T. E. Bleeding Risk and the Management of Bleeding Complications in Patients Undergoing Anticoagulant Therapy: Focus on New Anticoagulant Agents. *Blood* **2008**, *111*, 4871-9.
41. Hirsh, J.; Warkentin, T. E.; Shaughnessy, S. G.; Anand, S. S.; Halperin, J. L.; Raschke, R.; Granger, C.; Ohman, E. M.; Dalen, J. E. Heparin and Low-Molecular-Weight Heparin Mechanisms of Action, Pharmacokinetics, Dosing, Monitoring, Efficacy, and Safety. *Chest* **2001**, *119*, 64S-94S.
42. Hirsh, J.; O'Donnell, M.; Eikelboom, J. W. Beyond Unfractionated Heparin and Warfarin: Current and Future Advances. *Circulation* **2007**, *116*, 552-560.
43. Lee, C. J.; Ansell, J. E. Direct Thrombin Inhibitors. *Br. J. Clin. Pharmacol.* **2011**, *72*, 581-92.
44. Xiao, Z.; Theroux, P. Platelet Activation with Unfractionated Heparin at Therapeutic Concentrations and Comparisons with a Low-Molecular-Weight Heparin and with a Direct Thrombin Inhibitor. *Circulation* **1998**, *97*, 251-6.
45. Alban, S. Pharmacological Strategies for Inhibition of Thrombin Activity. *Curr. Pharm. Des.* **2008**, *14*, 1152-75.
46. Eikelboom, J. W.; Zelenkofske, S. L.; Rusconi, C. P. Coagulation Factor Ixa as a Target for Treatment and Prophylaxis of Venous Thromboembolism. *Arterioscler. Thromb. Vasc. Biol.* **2010**, *30*, 382-387.
47. Povsic, T. J.; Cohen, M. G.; Mehran, R.; Buller, C. E.; Bode, C.; Cornel, J. H.; Kasprzak, J. D.; Montalescot, G.; Joseph, D.; Wargin, W. A.; et al. A Randomized, Partially Blinded, Multicenter, Active-Controlled, Dose-Ranging Study Assessing the Safety, Efficacy, and Pharmacodynamics of the Reg1 Anticoagulation System in Patients with Acute Coronary Syndromes: Design and Rationale of the Radar Phase Iib Trial. *Am. Heart J.* **2011**, *161*, 261-268.e2.
48. Povsic, T. J.; Cohen, M. G.; Chan, M. Y.; Zelenkofske, S. L.; Wargin, W. A.; Harrington, R. A.; Alexander, J. H.; Rusconi, C. P.; Becker, R. C. Dose Selection for a Direct and Selective Factor Ixa Inhibitor and Its Complementary Reversal Agent: Translating Pharmacokinetic and Pharmacodynamic Properties of the Reg1 System to Clinical Trial Design. *J. Thromb. Thrombolysis* **2011**, *32*, 21-31.
49. Bock, L. C.; Griffin, L. C.; Latham, J. A.; Vermaas, E. H.; Toole, J. J. Selection of Single-Stranded DNA Molecules That Bind and Inhibit Human Thrombin. *Nature* **1992**, *355*, 564-6.

50. Rusconi, C. P.; Scardino, E.; Layzer, J.; Pitoc, G. A.; Ortel, T. L.; Monroe, D.; Sullenger, B. A. Rna Aptamers as Reversible Antagonists of Coagulation Factor Ixa. *Nature* **2002**, *419*, 90-4.
51. Rusconi, C. P.; Roberts, J. D.; Pitoc, G. A.; Nimjee, S. M.; White, R. R.; Quick, G., Jr.; Scardino, E.; Fay, W. P.; Sullenger, B. A. Antidote-Mediated Control of an Anticoagulant Aptamer in Vivo. *Nat. Biotechnol.* **2004**, *22*, 1423-8.
52. Rosen, E. D.; Gailani, D.; Castellino, F. J. Fxi Is Essential for Thrombus Formation Following Fecl3-Induced Injury of the Carotid Artery in the Mouse. *Thromb. Haemost.* **2002**, *87*, 774-6.
53. Wang, X.; Smith, P. L.; Hsu, M. Y.; Gailani, D.; Schumacher, W. A.; Ogletree, M. L.; Seiffert, D. A. Effects of Factor Xi Deficiency on Ferric Chloride-Induced Vena Cava Thrombosis in Mice. *J. Thromb. Haemost.* **2006**, *4*, 1982-1988.
54. Renné, T.; Pozgajová, M.; Grüner, S.; Schuh, K.; Pauer, H.-U.; Burfeind, P.; Gailani, D.; Nieswandt, B. Defective Thrombus Formation in Mice Lacking Coagulation Factor Xii. *J. Exp. Med.* **2005**, *202*, 271-281.
55. Kleinschnitz, C.; Stoll, G.; Bendszus, M.; Schuh, K.; Pauer, H.-U.; Burfeind, P.; Renné, C.; Gailani, D.; Nieswandt, B.; Renné, T. Targeting Coagulation Factor Xii Provides Protection from Pathological Thrombosis in Cerebral Ischemia without Interfering with Hemostasis. *J. Exp. Med.* **2006**, *203*, 513-518.
56. Schumacher, W. A.; Luetzgen, J. M.; Quan, M. L.; Seiffert, D. A. Inhibition of Factor Xia as a New Approach to Anticoagulation. *Arterioscler. Thromb. Vasc. Biol.* **2010**, *30*, 388-392.
57. Renné, T.; Schmaier, A. H.; Nickel, K. F.; Blombäck, M.; Maas, C. In Vivo Roles of Factor Xii. *Blood* **2012**, *120*, 4296-4303.
58. Lin, J.; Deng, H.; Jin, L.; Pandey, P.; Quinn, J.; Cantin, S.; Rynkiewicz, M. J.; Gorga, J. C.; Bibbins, F.; Celatka, C. A.; et al. Design, Synthesis, and Biological Evaluation of Peptidomimetic Inhibitors of Factor Xia as Novel Anticoagulants. *J. Med. Chem.* **2006**, *49*, 7781-7791.
59. Larsson, M.; Rayzman, V.; Nolte, M. W.; Nickel, K. F.; Björkqvist, J.; Jämsä, A.; Hardy, M. P.; Fries, M.; Schmidbauer, S.; Hedenqvist, P.; et al. A Factor Xiia Inhibitory Antibody Provides Thromboprotection in Extracorporeal Circulation without Increasing Bleeding Risk. *Sci. Transl. Med.* **2014**, *6*, 222ra17.
60. Ansell, J.; Hirsh, J.; Hylek, E.; Jacobson, A.; Crowther, M.; Palareti, G.; American College of Chest, P. Pharmacology and Management of the Vitamin K Antagonists: American College of Chest Physicians Evidence-Based Clinical Practice Guidelines (8th Edition). *Chest* **2008**, *133*, 160S-198S.
61. Becker, R. C. The Importance of Factor Xa Regulatory Pathways in Vascular Thromboresistance: Focus on Protein Z. *J. Thromb. Thrombolysis* **2005**, *19*, 135-7.
62. Gonsalves, W. I.; Pruthi, R. K.; Patnaik, M. M. The New Oral Anticoagulants in Clinical Practice. *Mayo Clin. Proc.* **2013**, *88*, 495-511.
63. Alquwaizani, M.; Buckley, L.; Adams, C.; Fanikos, J. Anticoagulants: A Review of the Pharmacology, Dosing, and Complications. *Curr. Emerg. Hosp. Med. Rep.* **2013**, *1*, 83-97.
64. Cove, C. L.; Hylek, E. M. An Updated Review of Target-Specific Oral Anticoagulants Used in Stroke Prevention in Atrial Fibrillation, Venous Thromboembolic Disease, and Acute Coronary Syndromes. *J. Am. Heart Assoc.* **2013**, *2*.

65. Giugliano, R. P.; Ruff, C. T.; Braunwald, E.; Murphy, S. A.; Wiviott, S. D.; Halperin, J. L.; Waldo, A. L.; Ezekowitz, M. D.; Weitz, J. I.; Špinar, J.; et al. Edoxaban Versus Warfarin in Patients with Atrial Fibrillation. *N. Engl. J. Med.* **2013**, *369*, 2093-2104.
66. Weitz, J. I. New Oral Anticoagulants: A View from the Laboratory. *Am. J. Hematol.* **2012**, *87 Suppl 1*, S133-6.
67. Heitman, S. J.; MacKay, E.; Hilsden, R. J.; Rostom, A. Novel Oral Anticoagulants: Is the Convenience Worth the Risk? *Gastroenterology* **2013**, *145*, 42-45.
68. Holster, I. L.; Valkhoff, V. E.; Kuipers, E. J.; Tjwa, E. T. T. L. New Oral Anticoagulants Increase Risk for Gastrointestinal Bleeding: A Systematic Review and Meta-Analysis. *Gastroenterology* **2013**, *145*, 105-112.e15.
69. Siegal, D.; Cuker, A. Reversal of Novel Oral Anticoagulants in Patients with Major Bleeding. *J. Thromb. Thrombolysis* **2013**, *35*, 391-398.
70. Bhatt, D. L.; Chew, D. P.; Hirsch, A. T.; Ringleb, P. A.; Hacke, W.; Topol, E. J. Superiority of Clopidogrel Versus Aspirin in Patients with Prior Cardiac Surgery. *Circulation* **2001**, *103*, 363-8.
71. Bhatt, D. L.; Topol, E. J. Scientific and Therapeutic Advances in Antiplatelet Therapy. *Nat. Rev. Drug Discov.* **2003**, *2*, 15-28.
72. Kong, D. F.; Califf, R. M.; Miller, D. P.; Moliterno, D. J.; White, H. D.; Harrington, R. A.; Tchong, J. E.; Lincoff, A. M.; Hasselblad, V.; Topol, E. J. Clinical Outcomes of Therapeutic Agents That Block the Platelet Glycoprotein Iib/Iiia Integrin in Ischemic Heart Disease. *Circulation* **1998**, *98*, 2829-35.
73. Capodanno, D.; Ferreira, J. L.; Angiolillo, D. J. Antiplatelet Therapy: New Pharmacological Agents and Changing Paradigms. *J. Thromb. Haemost.* **2013**, *11*, 316-329.
74. Anderson, H. V.; Willerson, J. T. Thrombolysis in Acute Myocardial Infarction. *N. Engl. J. Med.* **1993**, *329*, 703-9.
75. Marder, V. J.; Sherry, S. Thrombolytic Therapy: Current Status (1). *N. Engl. J. Med.* **1988**, *318*, 1512-20.
76. The NINDS t-PA Stroke Study Group Intracerebral Hemorrhage after Intravenous T-PA Therapy for Ischemic Stroke. *Stroke* **1997**, *28*, 2109-2118.
77. Jiao, Y.; Ubrich, N.; Marchand-Arvier, M.; Vigneron, C.; Hoffman, M.; Lecompte, T.; Maincent, P. In Vitro and in Vivo Evaluation of Oral Heparin-Loaded Polymeric Nanoparticles in Rabbits. *Circulation* **2002**, *105*, 230-235.
78. Paliwal, R.; Paliwal, S. R.; Agrawal, G. P.; Vyas, S. P. Biomimetic Solid Lipid Nanoparticles for Oral Bioavailability Enhancement of Low Molecular Weight Heparin and Its Lipid Conjugates: In Vitro and in Vivo Evaluation. *Mol. Pharm.* **2011**, *8*, 1314-1321.
79. Bai, S.; Thomas, C.; Ahsan, F. Dendrimers as a Carrier for Pulmonary Delivery of Enoxaparin, a Low-Molecular Weight Heparin. *J. Pharm. Sci.* **2007**, *96*, 2090-2106.
80. Palekar, R. U.; Myerson, J. W.; Schlesinger, P. H.; Sadler, J. E.; Pan, H.; Wickline, S. A. Thrombin-Targeted Liposomes Establish a Sustained Localized Anticlotting Barrier against Acute Thrombosis. *Mol. Pharm.* **2013**, *10*, 4168-4175.
81. Myerson, J.; He, L.; Lanza, G.; Tollefsen, D.; Wickline, S. Thrombin-Inhibiting Perfluorocarbon Nanoparticles Provide a Novel Strategy for the Treatment and Magnetic Resonance Imaging of Acute Thrombosis. *J. Thromb. Haemost.* **2011**, *9*, 1292-1300.
82. Shiang, Y.-C.; Huang, C.-C.; Wang, T.-H.; Chien, C.-W.; Chang, H.-T. Aptamer-Conjugated Nanoparticles Efficiently Control the Activity of Thrombin. *Adv. Funct. Mater.* **2010**, *20*, 3175-3182.

83. Shiang, Y.-C.; Hsu, C.-L.; Huang, C.-C.; Chang, H.-T. Gold Nanoparticles Presenting Hybridized Self-Assembled Aptamers That Exhibit Enhanced Inhibition of Thrombin. *Angew. Chem. Int. Ed. Engl.* **2011**, *50*, 7660-7665.
84. Rangnekar, A.; Zhang, A. M.; Li, S. S.; Bompiani, K. M.; Hansen, M. N.; Gothelf, K. V.; Sullenger, B. A.; LaBean, T. H. Increased Anticoagulant Activity of Thrombin-Binding DNA Aptamers by Nanoscale Organization on DNA Nanostructures. *Nanomed: Nanotechnol. Biol. Med.* **2012**, *8*, 673-681.
85. Peters, D.; Kastantin, M.; Kotamraju, V. R.; Karmali, P. P.; Gujraty, K.; Tirrell, M.; Ruoslahti, E. Targeting Atherosclerosis by Using Modular, Multifunctional Micelles. *Proc. Natl. Acad. Sci. U. S. A.* **2009**, *106*, 9815-9819.
86. McCarthy, J. R.; Jaffer, F. A. The Role of Nanomedicine in the Imaging and Therapy of Thrombosis. *Nanomed.* **2011**, *6*, 1291-1293.
87. Bi, F.; Zhang, J.; Su, Y.; Tang, Y. C.; Liu, J. N. Chemical Conjugation of Urokinase to Magnetic Nanoparticles for Targeted Thrombolysis. *Biomaterials* **2009**, *30*, 5125-30.
88. Ma, Y. H.; Wu, S. Y.; Wu, T.; Chang, Y. J.; Hua, M. Y.; Chen, J. P. Magnetically Targeted Thrombolysis with Recombinant Tissue Plasminogen Activator Bound to Polyacrylic Acid-Coated Nanoparticles. *Biomaterials* **2009**, *30*, 3343-51.
89. Marsh, J. N.; Hu, G.; Scott, M. J.; Zhang, H.; Goette, M. J.; Gaffney, P. J.; Caruthers, S. D.; Wickline, S. A.; Abendschein, D.; Lanza, G. M. A Fibrin-Specific Thrombolytic Nanomedicine Approach to Acute Ischemic Stroke. *Nanomed.* **2011**, *6*, 605-15.
90. McCarthy, J. R.; Sazonova, I. Y.; Erdem, S. S.; Hara, T.; Thompson, B. D.; Patel, P.; Botnaru, I.; Lin, C. P.; Reed, G. L.; Weissleder, R.; et al. Multifunctional Nanoagent for Thrombus-Targeted Fibrinolytic Therapy. *Nanomed.* **2012**, *7*, 1017-28.
91. Korin, N.; Kanapathipillai, M.; Matthews, B. D.; Crescente, M.; Brill, A.; Mammoto, T.; Ghosh, K.; Jurek, S.; Bencherif, S. A.; Bhatta, D.; et al. Shear-Activated Nanotherapeutics for Drug Targeting to Obstructed Blood Vessels. *Science* **2012**, *337*, 738-742.
92. IARC Globocan 2012: Estimated Cancer Incidence, Mortality, and Prevalence Worldwide in 2012. (accessed March 25).
93. Thiery, J. P. Epithelial-Mesenchymal Transitions in Tumour Progression. *Nat. Rev. Cancer* **2002**, *2*, 442-54.
94. Smith, R. A.; Manassaram-Baptiste, D.; Brooks, D.; Cokkinides, V.; Doroshenk, M.; Saslow, D.; Wender, R. C.; Brawley, O. W. Cancer Screening in the United States, 2014: A Review of Current American Cancer Society Guidelines and Current Issues in Cancer Screening. *CA. Cancer J. Clin.* **2014**, *64*, 30-51.
95. Hanash, S. M.; Baik, C. S.; Kallioniemi, O. Emerging Molecular Biomarkers--Blood-Based Strategies to Detect and Monitor Cancer. *Nat. Rev. Clin. Oncol.* **2011**, *8*, 142-50.
96. Frangioni, J. V. New Technologies for Human Cancer Imaging. *J. Clin. Oncol.* **2008**, *26*, 4012-4021.
97. Bernier, J.; Hall, E. J.; Giaccia, A. Radiation Oncology: A Century of Achievements. *Nat. Rev. Cancer* **2004**, *4*, 737-47.
98. Chabner, B. A.; Roberts, T. G., Jr. Timeline: Chemotherapy and the War on Cancer. *Nat. Rev. Cancer* **2005**, *5*, 65-72.
99. Sawyers, C. Targeted Cancer Therapy. *Nature* **2004**, *432*, 294-7.
100. Mellman, I.; Coukos, G.; Dranoff, G. Cancer Immunotherapy Comes of Age. *Nature* **2011**, *480*, 480-9.

101. Vanneman, M.; Dranoff, G. Combining Immunotherapy and Targeted Therapies in Cancer Treatment. *Nat. Rev. Cancer* **2012**, *12*, 237-51.
102. Minchinton, A. I.; Tannock, I. F. Drug Penetration in Solid Tumours. *Nat. Rev. Cancer* **2006**, *6*, 583-592.
103. Jain, R. K. Transport of Molecules, Particles, and Cells in Solid Tumors. *Annu. Rev. Biomed. Eng.* **1999**, *1*, 241-263.
104. Yuan, F. Transvascular Drug Delivery in Solid Tumors. *Semin. Radiat. Oncol.* **1998**, *8*, 164-175.
105. Roberts, W. G.; Palade, G. E. Neovasculature Induced by Vascular Endothelial Growth Factor Is Fenestrated. *Cancer Res.* **1997**, *57*, 765-772.
106. Hobbs, S. K.; Monsky, W. L.; Yuan, F.; Roberts, W. G.; Griffith, L.; Torchilin, V. P.; Jain, R. K. Regulation of Transport Pathways in Tumor Vessels: Role of Tumor Type and Microenvironment. *Proc. Natl. Acad. Sci. U. S. A.* **1998**, *95*, 4607-4612.
107. Lichtenbeld, H. C.; Yuan, F.; Michel, C. C.; Jain, R. K. Perfusion of Single Tumor Microvessels: Application to Vascular Permeability Measurement. *Microcirculation* **1996**, *3*, 349-357.
108. Boucher, Y.; Jain, R. K. Microvascular Pressure Is the Principal Driving Force for Interstitial Hypertension in Solid Tumors: Implications for Vascular Collapse. *Cancer Res.* **1992**, *52*, 5110-5114.
109. Boucher, Y.; Baxter, L. T.; Jain, R. K. Interstitial Pressure Gradients in Tissue-Isolated and Subcutaneous Tumors: Implications for Therapy. *Cancer Res.* **1990**, *50*, 4478-4484.
110. Senger, D.; Galli, S.; Dvorak, A.; Perruzzi, C.; Harvey, V.; Dvorak, H. Tumor Cells Secrete a Vascular Permeability Factor That Promotes Accumulation of Ascites Fluid. *Science* **1983**, *219*, 983-985.
111. Roberts, W.; Palade, G. Increased Microvascular Permeability and Endothelial Fenestration Induced by Vascular Endothelial Growth Factor. *J. Cell Sci.* **1995**, *108*, 2369-2379.
112. Rosenstein, M.; Ettinghausen, S.; Rosenberg, S. Extravasation of Intravascular Fluid Mediated by the Systemic Administration of Recombinant Interleukin 2. *J. Immunol.* **1986**, *137*, 1735-1742.
113. Khawli, L. A.; Hu, P.; Epstein, A. L. Nhs76/Pep2, a Fully Human Vasopermeability-Enhancing Agent to Increase the Uptake and Efficacy of Cancer Chemotherapy. *Clin. Cancer Res.* **2005**, *11*, 3084-3093.
114. LeBerthon, B.; Khawli, L. A.; Alauddin, M.; Miller, G. K.; Charak, B. S.; Mazumder, A.; Epstein, A. L. Enhanced Tumor Uptake of Macromolecules Induced by a Novel Vasoactive Interleukin 2 Immunoconjugate. *Cancer Res.* **1991**, *51*, 2694-2698.
115. Cope, D. A.; Dewhirst, M. W.; Friedman, H. S.; Bigner, D. D.; Zalutsky, M. R. Enhanced Delivery of a Monoclonal Antibody F(Ab')₂ Fragment to Subcutaneous Human Glioma Xenografts Using Local Hyperthermia. *Cancer Res.* **1990**, *50*, 1803-1809.
116. Hauck, M. L.; Dewhirst, M. W.; Bigner, D. D.; Zalutsky, M. R. Local Hyperthermia Improves Uptake of a Chimeric Monoclonal Antibody in a Subcutaneous Xenograft Model. *Clin. Cancer Res.* **1997**, *3*, 63-70.
117. Kong, G.; Anyarambhatla, G.; Petros, W. P.; Braun, R. D.; Colvin, O. M.; Needham, D.; Dewhirst, M. W. Efficacy of Liposomes and Hyperthermia in a Human Tumor Xenograft Model: Importance of Triggered Drug Release. *Cancer Res.* **2000**, *60*, 6950-6957.
118. Kong, G.; Braun, R. D.; Dewhirst, M. W. Characterization of the Effect of Hyperthermia on Nanoparticle Extravasation from Tumor Vasculature. *Cancer Res.* **2001**, *61*, 3027-3032.

119. Galaup, A.; Cazes, A.; Le Jan, S.; Philippe, J.; Connault, E.; Le Coz, E.; Mekid, H.; Mir, L. M.; Opolon, P.; Corvol, P.; et al. Angiopoietin-Like 4 Prevents Metastasis through Inhibition of Vascular Permeability and Tumor Cell Motility and Invasiveness. *Proc. Natl. Acad. Sci. U. S. A.* **2006**, *103*, 18721-18726.
120. Criscuoli, M. L.; Nguyen, M.; Eliceiri, B. P. Tumor Metastasis but Not Tumor Growth Is Dependent on Src-Mediated Vascular Permeability. *Blood* **2005**, *105*, 1508-1514.
121. Burke, D.; Davies, M. M.; Zweit, J.; Flower, M. A.; Ott, R. J.; Dworkin, M. J.; Glover, C.; McCready, V. R.; Carnochan, P.; Allen-Mersh, T. G. Continuous Angiotensin Ii Infusion Increases Tumour: Normal Blood Flow Ratio in Colo-Rectal Liver Metastases. *Br. J. Cancer* **2001**, *85*, 1640-1645.
122. Thurber, G. M.; Schmidt, M. M.; Wittrup, K. D. Antibody Tumor Penetration: Transport Opposed by Systemic and Antigen-Mediated Clearance. *Adv. Drug. Deliv. Rev.* **2008**, *60*, 1421-1434.
123. Netti, P. A.; Hamberg, L. M.; Babich, J. W.; Kierstead, D.; Graham, W.; Hunter, G. J.; Wolf, G. L.; Fischman, A.; Boucher, Y.; Jain, R. K. Enhancement of Fluid Filtration across Tumor Vessels: Implication for Delivery of Macromolecules. *Proc. Natl. Acad. Sci. U. S. A.* **1999**, *96*, 3137-3142.
124. Netti, P. A.; Baxter, L. T.; Boucher, Y.; Skalak, R.; Jain, R. K. Time-Dependent Behavior of Interstitial Fluid Pressure in Solid Tumors: Implications for Drug Delivery. *Cancer Res.* **1995**, *55*, 5451-5458.
125. Znati, C. A.; Rosenstein, M.; Boucher, Y.; Epperly, M. W.; Bloomer, W. D.; Jain, R. K. Effect of Radiation on Interstitial Fluid Pressure and Oxygenation in a Human Tumor Xenograft. *Cancer Res.* **1996**, *56*, 964-968.
126. Baranowska-Kortylewicz, J.; Abe, M.; Pietras, K.; Kortylewicz, Z. P.; Kurizaki, T.; Nearman, J.; Paulsson, J.; Mosley, R. L.; Enke, C. A.; Ostman, A. Effect of Platelet-Derived Growth Factor Receptor- β Inhibition with Sti571 on Radioimmunotherapy. *Cancer Res.* **2005**, *65*, 7824-7831.
127. Pietras, K.; Stumm, M.; Hubert, M.; Buchdunger, E.; Rubin, K.; Heldin, C.-H.; McSheehy, P.; Wartmann, M.; Åstman, A. Sti571 Enhances the Therapeutic Index of Etoposide by a Tumor-Selective Increase of Drug Uptake. *Clin. Cancer Res.* **2003**, *9*, 3779-3787.
128. Lee, I.; Boucher, Y.; Jain, R. K. Nicotinamide Can Lower Tumor Interstitial Fluid Pressure: Mechanistic and Therapeutic Implications. *Cancer Res.* **1992**, *52*, 3237-3240.
129. Inai, T.; Mancuso, M.; Hashizume, H.; Baffert, F.; Haskell, A.; Baluk, P.; Hu-Lowe, D. D.; Shalinsky, D. R.; Thurston, G.; Yancopoulos, G. D.; et al. Inhibition of Vascular Endothelial Growth Factor (Vegf) Signaling in Cancer Causes Loss of Endothelial Fenestrations, Regression of Tumor Vessels, and Appearance of Basement Membrane Ghosts. *Am. J. Pathol.* **2004**, *165*, 35-52.
130. Jain, R. K. Normalization of Tumor Vasculature: An Emerging Concept in Antiangiogenic Therapy. *Science* **2005**, *307*, 58-62.
131. Tong, R. T.; Boucher, Y.; Kozin, S. V.; Winkler, F.; Hicklin, D. J.; Jain, R. K. Vascular Normalization by Vascular Endothelial Growth Factor Receptor 2 Blockade Induces a Pressure Gradient across the Vasculature and Improves Drug Penetration in Tumors. *Cancer Res.* **2004**, *64*, 3731-3736.
132. Turetschek, K.; Preda, A.; Novikov, V.; Brasch, R. C.; Weinmann, H. J.; Wunderbaldinger, P.; Roberts, T. P. L. Tumor Microvascular Changes in Antiangiogenic

- Treatment: Assessment by Magnetic Resonance Contrast Media of Different Molecular Weights. *J. Magn. Reson. Imaging* **2004**, *20*, 138-144.
133. Yuan, F.; Chen, Y.; Dellian, M.; Safabakhsh, N.; Ferrara, N.; Jain, R. K. Time-Dependent Vascular Regression and Permeability Changes in Established Human Tumor Xenografts Induced by an Anti-Vascular Endothelial Growth Factor/Vascular Permeability Factor Antibody. *Proc. Natl. Acad. Sci. U. S. A.* **1996**, *93*, 14765-14770.
134. Hurwitz, H.; Fehrenbacher, L.; Novotny, W.; Cartwright, T.; Hainsworth, J.; Heim, W.; Berlin, J.; Baron, A.; Griffing, S.; Holmgren, E.; et al. Bevacizumab Plus Irinotecan, Fluorouracil, and Leucovorin for Metastatic Colorectal Cancer. *N. Engl. J. Med.* **2004**, *350*, 2335-2342.
135. Nakahara, T.; Norberg, S. M.; Shalinsky, D. R.; Hu-Lowe, D. D.; McDonald, D. M. Effect of Inhibition of Vascular Endothelial Growth Factor Signaling on Distribution of Extravasated Antibodies in Tumors. *Cancer Res.* **2006**, *66*, 1434-1445.
136. Duncan, R. The Dawning Era of Polymer Therapeutics. *Nat. Rev. Drug Discov.* **2003**, *2*, 347-60.
137. Erdogan, S.; Medarova, Z. O.; Roby, A.; Moore, A.; Torchilin, V. P. Enhanced Tumor Mr Imaging with Gadolinium-Loaded Polychelating Polymer-Containing Tumor-Targeted Liposomes. *J. Magn. Reson. Imaging* **2008**, *27*, 574-80.
138. Akerman, M. E.; Chan, W. C.; Laakkonen, P.; Bhatia, S. N.; Ruoslahti, E. Nanocrystal Targeting in Vivo. *Proc. Natl. Acad. Sci. U. S. A.* **2002**, *99*, 12617-21.
139. Farokhzad, O. C.; Cheng, J.; Teply, B. A.; Sherifi, I.; Jon, S.; Kantoff, P. W.; Richie, J. P.; Langer, R. Targeted Nanoparticle-Aptamer Bioconjugates for Cancer Chemotherapy in Vivo. *Proc. Natl. Acad. Sci. U. S. A.* **2006**, *103*, 6315-20.
140. Weissleder, R.; Kelly, K.; Sun, E. Y.; Shtatland, T.; Josephson, L. Cell-Specific Targeting of Nanoparticles by Multivalent Attachment of Small Molecules. *Nat Biotechnol* **2005**, *23*, 1418-23.
141. Medarova, Z.; Pham, W.; Farrar, C.; Petkova, V.; Moore, A. In Vivo Imaging of Sirna Delivery and Silencing in Tumors. *Nat. Med.* **2007**, *13*, 372-7.
142. Maiseyeu, A.; Mihai, G.; Kampfrath, T.; Simonetti, O. P.; Sen, C. K.; Roy, S.; Rajagopalan, S.; Parthasarathy, S. Gadolinium Containing Phosphatidylserine Liposomes for Molecular Imaging of Atherosclerosis. *J. Lipid Res.* **2008**.
143. Discher, B. M.; Won, Y. Y.; Ege, D. S.; Lee, J. C.; Bates, F. S.; Discher, D. E.; Hammer, D. A. Polymersomes: Tough Vesicles Made from Diblock Copolymers. *Science* **1999**, *284*, 1143-6.
144. Torchilin, V. P. Structure and Design of Polymeric Surfactant-Based Drug Delivery Systems. *J. Control. Release* **2001**, *73*, 137-72.
145. Sengupta, S.; Eavarone, D.; Capila, I.; Zhao, G.; Watson, N.; Kiziltepe, T.; Sasisekharan, R. Temporal Targeting of Tumour Cells and Neovasculature with a Nanoscale Delivery System. *Nature* **2005**, *436*, 568-72.
146. Nguyen, P. M.; Hammond, P. T. Amphiphilic Linear-Dendritic Triblock Copolymers Composed of Poly(Amidoamine) and Poly(Propylene Oxide) and Their Micellar-Phase and Encapsulation Properties. *Langmuir* **2006**, *22*, 7825-7832.
147. Kojima, C.; Kono, K.; Maruyama, K.; Takagishi, T. Synthesis of Polyamidoamine Dendrimers Having Poly(Ethylene Glycol) Grafts and Their Ability to Encapsulate Anticancer Drugs. *Bioconjug. Chem.* **2000**, *11*, 910-7.

148. Patri, A. K.; Majoros, I. J.; Baker, J. R. Dendritic Polymer Macromolecular Carriers for Drug Delivery. *Curr. Opin. Chem. Biol.* **2002**, *6*, 466-71.
149. Patri, A. K.; Myc, A.; Beals, J.; Thomas, T. P.; Bander, N. H.; Baker, J. R., Jr. Synthesis and in Vitro Testing of J591 Antibody-Dendrimer Conjugates for Targeted Prostate Cancer Therapy. *Bioconjug. Chem.* **2004**, *15*, 1174-81.
150. Wood, K. C.; Little, S. R.; Langer, R.; Hammond, P. T. A Family of Hierarchically Self-Assembling Linear-Dendritic Hybrid Polymers for Highly Efficient Targeted Gene Delivery¹³. *Angewandte Chemie* **2005**, *117*, 6862-6866.
151. von Maltzahn, G.; Park, J.-H.; Agrawal, A.; Bandaru, N. K.; Das, S. K.; Sailor, M. J.; Bhatia, S. N. Computationally Guided Photothermal Tumor Therapy Using Long-Circulating Gold Nanorod Antennas. *Cancer Res.* **2009**, *69*, 3892-3900.
152. Diagaradjane, P.; Shetty, A.; Wang, J. C.; Elliott, A. M.; Schwartz, J.; Shentu, S.; Park, H. C.; Deorukhkar, A.; Stafford, R. J.; Cho, S. H.; et al. Modulation of in Vivo Tumor Radiation Response Via Gold Nanoshell-Mediated Vascular-Focused Hyperthermia: Characterizing an Integrated Antihypoxic and Localized Vascular Disrupting Targeting Strategy. *Nano Lett.* **2008**, *8*, 1492-500.
153. Allen, T. M.; Cullis, P. R. Drug Delivery Systems: Entering the Mainstream. *Science* **2004**, *303*, 1818-22.
154. Ruoslahti, E. Drug Targeting to Specific Vascular Sites. *Drug Discov. Today* **2002**, *7*, 1138-43.
155. Wickham, T. J. Targeting Adenovirus. *Gene Ther.* **2000**, *7*, 110-4.
156. Jain, R. K. Delivery of Molecular and Cellular Medicine to Solid Tumors. *J. Control. Release* **1998**, *53*, 49-67.
157. Jain, R. K. Delivery of Molecular and Cellular Medicine to Solid Tumors. *Adv Drug Deliv Rev* **2001**, *46*, 149-68.
158. Satchi-Fainaro, R.; Puder, M.; Davies, J. W.; Tran, H. T.; Sampson, D. A.; Greene, A. K.; Corfas, G.; Folkman, J. Targeting Angiogenesis with a Conjugate of Hpma Copolymer and Tnp-470. *Nat. Med.* **2004**, *10*, 255-61.
159. Ruoslahti, E.; Rajotte, D. An Address System in the Vasculature of Normal Tissues and Tumors. *Annu. Rev. Immunol.* **2000**, *18*, 813-827.
160. Matsumura, Y.; Maeda, H. A New Concept for Macromolecular Therapeutics in Cancer Chemotherapy: Mechanism of Tumor-tropic Accumulation of Proteins and the Antitumor Agent Smancs. *Cancer Res.* **1986**, *46*, 6387-6392.
161. Jain, R. K. Vascular and Interstitial Barriers to Delivery of Therapeutic Agents in Tumors. *Cancer Metastasis Rev.* **1990**, *9*, 253-66.
162. Tabata, Y.; Murakami, Y.; Ikada, Y. Tumor Accumulation of Poly(Vinyl Alcohol) of Different Sizes after Intravenous Injection. *J. Control. Release* **1998**, *50*, 123-33.
163. Moghimi, S. M.; Hunter, A. C. Recognition by Macrophages and Liver Cells of Opsonized Phospholipid Vesicles and Phospholipid Headgroups. *Pharm. Res.* **2001**, *18*, 1-8.
164. Moghimi, S. M.; Hunter, A. C.; Murray, J. C. Long-Circulating and Target-Specific Nanoparticles: Theory to Practice. *Pharmacol. Rev.* **2001**, *53*, 283-318.
165. Nicolazzi, C.; Mignet, N.; de la Figuera, N.; Cadet, M.; Ibad, R. T.; Seguin, J.; Scherman, D.; Bessodes, M. Anionic Polyethyleneglycol Lipids Added to Cationic Lipoplexes Increase Their Plasmatic Circulation Time. *J. Control. Release* **2003**, *88*, 429-43.

166. Hoffman, J. A.; Giraudo, E.; Singh, M.; Zhang, L.; Inoue, M.; Porkka, K.; Hanahan, D.; Ruoslahti, E. Progressive Vascular Changes in a Transgenic Mouse Model of Squamous Cell Carcinoma. *Cancer Cell* **2003**, *4*, 383-91.
167. Porkka, K.; Laakkonen, P.; Hoffman, J. A.; Bernasconi, M.; Ruoslahti, E. A Fragment of the Hmgn2 Protein Homes to the Nuclei of Tumor Cells and Tumor Endothelial Cells in Vivo. *Proc. Natl. Acad. Sci. U. S. A.* **2002**, *99*, 7444-7449.
168. Arap, W.; Pasqualini, R.; Ruoslahti, E. Cancer Treatment by Targeted Drug Delivery to Tumor Vasculature in a Mouse Model. *Science* **1998**, *279*, 377-380.
169. Weissleder, R.; Kelly, K.; Sun, E. Y.; Shtatland, T.; Josephson, L. Cell-Specific Targeting of Nanoparticles by Multivalent Attachment of Small Molecules. *Nat. Biotechnol.* **2005**, *23*, 1418-1423.
170. Putnam, D.; Kopecek, J. Enantioselective Release of 5-Fluorouracil from N-(2-Hydroxypropyl)Methacrylamide-Based Copolymers Via Lysosomal Enzymes. *Bioconjug. Chem.* **1995**, *6*, 483-92.
171. Farokhzad, O. C.; Jon, S.; Khademhosseini, A.; Tran, T. N.; Lavan, D. A.; Langer, R. Nanoparticle-Aptamer Bioconjugates: A New Approach for Targeting Prostate Cancer Cells. *Cancer Res.* **2004**, *64*, 7668-72.
172. Simberg, D.; Duza, T.; Park, J. H.; Essler, M.; Pilch, J.; Zhang, L.; Derfus, A. M.; Yang, M.; Hoffman, R. M.; Bhatia, S.; et al. Biomimetic Amplification of Nanoparticle Homing to Tumors. *Proc. Natl. Acad. Sci. U. S. A.* **2007**, *104*, 932-936.
173. Ruoslahti, E. Specialization of Tumour Vasculature. *Nat. Rev. Cancer* **2002**, *2*, 83-90.
174. Wickline, S. A.; Lanza, G. M. Nanotechnology for Molecular Imaging and Targeted Therapy. *Circulation* **2003**, *107*, 1092-1095.
175. Sahoo, S. K.; Labhasetwar, V. Nanotech Approaches to Drug Delivery and Imaging. *Drug Discov. Today* **2003**, *8*, 1112-20.
176. Bartlett, D. W.; Su, H.; Hildebrandt, I. J.; Weber, W. A.; Davis, M. E. Impact of Tumor-Specific Targeting on the Biodistribution and Efficacy of Sirna Nanoparticles Measured by Multimodality in Vivo Imaging. *Proc. Natl. Acad. Sci. U. S. A.* **2007**, *104*, 15549-15554.
177. Byrne, J. D.; Betancourt, T.; Brannon-Peppas, L. Active Targeting Schemes for Nanoparticle Systems in Cancer Therapeutics. *Adv. Drug. Deliv. Rev.* **2008**, *60*, 1615-1626.
178. Teesalu, T.; Sugahara, K. N.; Kotamraju, V. R.; Ruoslahti, E. C-End Rule Peptides Mediate Neuropilin-1-Dependent Cell, Vascular, and Tissue Penetration. *Proc. Natl. Acad. Sci. U. S. A.* **2009**, *106*, 16157-16162.
179. Sugahara, K. N.; Teesalu, T.; Karmali, P. P.; Kotamraju, V. R.; Agemy, L.; Girard, O. M.; Hanahan, D.; Mattrey, R. F.; Ruoslahti, E. Tissue-Penetrating Delivery of Compounds and Nanoparticles into Tumors. *Cancer Cell* **2009**, *16*, 510-520.
180. Ruoslahti, E.; Bhatia, S. N.; Sailor, M. J. Targeting of Drugs and Nanoparticles to Tumors. *J. Cell Biol.* **2010**, *188*, 759-768.
181. Kranenborg, M. H. G. C.; Boerman, O. C.; Oosterwijk-Wakka, J. C.; Weijert, M. C. A. D.; Corstens, F. H. M.; Oosterwijk, E. Two-Step Radio-Immunotargeting of Renal-Cell Carcinoma Xenografts in Nude Mice with Anti-Renal-Cell-Carcinoma X Anti-Dtpa Bispecific Monoclonal Antibodies. *Int. J. Cancer* **1998**, *75*, 74-80.
182. von Maltzahn, G.; Park, J.-H.; Lin, K. Y.; Singh, N.; Schwöppe, C.; Mesters, R.; Berdel, W. E.; Ruoslahti, E.; Sailor, M. J.; Bhatia, S. N. Nanoparticles That Communicate in Vivo to Amplify Tumour Targeting. *Nat. Mater.* **2011**, *10*, 545-552.

183. Fogal, V.; Zhang, L.; Krajewski, S.; Ruoslahti, E. Mitochondrial/Cell-Surface Protein P32/Gc1qr as a Molecular Target in Tumor Cells and Tumor Stroma. *Cancer Res.* **2008**, *68*, 7210-7218.
184. Park, J.-H.; von Maltzahn, G.; Xu, M. J.; Fogal, V.; Kotamraju, V. R.; Ruoslahti, E.; Bhatia, S. N.; Sailor, M. J. Cooperative Nanomaterial System to Sensitize, Target, and Treat Tumors. *Proc. Natl. Acad. Sci. U. S. A.* **2010**, *107*, 981-986.
185. Laakkonen, P.; Porkka, K.; Hoffman, J. A.; Ruoslahti, E. A Tumor-Homing Peptide with a Targeting Specificity Related to Lymphatic Vessels. *Nat. Med.* **2002**, *8*, 751-755.
186. Siemann, D. W.; Horsman, M. R., Small-Molecule Vascular Disrupting Agents in Cancer Therapy. In *Cancer Drug Delivery and Development, Antiangiogenic Agents in Cancer Therapy*, Teicher, B. A.; Ellis, L. M., Eds. Humana Press: 2007; Vol. 2nd Edition.
187. Tozer, G. M.; Kanthou, C.; Baguley, B. C. Disrupting Tumour Blood Vessels. *Nat. Rev. Cancer* **2005**, *5*, 423-435.
188. Bruce, C. B.; Lai-Ming, C. Dmxa: An Antivascular Agent with Multiple Host Responses. *Int. J. Radiat. Oncol. Biol. Phys.* **2002**, *54*, 1503-1511.
189. Eskens, F.; Hinnen, P. Vascular Disrupting Agents in Clinical Development. *Br. J. Cancer* **2007**, *96*, 1159-1165.
190. Kanthou, C.; Tozer, G. M. The Tumor Vascular Targeting Agent Combretastatin a-4-Phosphate Induces Reorganization of the Actin Cytoskeleton and Early Membrane Blebbing in Human Endothelial Cells. *Blood* **2002**, *99*, 2060-2069.
191. Tozer, G. M.; Prise, V. E.; Wilson, J.; Cemazar, M.; Shan, S.; Dewhurst, M. W.; Barber, P. R.; Vojnovic, B.; Chaplin, D. J. Mechanisms Associated with Tumor Vascular Shut-Down Induced by Combretastatin a-4 Phosphate: Intravital Microscopy and Measurement of Vascular Permeability. *Cancer Res.* **2001**, *61*, 6413-6422.
192. Michael, F. M.; Anthony, W. F.; Richard, P. H. The Relationship between Elevated Interstitial Fluid Pressure and Blood Flow in Tumors: A Bioengineering Analysis. *Int. J. Radiat. Oncol. Biol. Phys.* **1999**, *43*, 1111-1123.
193. Anderson, H. L.; Yap, J. T.; Miller, M. P.; Robbins, A.; Jones, T.; Price, P. M. Assessment of Pharmacodynamic Vascular Response in a Phase I Trial of Combretastatin A4 Phosphate. *J. Clin. Oncol.* **2003**, *21*, 2823-2830.
194. Rustin, G. J. S.; Galbraith, S. M.; Anderson, H.; Stratford, M.; Folkes, L. K.; Sena, L.; Gumbrell, L.; Price, P. M. Phase I Clinical Trial of Weekly Combretastatin A4 Phosphate: Clinical and Pharmacokinetic Results. *J. Clin. Oncol.* **2003**, *21*, 2815-2822.
195. Stevenson, J. P.; Rosen, M.; Sun, W.; Gallagher, M.; Haller, D. G.; Vaughn, D.; Giantonio, B.; Zimmer, R.; Petros, W. P.; Stratford, M.; et al. Phase I Trial of the Antivascular Agent Combretastatin A4 Phosphate on a 5-Day Schedule to Patients with Cancer: Magnetic Resonance Imaging Evidence for Altered Tumor Blood Flow. *J. Clin. Oncol.* **2003**, *21*, 4428-4438.
196. Cooney, M. M.; Radivoyevitch, T.; Dowlati, A.; Overmoyer, B.; Levitan, N.; Robertson, K.; Levine, S. L.; DeCaro, K.; Buchter, C.; Taylor, A.; et al. Cardiovascular Safety Profile of Combretastatin A4 Phosphate in a Single-Dose Phase I Study in Patients with Advanced Cancer. *Clin. Cancer Res.* **2004**, *10*, 96-100.
197. Cooney, M. M.; Savvides, P.; Agarwala, S.; Wang, D.; Flick, S.; Bergant, S.; Bhakta, S.; Lavertu, P.; Ortiz, J.; Remick, S. Phase II Study of Combretastatin A4 Phosphate (Ca4p) in Patients with Advanced Anaplastic Thyroid Carcinoma (Atc). *J. Clin. Oncol.* **2006**, *24*, 5580-.

198. Kanthou, C.; Tozer, G. M. Microtubule Depolymerizing Vascular Disrupting Agents: Novel Therapeutic Agents for Oncology and Other Pathologies. *Int. J. Exp. Pathol.* **2009**, *90*, 284-294.
199. Lingyun, L.; Aryn, R.; Dietmar, W. S. Targeting the Tumor Vasculature with Combretastatin a-4 Disodium Phosphate: Effects on Radiation Therapy. *Int. J. Radiat. Oncol. Biol. Phys.* **1998**, *42*, 899-903.
200. William, R. W.; Alan, E. L.; David, S. M. C.; Bronwyn, G. S. Enhancement of Tumor Radiation Response by the Antivascular Agent 5,6-Dimethylxanthenone-4-Acetic Acid. *Int. J. Radiat. Oncol. Biol. Phys.* **1998**, *42*, 905-908.
201. Willy, L.; Bisan, A.; Sandra, N.; Jan, T.; Michel Op de, B.; Alex, R.; Jozef, A.; Allan van, O.; Walter Van den, B.; Philippe, L. In Vivo Antitumor Effect of Vascular Targeting Combined with Either Ionizing Radiation or Anti-Angiogenesis Treatment. *Int. J. Radiat. Oncol. Biol. Phys.* **2001**, *49*, 443-450.
202. Murata, R.; Siemann, D. W.; Overgaard, J.; Horsman, M. R. Improved Tumor Response by Combining Radiation and the Vascular-Damaging Drug 5,6-Dimethylxanthenone-4-Acetic Acid. *Radiat. Res.* **2001**, *156*, 503-509.
203. Rumi, M.; Dietmar, W. S.; Jens, O.; Michael, R. H. Interaction between Combretastatin a-4 Disodium Phosphate and Radiation in Murine Tumors. *Radiother. Oncol.* **2001**, *60*, 155-161.
204. Dietmar, W. S.; Aryn, M. R. Enhancement of Radiation Therapy by the Novel Vascular Targeting Agent Zd6126. *Int. J. Radiat. Oncol. Biol. Phys.* **2002**, *53*, 164-171.
205. Siemann, D. W.; Mercer, E.; Lepler, S.; Rojiani, A. M. Vascular Targeting Agents Enhance Chemotherapeutic Agent Activities in Solid Tumor Therapy. *Int. J. Cancer* **2002**, *99*, 1-6.
206. Martinelli, M.; Bonezzi, K.; Riccardi, E.; Kuhn, E.; Frapolli, R.; Zucchetti, M.; Ryan, A. J.; Taraboletti, G.; Giavazzi, R. Sequence Dependent Antitumour Efficacy of the Vascular Disrupting Agent Zd6126 in Combination with Paclitaxel. *Br. J. Cancer* **2007**, *97*, 888-94.
207. Wang, E. S.; Pili, R.; Seshadri, M. Modulation of Chemotherapeutic Efficacy by Vascular Disrupting Agents: Optimizing the Sequence and Schedule. *J. Clin. Oncol.* **2012**, *30*, 760-761.
208. Pisitkun, T.; Johnstone, R.; Knepper, M. A. Discovery of Urinary Biomarkers. *Mol. Cell. Proteomics* **2006**, *5*, 1760-1771.
209. Barratt, J.; Topham, P. Urine Proteomics: The Present and Future of Measuring Urinary Protein Components in Disease. *Can. Med. Assoc. J.* **2007**, *177*, 361-368.
210. Adachi, J.; Kumar, C.; Zhang, Y.; Olsen, J. V.; Mann, M. The Human Urinary Proteome Contains More Than 1500 Proteins, Including a Large Proportion of Membrane Proteins. *Genome Biol.* **2006**, *7*, R80.
211. Wide, L.; Gemzell, C. A. An Immunological Pregnancy Test. *Acta Endocrinol. (Copenh.)* **1960**, *XXXV*, 261-267.
212. Cole, L. A.; Kardana, A.; Seifer, D. B.; Bohler, H. C. Urine Hcg Beta-Subunit Core Fragment, a Sensitive Test for Ectopic Pregnancy. *J. Clin. Endocrinol. Metab.* **1994**, *78*, 497-9.
213. Hinokio, Y.; Suzuki, S.; Hirai, M.; Chiba, M.; Hirai, A.; Toyota, T. Oxidative DNA Damage in Diabetes Mellitus: Its Association with Diabetic Complications. *Diabetologia* **1999**, *42*, 995-998.
214. Nishikawa, T.; Sasahara, T.; Kiritoshi, S.; Sonoda, K.; Senokuchi, T.; Matsuo, T.; Kukidome, D.; Wake, N.; Matsumura, T.; Miyamura, N.; et al. Evaluation of Urinary 8-

- Hydroxydeoxy-Guanosine as a Novel Biomarker of Macrovascular Complications in Type 2 Diabetes. *Diabetes Care* **2003**, *26*, 1507-1512.
215. Wu, L. L.; Chiou, C. C.; Chang, P. Y.; Wu, J. T. Urinary 8-OHdG: A Marker of Oxidative Stress to DNA and a Risk Factor for Cancer, Atherosclerosis and Diabetics. *Clin. Chim. Acta* **2004**, *339*, 1-9.
216. Rossing, K.; Mischak, H.; Dakna, M.; Zürlbig, P.; Novak, J.; Julian, B. A.; Good, D. M.; Coon, J. J.; Tarnow, L.; Rossing, P. Urinary Proteomics in Diabetes and Ckd. *J. Am. Soc. Nephrol.* **2008**, *19*, 1283-1290.
217. Tesch, G. H. Review: Serum and Urine Biomarkers of Kidney Disease: A Pathophysiological Perspective. *Nephrology* **2010**, *15*, 609-616.
218. Fassett, R. G.; Venuthurupalli, S. K.; Gobe, G. C.; Coombes, J. S.; Cooper, M. A.; Hoy, W. E. Biomarkers in Chronic Kidney Disease: A Review. *Kidney Int.* **2011**, *80*, 806-21.
219. Mishra, J.; Ma, Q.; Prada, A.; Mitsnefes, M.; Zahedi, K.; Yang, J.; Barasch, J.; Devarajan, P. Identification of Neutrophil Gelatinase-Associated Lipocalin as a Novel Early Urinary Biomarker for Ischemic Renal Injury. *J. Am. Soc. Nephrol.* **2003**, *14*, 2534-2543.
220. Isomaa, B.; Almgren, P.; Tuomi, T.; Forsén, B.; Lahti, K.; Nissén, M.; Taskinen, M.-R.; Groop, L. Cardiovascular Morbidity and Mortality Associated with the Metabolic Syndrome. *Diabetes Care* **2001**, *24*, 683-689.
221. Palaniappan, L.; Carnethon, M.; Fortmann, S. P. Association between Microalbuminuria and the Metabolic Syndrome: Nhanes Iii. *Am. J. Hypertens.* **2003**, *16*, 952-958.
222. Moses, M. A.; Wiederschain, D.; Loughlin, K. R.; Zurakowski, D.; Lamb, C. C.; Freeman, M. R. Increased Incidence of Matrix Metalloproteinases in Urine of Cancer Patients. *Cancer Res.* **1998**, *58*, 1395-1399.
223. Roy, R.; Yang, J.; Moses, M. A. Matrix Metalloproteinases as Novel Biomarkers and Potential Therapeutic Targets in Human Cancer. *J. Clin. Oncol.* **2009**, *27*, 5287-5297.
224. Robbins, S. L.; Kumar, V.; Cotran, R. S., *Robbins and Cotran Pathologic Basis of Disease*. Saunders/Elsevier: Philadelphia, PA, 2010.
225. Davie, E. W.; Kulman, J. D. An Overview of the Structure and Function of Thrombin. *Semin. Thromb. Hemost.* **2006**, *32*, 003-015.
226. Huntington, J. A. Molecular Recognition Mechanisms of Thrombin. *J. Thromb. Haemost.* **2005**, *3*, 1861-1872.
227. Olson, E. S.; Whitney, M. A.; Friedman, B.; Aguilera, T. A.; Crisp, J. L.; Baik, F. M.; Jiang, T.; Baird, S. M.; Tsimikas, S.; Tsién, R. Y.; et al. In Vivo Fluorescence Imaging of Atherosclerotic Plaques with Activatable Cell-Penetrating Peptides Targeting Thrombin Activity. *Integr. Biol.* **2012**, *4*, 595-605.
228. Whitney, M.; Savariar, E. N.; Friedman, B.; Levin, R. A.; Crisp, J. L.; Glasgow, H. L.; Lefkowitz, R.; Adams, S. R.; Steinbach, P.; Nashi, N.; et al. Ratiometric Activatable Cell-Penetrating Peptides Provide Rapid in Vivo Readout of Thrombin Activation. *Angew. Chem. Int. Ed. Engl.* **2013**, *52*, 325-330.
229. Bounameaux, H.; de Moerloose, P.; Perrier, A.; Reber, G. Plasma Measurement of D-Dimer as Diagnostic Aid in Suspected Venous Thromboembolism: An Overview. *Thromb. Haemost.* **1994**, *71*, 1-6.
230. Ginsberg, J. S.; Wells, P. S.; Kearon, C.; Anderson, D.; Crowther, M.; Weitz, J. I.; Bormanis, J.; Brill-Edwards, P.; Turpie, A. G.; MacKinnon, B.; et al. Sensitivity and Specificity of a Rapid Whole-Blood Assay for D-Dimer in the Diagnosis of Pulmonary Embolism. *Ann. Intern. Med.* **1998**, *129*, 1006-1011.

231. Becker, R. C.; Spencer, F. A. Thrombin: Structure, Biochemistry, Measurement, and Status in Clinical Medicine. *J. Thromb. Thrombolysis* **1998**, *5*, 215-229.
232. Choi, H. S.; Liu, W.; Misra, P.; Tanaka, E.; Zimmer, J. P.; Ito, I.; Bawendi, M. G.; Frangioni, J. V. Renal Clearance of Quantum Dots. *Nat. Biotechnol.* **2007**, *25*, 1165-1170.
233. Park, J.-H.; Maltzahn, G. v.; Zhang, L.; Schwartz, M. P.; Ruoslahti, E.; Bhatia, S. N.; Sailor, M. J. Magnetic Iron Oxide Nanoworms for Tumor Targeting and Imaging. *Adv. Mater.* **2008**, *20*, 1630-1635.
234. Park, J.-H.; von Maltzahn, G.; Zhang, L.; Derfus, A. M.; Simberg, D.; Harris, T. J.; Ruoslahti, E.; Bhatia, S. N.; Sailor, M. J. Systematic Surface Engineering of Magnetic Nanoworms for in Vivo Tumor Targeting. *Small* **2009**, *5*, 694-700.
235. Mitchell, G. A.; Gargiulo, R. J.; Huseby, R. M.; Lawson, D. E.; Pochron, S. P.; Sehuanes, J. A. Assay for Plasma Heparin Using a Synthetic Peptide Substrate for Thrombin: Introduction of the Fluorophore Aminoisophthalic Acid, Dimethyl Ester. *Thromb. Res.* **1978**, *13*, 47-52.
236. Asai, K.; Asai, M. A Colorimetric Assay for Plasma Antithrombin Iii Using a New Synthetic Peptide Substrate (Ps-915). *Clin. Chim. Acta* **1984**, *144*, 163-71.
237. Larsen, M. L.; Abildgaard, U.; Teien, A. N.; Gjesdal, K. Assay of Plasma Heparin Using Thrombin and the Chromogenic Substrate H-D-Phe-Pip-Arg-Pna (S-2238). *Thromb. Res.* **1978**, *13*, 285-288.
238. Rijkers, D. S.; Wielders, S. J. H.; Tesser, G. I.; Hemker, H. C. Design and Synthesis of Thrombin Substrates with Modified Kinetic Parameters. *Thromb. Res.* **1995**, *79*, 491-499.
239. Morris, T. A.; Marsh, J. J.; Burrows, C. M.; Chiles, P. G.; Konopka, R. G.; Pedersen, C. A. Urine and Plasma Levels of Fibrinopeptide B in Patients with Deep Vein Thrombosis and Pulmonary Embolism. *Thromb. Res.* **2003**, *110*, 159-165.
240. Rosi, N. L.; Mirkin, C. A. Nanostructures in Biodiagnostics. *Chem. Rev.* **2005**, *105*, 1547-1562.
241. Weiss, E. J.; Hamilton, J. R.; Lease, K. E.; Coughlin, S. R. Protection against Thrombosis in Mice Lacking Par3. *Blood* **2002**, *100*, 3240-3244.
242. Lenain, N.; Freund, M.; Léon, C.; Cazenave, J. P.; Gachet, C. Inhibition of Localized Thrombosis in P2y1-Deficient Mice and Rodents Treated with Mrs2179, a P2y1 Receptor Antagonist. *J. Thromb. Haemost.* **2003**, *1*, 1144-1149.
243. Smyth, S. S.; Reis, E. D.; Väänänen, H.; Zhang, W.; Collier, B. S. Variable Protection of B3-Integrin-Deficient Mice from Thrombosis Initiated by Different Mechanisms. *Blood* **2001**, *98*, 1055-1062.
244. Koeppen, B. M.; Stanton, B. A., *Renal Physiology*. Mosby Elsevier: Philadelphia, 2007.
245. Vestergaard, P.; Leverett, R. Constancy of Urinary Creatinine Excretion. *J. Lab. Clin. Med.* **1958**, *51*, 211-8.
246. Wyss, M.; Kaddurah-Daouk, R. Creatine and Creatinine Metabolism. *Physiol. Rev.* **2000**, *80*, 1107-213.
247. Roe, J. H.; Epstein, J. H.; Goldstein, N. P. A Photometric Method for the Determination of Inulin in Plasma and Urine. *J. Biol. Chem.* **1949**, *178*, 839-845.
248. Gaspari, F.; Perico, N.; Remuzzi, G. Measurement of Glomerular Filtration Rate. *Kidney Int. Suppl.* **1997**, *63*, S151-4.
249. Qi, Z.; Whitt, I.; Mehta, A.; Jin, J.; Zhao, M.; Harris, R. C.; Fogo, A. B.; Breyer, M. D. Serial Determination of Glomerular Filtration Rate in Conscious Mice Using Fitc-Inulin Clearance. *Am. J. Physiol. Renal Physiol.* **2004**, *286*, F590-F596.

250. Ghadiali, J. E.; Stevens, M. M. Enzyme-Responsive Nanoparticle Systems. *Adv. Mater.* **2008**, *20*, 4359-4363.
251. Welser, K.; Adsley, R.; Moore, B. M.; Chan, W. C.; Aylott, J. W. Protease Sensing with Nanoparticle Based Platforms. *Analyst* **2011**, *136*, 29-41.
252. de la Rica, R.; Aili, D.; Stevens, M. M. Enzyme-Responsive Nanoparticles for Drug Release and Diagnostics. *Adv. Drug. Deliv. Rev.* **2012**, *64*, 967-978.
253. Frangioni, J. V. In Vivo near-Infrared Fluorescence Imaging. *Curr. Opin. Chem. Biol.* **2003**, *7*, 626-634.
254. Yager, P.; Domingo, G. J.; Gerdes, J. Point-of-Care Diagnostics for Global Health. *Annu. Rev. Biomed. Eng.* **2008**, *10*, 107-44.
255. Martinez, A. W.; Phillips, S. T.; Whitesides, G. M.; Carrilho, E. Diagnostics for the Developing World: Microfluidic Paper-Based Analytical Devices. *Anal. Chem.* **2009**, *82*, 3-10.
256. Warren, A. D.; Kwong, G. A.; Wood, D. K.; Lin, K. Y.; Bhatia, S. N. Point-of-Care Diagnostics for Noncommunicable Diseases Using Synthetic Urinary Biomarkers and Paper Microfluidics. *Proc. Natl. Acad. Sci. U. S. A.* **2014**.
257. Backes, B. J.; Harris, J. L.; Leonetti, F.; Craik, C. S.; Ellman, J. A. Synthesis of Positional-Scanning Libraries of Fluorogenic Peptide Substrates to Define the Extended Substrate Specificity of Plasmin and Thrombin. *Nat. Biotechnol.* **2000**, *18*, 187-93.
258. Imai, Y.; Murakami, T.; Yoshida, S.; Nishikawa, M.; Ohsawa, M.; Tokunaga, K.; Murata, M.; Shibata, K.; Zushi, S.; Kurokawa, M.; et al. Superparamagnetic Iron Oxide-Enhanced Magnetic Resonance Images of Hepatocellular Carcinoma: Correlation with Histological Grading. *Hepatology* **2000**, *32*, 205-212.
259. Reimer, P.; Jähnke, N.; Fiebich, M.; Schima, W.; Deckers, F.; Marx, C.; Holzknrecht, N.; Saini, S. Hepatic Lesion Detection and Characterization: Value of Nonenhanced Mr Imaging, Superparamagnetic Iron Oxide-Enhanced Mr Imaging, and Spiral Ct—Roc Analysis¹. *Radiology* **2000**, *217*, 152-158.
260. Harisinghani, M. G.; Barentsz, J.; Hahn, P. F.; Deserno, W. M.; Tabatabaei, S.; van de Kaa, C. H.; de la Rosette, J.; Weissleder, R. Noninvasive Detection of Clinically Occult Lymph-Node Metastases in Prostate Cancer. *N. Engl. J. Med.* **2003**, *348*, 2491-2499.
261. Reimer, P.; Balzer, T. Ferucarbotran (Resovist): A New Clinically Approved Res-Specific Contrast Agent for Contrast-Enhanced Mri of the Liver: Properties, Clinical Development, and Applications. *Eur. Radiol.* **2003**, *13*, 1266-1276.
262. Tanimoto, A.; Kuribayashi, S. Application of Superparamagnetic Iron Oxide to Imaging of Hepatocellular Carcinoma. *Eur. J. Radiol.* **2006**, *58*, 200-216.
263. Heesackers, R. A. M.; Jager, G. J.; Hövels, A. M.; de Hoop, B.; van den Bosch, H. C. M.; Raat, F.; Witjes, J. A.; Mulders, P. F. A.; van der Kaa, C. H.; Barentsz, J. O. Prostate Cancer: Detection of Lymph Node Metastases Outside the Routine Surgical Area with Ferumoxtran-10-Enhanced Mr Imaging¹. *Radiology* **2009**, *251*, 408-414.
264. Fink, G. Feedback Actions of Target Hormones on Hypothalamus and Pituitary with Special Reference to Gonadal Steroids. *Annu. Rev. Physiol.* **1979**, *41*, 571-585.
265. Mundy, G. R.; Guise, T. A. Hormonal Control of Calcium Homeostasis. *Clin. Chem.* **1999**, *45*, 1347-1352.
266. Bader, M. Tissue Renin-Angiotensin-Aldosterone Systems: Targets for Pharmacological Therapy. *Annu. Rev. Pharmacol. Toxicol.* **2010**, *50*, 439-465.

267. Lenardo, M.; Chan, K. M.; Hornung, F.; McFarland, H.; Siegel, R.; Wang, J.; Zheng, L. Mature T Lymphocyte Apoptosis--Immune Regulation in a Dynamic and Unpredictable Antigenic Environment. *Annu. Rev. Immunol.* **1999**, *17*, 221-53.
268. Wing, K.; Sakaguchi, S. Regulatory T Cells Exert Checks and Balances on Self Tolerance and Autoimmunity. *Nat. Immunol.* **2010**, *11*, 7-13.
269. Kitano, H. Systems Biology: A Brief Overview. *Science* **2002**, *295*, 1662-1664.
270. Sprinzak, D.; Elowitz, M. B. Reconstruction of Genetic Circuits. *Nature* **2005**, *438*, 443-448.
271. Maitz, M. F.; Freudenberg, U.; Tsurkan, M. V.; Fischer, M.; Beyrich, T.; Werner, C. Bio-Responsive Polymer Hydrogels Homeostatically Regulate Blood Coagulation. *Nat. Commun.* **2013**, *4*.
272. Moscucci, M. Frequency and Costs of Ischemic and Bleeding Complications after Percutaneous Coronary Interventions: Rationale for New Antithrombotic Agents. *J. Invasive Cardiol.* **2002**, *14 Suppl B*, 55B-64B.
273. Mannucci, P. M.; Franchini, M. Old and New Anticoagulant Drugs: A Minireview. *Ann. Med.* **2011**, *43*, 116-123.
274. Eikelboom, J. W.; Hirsh, J. Monitoring Unfractionated Heparin with the Aptt: Time for a Fresh Look. *Thromb. Haemost.* **2006**, *96*, 547-52.
275. Sarikaya, M.; Tamerler, C.; Jen, A. K. Y.; Schulten, K.; Baneyx, F. Molecular Biomimetics: Nanotechnology through Biology. *Nat. Mater.* **2003**, *2*, 577-585.
276. Vasudev, S. C.; Chandy, T.; Sharma, C. P. Development of Chitosan/Polyethylene Vinyl Acetate Co-Matrix: Controlled Release of Aspirin-Heparin for Preventing Cardiovascular Thrombosis. *Biomaterials* **1997**, *18*, 375-381.
277. Gutowska, A.; Bae, Y. H.; Jacobs, H.; Mohammad, F.; Mix, D.; Feijen, J.; Kim, S. W. Heparin Release from Thermosensitive Polymer Coatings: In Vivo Studies. *J. Biomed. Mater. Res.* **1995**, *29*, 811-21.
278. Baldwin, A. D.; Robinson, K. G.; Militar, J. L.; Derby, C. D.; Kiick, K. L.; Akins, R. E. In Situ Crosslinkable Heparin-Containing Poly(Ethylene Glycol) Hydrogels for Sustained Anticoagulant Release. *J. Biomed. Mater. Res. A* **2012**, *100A*, 2106-2118.
279. Chaikof, E. L. The Development of Prosthetic Heart Valves — Lessons in Form and Function. *N. Engl. J. Med.* **2007**, *357*, 1368-1371.
280. Cronin, R. E.; Reilly, R. F. Unfractionated Heparin for Hemodialysis: Still the Best Option. *Semin. Dial.* **2010**, *23*, 510-5.
281. Wieduwild, R.; Tsurkan, M.; Chwalek, K.; Murawala, P.; Nowak, M.; Freudenberg, U.; Neinhuis, C.; Werner, C.; Zhang, Y. Minimal Peptide Motif for Non-Covalent Peptide-Heparin Hydrogels. *J. Am. Chem. Soc.* **2013**, *135*, 2919-2922.
282. DeLucia, A., 3rd; Wakefield, T. W.; Andrews, P. C.; Nichol, B. J.; Kadell, A. M.; Wroblewski, S. K.; Downing, L. J.; Stanley, J. C. Efficacy and Toxicity of Differently Charged Polycationic Protamine-Like Peptides for Heparin Anticoagulation Reversal. *J. Vasc. Surg.* **1993**, *18*, 49-58; discussion 58-60.
283. Jenny, R. J.; Mann, K. G.; Lundblad, R. L. A Critical Review of the Methods for Cleavage of Fusion Proteins with Thrombin and Factor Xa. *Protein Expr. Purif.* **2003**, *31*, 1-11.
284. Li, S.-D.; Huang, L. Pharmacokinetics and Biodistribution of Nanoparticles. *Mol. Pharm.* **2008**, *5*, 496-504.

285. Fischer, D.; Li, Y.; Ahlemeyer, B.; Krieglstein, J.; Kissel, T. In Vitro Cytotoxicity Testing of Polycations: Influence of Polymer Structure on Cell Viability and Hemolysis. *Biomaterials* **2003**, *24*, 1121-31.
286. Rimann, M.; Luhmann, T.; Textor, M.; Guerino, B.; Ogier, J.; Hall, H. Characterization of PII-G-Peg-DNA Nanoparticles for the Delivery of Therapeutic DNA. *Bioconjug. Chem.* **2008**, *19*, 548-57.
287. Raschke, R. A.; Reilly, B. M.; Guidry, J. R.; Fontana, J. R.; Srinivas, S. The Weight-Based Heparin Dosing Nomogram Compared with a Standard Care Nomogram Randomized Controlled Trial. *Ann. Intern. Med.* **1993**, *119*, 874-881.
288. Granger, C. B.; Hirsh, J.; Califf, R. M.; Col, J.; White, H. D.; Betriu, A.; Woodlief, L. H.; Lee, K. L.; Bovill, E. G.; Simes, R. J.; et al. Activated Partial Thromboplastin Time and Outcome after Thrombolytic Therapy for Acute Myocardial Infarction: Results from the Gusto-I Trial. *Circulation* **1996**, *93*, 870-878.
289. Anand, S. S.; Yusuf, S.; Pogue, J.; Ginsberg, J. S.; Hirsh, J.; Investigators, o. B. o. t. O. t. A. S. f. I. S. Relationship of Activated Partial Thromboplastin Time to Coronary Events and Bleeding in Patients with Acute Coronary Syndromes Who Receive Heparin. *Circulation* **2003**, *107*, 2884-2888.
290. Passirani, C.; Barratt, G.; Devissaguet, J.-P.; Labarre, D. Long-Circulating Nanoparticles Bearing Heparin or Dextran Covalently Bound to Poly(Methyl Methacrylate). *Pharm. Res.* **1998**, *15*, 1046-1050.
291. Brummel, K. E.; Paradis, S. G.; Butenas, S.; Mann, K. G. Thrombin Functions During Tissue Factor-Induced Blood Coagulation. *Blood* **2002**, *100*, 148-152.
292. Comer, M. B.; Cackett, K. S.; Gladwell, S.; Wood, L. M.; Dawson, K. M. Thrombolytic Activity of Bb-10153, a Thrombin-Activatable Plasminogen. *J. Thromb. Haemost.* **2005**, *3*, 146-153.
293. Lin, K. Y.; Kwong, G. A.; Warren, A. D.; Wood, D. K.; Bhatia, S. N. Nanoparticles That Sense Thrombin Activity as Synthetic Urinary Biomarkers of Thrombosis. *ACS Nano* **2013**, *7*, 9001-9009.
294. Dawson, K. M.; Cook, A.; Devine, J. M.; Edwards, R. M.; Hunter, M. G.; Raper, R. H.; Roberts, G. Plasminogen Mutants Activated by Thrombin. Potential Thrombus-Selective Thrombolytic Agents. *J. Biol. Chem.* **1994**, *269*, 15989-92.
295. Kurz, K. D.; Main, B. W.; Sandusky, G. E. Rat Model of Arterial Thrombosis Induced by Ferric Chloride. *Thromb. Res.* **1990**, *60*, 269-280.
296. Furie, B.; Furie, B. C. Thrombus Formation in Vivo. *J. Clin. Invest.* **2005**, *115*, 3355-3362.
297. Arepally, G. M.; Ortel, T. L. Heparin-Induced Thrombocytopenia. *N. Engl. J. Med.* **2006**, *355*, 809-817.
298. Harker, L.; Malpass, T.; Branson, H.; Hessel, E. d.; Slichter, S. Mechanism of Abnormal Bleeding in Patients Undergoing Cardiopulmonary Bypass: Acquired Transient Platelet Dysfunction Associated with Selective Alpha-Granule Release. *Blood* **1980**, *56*, 824-834.
299. Zhao, Y.; Trewyn, B. G.; Slowing, I. I.; Lin, V. S. Y. Mesoporous Silica Nanoparticle-Based Double Drug Delivery System for Glucose-Responsive Controlled Release of Insulin and Cyclic Amp. *J. Am. Chem. Soc.* **2009**, *131*, 8398-8400.
300. Kim, H.; Kang, Y. J.; Kang, S.; Kim, K. T. Monosaccharide-Responsive Release of Insulin from Polymersomes of Polyboroxole Block Copolymers at Neutral Ph. *J. Am. Chem. Soc.* **2012**, *134*, 4030-4033.

301. Farmer, T. G., Jr.; Edgar, T. F.; Peppas, N. A. The Future of Open- and Closed-Loop Insulin Delivery Systems. *J. Pharm. Pharmacol.* **2008**, *60*, 1-13.
302. Teien, A. N.; Lie, M.; Abildgaard, U. Assay of Heparin in Plasma Using a Chromogenic Substrate for Activated Factor X. *Thromb. Res.* **1976**, *8*, 413-416.
303. Gouzy, M. F.; Sperling, C.; Salchert, K.; Pompe, T.; Streller, U.; Uhlmann, P.; Rauwolf, C.; Simon, F.; Bohme, F.; Voit, B.; et al. In Vitro Blood Compatibility of Polymeric Biomaterials through Covalent Immobilization of an Amidine Derivative. *Biomaterials* **2004**, *25*, 3493-501.
304. Hallahan, D.; Geng, L.; Qu, S.; Scarfone, C.; Giorgio, T.; Donnelly, E.; Gao, X.; Clanton, J. Integrin-Mediated Targeting of Drug Delivery to Irradiated Tumor Blood Vessels. *Cancer Cell* **2003**, *3*, 63-74.
305. Chambers, A. F.; Groom, A. C.; MacDonald, I. C. Dissemination and Growth of Cancer Cells in Metastatic Sites. *Nat. Rev. Cancer* **2002**, *2*, 563-72.
306. Kummar, S.; Chen, H. X.; Wright, J.; Holbeck, S.; Millin, M. D.; Tomaszewski, J.; Zweibel, J.; Collins, J.; Doroshow, J. H. Utilizing Targeted Cancer Therapeutic Agents in Combination: Novel Approaches and Urgent Requirements. *Nat. Rev. Drug Discov.* **2010**, *9*, 843-856.
307. Al-Lazikani, B.; Banerji, U.; Workman, P. Combinatorial Drug Therapy for Cancer in the Post-Genomic Era. *Nat. Biotechnol.* **2012**, *30*, 679-692.
308. Weiner, L. M.; Surana, R.; Wang, S. Monoclonal Antibodies: Versatile Platforms for Cancer Immunotherapy. *Nat. Rev. Immunol.* **2010**, *10*, 317-27.
309. Heath, V. L.; Bicknell, R. Anticancer Strategies Involving the Vasculature. *Nat. Rev. Clin. Oncol.* **2009**, *6*, 395-404.
310. DeVita, V. T., Jr.; Young, R. C.; Canellos, G. P. Combination Versus Single Agent Chemotherapy: A Review of the Basis for Selection of Drug Treatment of Cancer. *Cancer* **1975**, *35*, 98-110.
311. Han, Z.; Fu, A.; Wang, H.; Diaz, R.; Geng, L.; Onishko, H.; Hallahan, D. E. Noninvasive Assessment of Cancer Response to Therapy. *Nat. Med.* **2008**, *14*, 343-349.
312. Passarella, R. J.; Zhou, L.; Phillips, J. G.; Wu, H.; Hallahan, D. E.; Diaz, R. Recombinant Peptides as Biomarkers for Tumor Response to Molecular Targeted Therapy. *Clin. Cancer Res.* **2009**, *15*, 6421-6429.
313. Rubinfeld, B.; Upadhyay, A.; Clark, S. L.; Fong, S. E.; Smith, V.; Koeppen, H.; Ross, S.; Polakis, P. Identification and Immunotherapeutic Targeting of Antigens Induced by Chemotherapy. *Nat Biotech* **2006**, *24*, 205-209.
314. Morinaga, Y.; Suga, Y.; Ehara, S.; Harada, K.; Nihei, Y.; Suzuki, M. Combination Effect of Ac-7700, a Novel Combretastatin a-4 Derivative, and Cisplatin against Murine and Human Tumors in Vivo. *Cancer Sci.* **2003**, *94*, 200-204.
315. Dumontet, C.; Jordan, M. A. Microtubule-Binding Agents: A Dynamic Field of Cancer Therapeutics. *Nat. Rev. Drug Discov.* **2010**, *9*, 790-803.
316. Ren, Y.; Cheung, H. W.; von Maltzhan, G.; Agrawal, A.; Cowley, G. S.; Weir, B. A.; Boehm, J. S.; Tamayo, P.; Karst, A. M.; Liu, J. F.; et al. Targeted Tumor-Penetrating Sirna Nanocomplexes for Credentialing the Ovarian Cancer Oncogene Id4. *Sci. Transl. Med.* **2012**, *4*, 147ra112.
317. Roth, L.; Agemy, L.; Kotamraju, V. R.; Braun, G.; Teesalu, T.; Sugahara, K. N.; Hamzah, J.; Ruoslahti, E. Transtumoral Targeting Enabled by a Novel Neuropilin-Binding Peptide. *Oncogene* **2012**, *31*, 3754-63.

318. Åkerman, M. E.; Chan, W. C. W.; Laakkonen, P.; Bhatia, S. N.; Ruoslahti, E. Nanocrystal Targeting in Vivo. *Proc. Natl. Acad. Sci. U. S. A.* **2002**, *99*, 12617-12621.
319. Karmali, P. P.; Kotamraju, V. R.; Kastantin, M.; Black, M.; Missirlis, D.; Tirrell, M.; Ruoslahti, E. Targeting of Albumin-Embedded Paclitaxel Nanoparticles to Tumors. *Nanomed: Nanotechnol. Biol. Med.* **2009**, *5*, 73-82.
320. von Maltzahn, G.; Ren, Y.; Park, J.-H.; Min, D.-H.; Kotamraju, V. R.; Jayakumar, J.; Fogal, V.; Sailor, M. J.; Ruoslahti, E.; Bhatia, S. N. In Vivo Tumor Cell Targeting with “Click” Nanoparticles. *Bioconjug. Chem.* **2008**, *19*, 1570-1578.
321. Yuan, F.; Dellian, M.; Fukumura, D.; Leunig, M.; Berk, D. A.; Torchilin, V. P.; Jain, R. K. Vascular Permeability in a Human Tumor Xenograft: Molecular Size Dependence and Cutoff Size. *Cancer Res.* **1995**, *55*, 3752-3756.
322. Cheng, Z.; Al Zaki, A.; Hui, J. Z.; Muzykantov, V. R.; Tsourkas, A. Multifunctional Nanoparticles: Cost Versus Benefit of Adding Targeting and Imaging Capabilities. *Science* **2012**, *338*, 903-910.
323. Nihei, Y.; Suga, Y.; Morinaga, Y.; Ohishi, K.; Okano, A.; Ohsumi, K.; Hatanaka, T.; Nakagawa, R.; Tsuji, T.; Akiyama, Y.; et al. A Novel Combretastatin a-4 Derivative, Ac-7700, Shows Marked Antitumor Activity against Advanced Solid Tumors and Orthotopically Transplanted Tumors. *Cancer Sci.* **1999**, *90*, 1016-1025.
324. Davis, M. E.; Zuckerman, J. E.; Choi, C. H.; Seligson, D.; Tolcher, A.; Alabi, C. A.; Yen, Y.; Heidel, J. D.; Ribas, A. Evidence of Rnai in Humans from Systemically Administered Sirna Via Targeted Nanoparticles. *Nature* **2010**, *464*, 1067-70.
325. Kratz, F.; Roth, T.; Fichiner, I.; Schumacher, P.; Fiebig, H.; Unger, C. In Vitro and in Vivo Efficacy of Acid-Sensitive Transferrin and Albumin Doxorubicin Conjugates in a Human Xenograft Panel and in the Mda-Mb-435 Mamma Carcinoma Model. *J. Drug Target.* **2000**, *8*, 305-318.
326. Tice, D. A.; Szeto, W.; Soloviev, I.; Rubinfeld, B.; Fong, S. E.; Dugger, D. L.; Winer, J.; Williams, P. M.; Wieand, D.; Smith, V.; et al. Synergistic Induction of Tumor Antigens by Wnt-1 Signaling and Retinoic Acid Revealed by Gene Expression Profiling. *J. Biol. Chem.* **2002**, *277*, 14329-14335.
327. Hope, M. J.; Bally, M. B.; Webb, G.; Cullis, P. R. Production of Large Unilamellar Vesicles by a Rapid Extrusion Procedure. Characterization of Size Distribution, Trapped Volume and Ability to Maintain a Membrane Potential. *Biochim. Biophys. Acta* **1985**, *812*, 55-65.
328. Mayer, L. D.; Bally, M. B.; Hope, M. J.; Cullis, P. R. Uptake of Antineoplastic Agents into Large Unilamellar Vesicles in Response to a Membrane Potential. *Biochim. Biophys. Acta* **1985**, *816*, 294-302.
329. Euhus, D. M.; Hudd, C.; Laregina, M. C.; Johnson, F. E. Tumor Measurement in the Nude Mouse. *J. Surg. Oncol.* **1986**, *31*, 229-234.
330. Schwartz, M. A Biomathematical Approach to Clinical Tumor Growth. *Cancer* **1961**, *14*, 1272-1294.
331. Gosalia, D. N.; Salisbury, C. M.; Maly, D. J.; Ellman, J. A.; Diamond, S. L. Profiling Serine Protease Substrate Specificity with Solution Phase Fluorogenic Peptide Microarrays. *Proteomics* **2005**, *5*, 1292-1298.
332. Harris, J. L.; Backes, B. J.; Leonetti, F.; Mahrus, S.; Ellman, J. A.; Craik, C. S. Rapid and General Profiling of Protease Specificity by Using Combinatorial Fluorogenic Substrate Libraries. *Proc. Natl. Acad. Sci. U. S. A.* **2000**, *97*, 7754-7759.

333. Hockin, M. F.; Jones, K. C.; Everse, S. J.; Mann, K. G. A Model for the Stoichiometric Regulation of Blood Coagulation. *J. Biol. Chem.* **2002**, *277*, 18322-18333.
334. Schellenberger, V.; Wang, C. W.; Geething, N. C.; Spink, B. J.; Campbell, A.; To, W.; Scholle, M. D.; Yin, Y.; Yao, Y.; Bogin, O.; et al. A Recombinant Polypeptide Extends the in Vivo Half-Life of Peptides and Proteins in a Tunable Manner. *Nat. Biotechnol.* **2009**, *27*, 1186-90.
335. Ahmed, B.; Robert, L.; Martin, M.; Gerhard, W., Challenges for Pegylated Proteins and Alternative Half-Life Extension Technologies Based on Biodegradable Polymers. In *Tailored Polymer Architectures for Pharmaceutical and Biomedical Applications*, American Chemical Society: 2013; Vol. 1135, pp 215-233.
336. Kratz, F. Albumin as a Drug Carrier: Design of Prodrugs, Drug Conjugates and Nanoparticles. *J. Control. Release* **2008**, *132*, 171-83.
337. Gao, C.; Boylan, B.; Fang, J.; Wilcox, D. A.; Newman, D. K.; Newman, P. J. Heparin Promotes Platelet Responsiveness by Potentiating Aiiβ3-Mediated Outside-in Signaling. *Blood* **2011**, *117*, 4946-4952.
338. Wu, W.; Zhou, S. Responsive Materials for Self-Regulated Insulin Delivery. *Macromol. Biosci.* **2013**, *13*, 1464-1477.
339. Medzhitov, R. Origin and Physiological Roles of Inflammation. *Nature* **2008**, *454*, 428-35.
340. Sarma, J. V.; Ward, P. A. The Complement System. *Cell Tissue Res.* **2011**, *343*, 227-35.
341. Reddy, S. T.; van der Vlies, A. J.; Simeoni, E.; Angeli, V.; Randolph, G. J.; O'Neil, C. P.; Lee, L. K.; Swartz, M. A.; Hubbell, J. A. Exploiting Lymphatic Transport and Complement Activation in Nanoparticle Vaccines. *Nat. Biotechnol.* **2007**, *25*, 1159-1164.
342. Mahmoud, E. A.; Sankaranarayanan, J.; Morachis, J. M.; Kim, G.; Almutairi, A. Inflammation Responsive Logic Gate Nanoparticles for the Delivery of Proteins. *Bioconjug. Chem.* **2011**, *22*, 1416-21.
343. Wang, Z.; Li, J.; Cho, J.; Malik, A. B. Prevention of Vascular Inflammation by Nanoparticle Targeting of Adherent Neutrophils. *Nat. Nanotechnol.* **2014**, *9*, 204-10.